Kinematics of Early-Type Galaxies in the Magneticum Pathfinder Simulations

Felix Schulze

München 2015

Master Thesis

Kinematik elliptischer Galaxien in den Magneticum Pathfinder Simulationen

Masterarbeit

an der

Ludwig–Maximilians–Universität München

eingereicht von

Felix Schulze

(Matr. Nr.: 10093383)

geboren am 21.02.1989 in Isny im Allgäu

betreut von
PD Dr. Klaus Dolag

und
Dr. Rhea-Silvia Remus

München, den 4. März 2016

Evaluator: PD Dr. Klaus Dolag

Contents

1. Theoretical Foundation

1.1. Review on Galaxies and Classification

Only since the first quarter of the twentieth century when the distance measurements by Edwin Hubble had been conducted the existence of objects outside our own galaxy has been publicly accepted.

The first proposal of a galaxy classification was submitted by Edwin Hubble in 1926 (Hubble, 1926). In his study Hubble classified 400 nearby galaxies according to their apparent morphology. The results clearly indicated a partition into mainly two morphological types. Only three per cent could be assigned to neither of the two types, hence were classified as irregulars. The first group features characteristic elliptical isophotes, merely varying in their apparent elongation, thus called elliptical galaxies. Galaxies of this type do not show any evidence of internal structure. Therefore a further division according to the elongation was introduced. In contrast, members of the second group, which are called spiral galaxies, show typically a larger, but within the group constant, elongation. However, the main difference to the elliptical galaxies is the internal spiral-arm like structure. The structural features are used as an further classification criterion within the branch of spiral galaxies.

This study provided the basis for the well-known Hubble-sequence or Hubble's tuning fork fig. 1.1. The left side includes the spheroid-dominated elliptical galaxies, whereas the right side is composed of the disk-dominated spiral galaxies with spiral arms.

Spiral galaxies are further divided into objects exhibiting a stellar bar in the centre (right top) and the ones not showing this feature (right down).

The galaxies at the merging point of both classes are called lenticular or S0 galaxies. They represent the transition between ellipticals and spirals, featuring properties of both categories.

Lenticular and elliptical objects are included in a larger, historically motivated class, called early-type galaxies or ETGs. Spiral galaxies are also known as late-type galaxies (LTGs). This terminology has its origin in the early theory of galaxy formation.

1.1.1. Spiral Galaxies

As mentioned before spiral galaxies are grouped according to their structural features. Objects exhibiting a stellar bar in the centre are labeled by **SB**, whereas
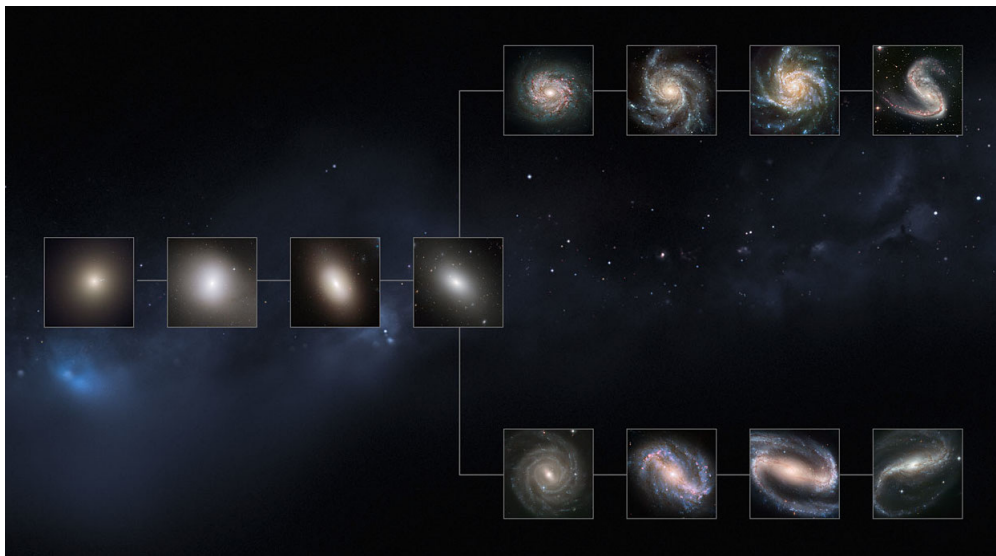
Figure 1.1.: Illustration of the Hubble sequence proposed by Edwin Hubble in 1936. Image credit: NASA, ESA, M. Kornmesser.

objects without a bar are labeled with **S**.

Independent of the bar, these types form a continuous sequence from bulge dominated galaxies with tightly bound arms **S(B)a** on the left to smaller bulges with loosely bound arms **S(B)c** on the extreme right.

Spiral galaxies in general can be decomposed into three components, namely the central bulge, a rotational supported disk, and a surrounding halo. The bulge forms the centre of the spiral, mainly consisting of old population II stars and almost no gas. Its radial surface brightness profile can be fitted by a Sérsic profile of the form

$$\rho(R) \propto e^{-b_n\left(\frac{R}{R_e}\right)^{\frac{1}{n}}},\tag{1.1}$$

where n is the so-called Sérsic index (Sérsic, 1963). Typical values for the Sérsic index are between 0 and 3 (Weinzirl et al., 2009). This profile can also be applied to elliptical galaxies, indicating similar properties for bulges and ETGs.

The most distinctive component of LTGs is the galactic disk showing the characteristic spiral structure. Gas as well as the stars populating the disk move on nearly circular orbits. The surface brightness profile can be described by an exponential law i.e., a Sérsic profile with $n = 1$ (see eq. 1.1):

$$I(R) = I_0 \cdot e^{\frac{r}{r_e}}.\tag{1.2}$$

During the past decades there have been several approaches to understand the dynamics and formation of the spiral structure (Lin and Shu, 1964; Toomre, 1977). Different theories like the Density-Wave-Theory by Lin and Shu (1964) were proposed, however still today no consistent theory exists.

Since the stars in a spiral galaxy move on nearly circular orbits their rotational velocity V_{rot} can be calculated from the mass distribution

$$V_{rot}(r) = \sqrt{\frac{G\ M(<r)}{r}}, \qquad (1.3)$$

where G is the gravitational constant and $M(<r)$ the enclosed mass. Observations by Rubin et al. (1978) revealed a constant $V_{\mathrm{rot}}(r)$ profile. Therefore, unlike the luminosity, the $M(<r)$ is proportional to the radius. This is clear evidence for an extended dark matter halo surrounding the galaxy. Since dark matter can not be observed directly, modern N-Body simulations are a convenient method to analyse its properties. As a result of these simulations the radial profile of dark matter haloes can be described by the a NFW profile (Navarro et al., 1996):

$$\frac{\rho(r)}{\rho_{\mathrm{crit}}} = \frac{\delta_c}{\frac{r}{r_{\mathrm{s}}}(1+\frac{r}{r_{\mathrm{s}}})^2}, \qquad (1.4)$$

where $\rho_{\mathrm{crit}} = 3H^2/8\pi G$ is the critical density; $r_{\mathrm{s}} = \frac{r_{200}}{c}$ is the characteristic radius; δ_c and c are two dimensionless parameters.

An important scaling relation fulfilled by spiral galaxies is the Tully-Fischer-relation (Tully and Fisher, 1977). It states a exponential correlation between the luminosity L and the maximum rotational velocity

$$L \propto V_{\mathrm{max}}^{\alpha}, \qquad (1.5)$$

where α has typical values between 2.5 and 4.2. Hence it correlates a property dominated by the dark matter halo with the luminosity which is determined by the star formation history.

1.1.2. Elliptical Galaxies

Early type galaxies are dominated by old stellar populations and a very small amount of gas. Therefore, they are clearly recognisable by their red colour. Due to the lack of gas ETGs show very low star formation rates (Shapiro et al., 2010).

Elliptical galaxies span a broad range of masses from about 10^7 for dwarf elliptical galaxies to 10^{13} solar masses for giant ETGs. This mass-range is much broader than for spiral galaxies.

The luminosity distribution of ellipticals is very smooth and does not exhibit any features like spiral structures. de Vaucouleurs (1948) suggested that the luminosity profile follows a Sérsic profile with $n = 4$. However, Sérsic profiles with distinct values of n fit the large variety of ETGs much better (Ferrarese et al., 2006).

Within the Hubble sequence, ETGs are further classified by a parameter which

measures their elongation, called ellipticity:

$$\epsilon = 1 - \frac{b}{a} \qquad (1.6)$$

where a is the major and b the minor axis of the galaxy isophotes. More round ETGs (low ϵ) are located on the left of the Hubble tuning fork, whereas the flat ones (high ϵ) are near the **S0s**. They are labeled as **EN** where N = 10ϵ.

Obviously, this classification depends on the viewing angle and therefore does not reveal the intrinsic morphology. Hence, this classification mainly correlates with inclination rather than with fundamental properties. Due to this drawback the observed ellipticity is often denoted as apparent ellipticity. Based on that issue, Kormendy and Bender (1996) proposed a revision of the Hubble classification. Detailed investigations of the surface brightness of ETG's revealed small deviation of the isophotes from an ellipse. Therefore, they suggested to arrange ETG's depending on the discyness or boxyness of their isophote shapes. Claiming that discy ellipticals have significant rotation, little or no radio and X-ray emission, while boxy ellipticals show less rotation and stronger than average radio and X-ray emission this classification correlates with fundamental properties (Bender et al., 1989; Pasquali et al., 2007).

For many decades the Hubble sequence for elliptical galaxies has been the commonly used classification scheme. Only since the observational methods improved it is possible to obtain detailed kinematical data, revealing a richness of different structures.

Features like kinematically distinct cores (KDC), counter-rotating cores and misalignments between the photometric and kinematic axis are found in kinematical maps provides by integral field spectrographs like SAURON (Bacon et al., 2001).

Based on these observation a new view of elliptical galaxies emerged, allowing to classify the sample into two families, the fast and the slow rotators (Emsellem et al., 2007; Krajnović et al., 2011; Emsellem et al., 2011). Fast rotators show significant large scale rotation, whereas slow rotators have low angular momentum and exhibit more complex kinematical structures. Thus this categorization is not only according to the morphology, but also corresponding to their kinematics.

Similar to the Tully-Fischer relation for spiral galaxies, the Faber-Jackson relation relates the luminosity L with the central velocity dispersion σ_0 (Faber and Jackson, 1976):

$$L \propto \sigma_0^{\gamma} \qquad (1.7)$$

The exponent γ is observed to be approximately 4, but its value depends on the range of luminosities which are fitted. In addition a further correlation between the mean surface brightness $\langle I_e \rangle$ inside R_e and σ_0 was found. Therefore, $\langle I_e \rangle$, σ_0 and L_e span a curved plane in a three dimensional space, called the fundamental plane.

1.2. Cosmological Structure and Galaxy Formation

1.2.1. Cosmological Structure Formation

Expansion of the Universe

A very essential mechanism to understand the evolution of the universe is spatial expansion. Without it the structures, like galaxies and clusters, we observe today would not exist.

In 1915, Albert Einstein published the ground breaking theory of General Relativity (Einstein, 1915). Based on this theory the first solutions of Einsteins field equations described a static and flat universe. Einstein himself preferred a static universe containing only matter. To prevent such a universe from collapsing, he introduced a positive cosmological constant $\Lambda > 0$, which counteract against gravity. This was not unreasonable at that time, because the measured velocities of nearby stars were small. Later on the idea of a static universe was proved to be wrong by observational results.

Another famous approach is the de-Sitter model formulated by Willem de Sitter (de Sitter, 1916a,b, 1917). It models the universe as spatially flat without any matter or radiation, but with a positive cosmological constant driving the expansion. Although such a model uses unphysical assumptions it was the first formulation of a spatially expanding universe.

The present-day accepted model of modern cosmology was introduced by Alexander Friedmann in 1922 (Friedmann, 1922). It is based on the assumption, that the cosmological principle is valid if one observes the universe on scales large enough:

- **The universe is homogeneous** - on large scales the matter is distributed uniformly, independent of an observers location.

- **The universe is isotropic** - on large scales the universe looks the same in all spatial directions, independent of an observer's location.

These assumptions constrain the form of the Friedmann-Robertson-Walker (FRW) metric tensor $g_{\mu\nu}$ and the stress-energy tensor $T_{\mu\nu}$ in Einsteins field equations:

$$R_{\mu\nu} - \frac{1}{2} R \, g_{\mu\nu}^{\mathrm{FRW}} + \Lambda \, g_{\mu\nu}^{\mathrm{FRW}} = \frac{8 \, \pi \, G}{c^4} \, T_{\mu\nu}^{\mathrm{FRW}} \tag{1.8}$$

For the Friedmann-Robertson-Walker metric and a stress-tensor, obeying the cosmological principle, eq. 1.8 are called the Friedmann equations. Combining the Friedmann equations yields the evolution equation for the scale factor $a(t)$:

$$\frac{\dot{a}(t)}{a(t)} = H_0^2 \left(\frac{\Omega_{\mathrm{r}}}{a(t)^4} + \frac{\Omega_{\mathrm{m}}}{a(t)^3} + \frac{\Omega_{\mathrm{k}}}{a(t)^2} + \Omega_{\Lambda} \right) \tag{1.9}$$

Therefore, the evolution of $a(t)$ is determined by five parameters:

- H_0 is the famous Hubble constant defined as

$$H_0 = \frac{\dot{a}(t_0)}{a(t_0)} \tag{1.10}$$

- Ω_r is the present-day radiative energy density in units of the critical density

- $\Omega_m = \Omega_B + \Omega_{DM}$ the present-day matter density of the dark matter and baryonic component

- $\Omega_\Lambda = \Lambda/\rho_{\mathrm{crit}}$ describes the dark energy component

- $\Omega_k = 1 - \Omega_m - \Omega_r - \Omega_\Lambda$ depends on the curvature k, hence defines the geometry of the universe $\Omega_k < 0$ describes an open hyperbolic geometry. For $\Omega_k = 0$ the universe is flat. If $\Omega_k > 0$ the universe is spherical and closed.

One important effect induced by the expansion is the redshift of light. It can be observed in the wavelength of a photon, which is emitted at t_e and absorbed at t_a. From the FRW metric and the defining property of comoving distances one can derive a relation between $\lambda(t_e)$, $\lambda(t_a)$, and the scale factor:

$$z \equiv \frac{\lambda(t_a) - \lambda(t_e)}{\lambda(t_e)} = \frac{1}{a(t_e)} - 1 \tag{1.11}$$

This shift of wavelength is parametrized by the so-called redshift parameter z. Hence, every moment in cosmic time is related to a unique redshift.

Structure Formation in the Early Universe

The kinematics of present-day galaxies are completely determined by their formation history. Since these processes happen on cosmological time scales, it is crucial to understand them in a cosmological context.

The modern picture of structure formation starts when the universe was about one Planck time old. At this earliest epoch all matter was concentrated in a very small volume causing very high temperatures and pressure. Due to the high temperatures the strong and electroweak force were too weak to bind the gluons in protons or neutrons. Hence, the universe was in a plasma state consisting of free charges.

At this early stage the universe was dominated by photons, scattering with the free charged particles. This process prevented the matter from forming potential wells, causing density fluctuation to smear out leading to a uniform optically thick universe. At a certain point the universe was cold enough for the gluons to form protons and neutrons, however, not cold enough to build neutral atoms. In contrast, the dark was able to grow potential wells caused by quantum fluctuations, since it is not influenced by the electromagnetic force (Mukhanov and Chibisov, 1981).

When the temperature of the universe decreased below 3000K a global phase transition, called recombination, took place. The particles had slowed down enough

to form neutral atoms out of the electrons and atomic nuclei. As a result, the photons now could travel freely without scattering. The matter decoupled from the radiation and the universe became optically transparent.

The gravitational attraction of the dark matter was now the dominating force acting on the newly formed baryonic matter. Hence, the baryonic matter followed the density fluctuation in the dark matter, initiating the formation of the first protogalaxies.

The detection of the radiation emitted at the moment of recombination was one of the groundbreaking observational results of modern cosmology, referred to as Cosmic Microwave Background (CMB). The discovery goes back to Arno Penzias and Robert Woodrow Wilson, in 1964. They used a Dicke radiometer, which they intended to use for radio astronomy and satellite communication experiments. After examining their data, they found a signal distributed isotropically over the complete sky, corresponding to a temperature of $3.5K$ (Penzias and Wilson, 1965). The low temperature is due to the expansion of the universe, which causes the wavelength to increase according to eq. 1.11 and therefore the energy of the photons to decrease.

Further investigations by the space-based probes COBE (launched 1989), WMAP (launched 2009) and recently Planck revealed the most striking feature of the CMB: on large scales it is isotropic with a temperature of $2.7K$, though on small scales it exhibits little temperature fluctuations. These fluctuations originate from baryonic oscillations right before the recombination epoch. The CMB temperature fluctuation map measured by the Planck mission is shown in fig. 1.2.
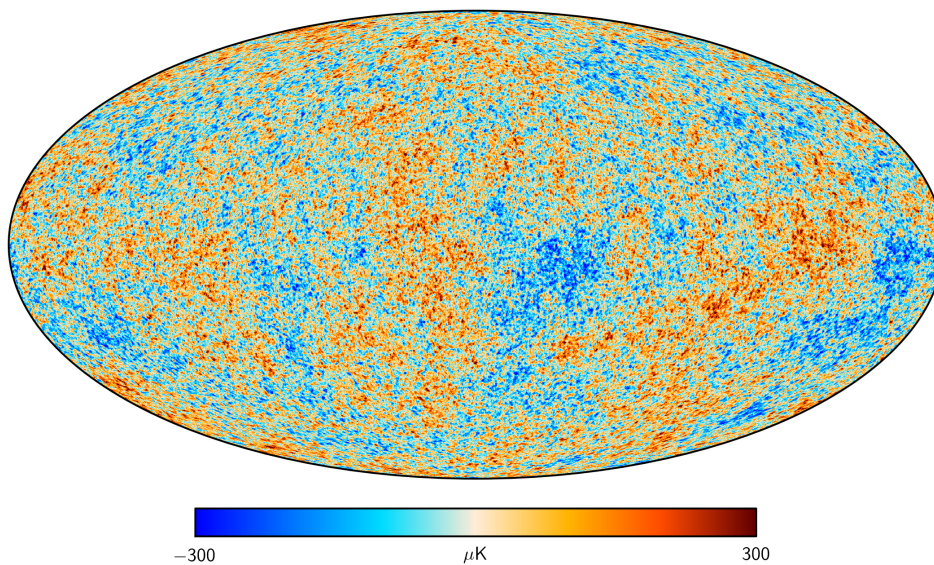

Figure 1.2.: Temperature fluctuations in the cosmic microwave background provided by the Planck mission. Image Credits: NASA/JPL-Caltech/ESA.

As mentioned earlier, the dark matter grew potential wells much earlier than the baryons, causing them to stream into these wells. Due to the compression of the

baryons, a radiation pressure built up, counteracting the gravitational force. At a certain point the radiation pressure took over the gravitation, pushing the baryons outwards, provoking them to oscillate within the potential wells. When the photons decoupled the different oscillation states of the wells were imprinted onto the CMB. Hence, the CMB encodes the physical conditions of the universe at the time of recombination. The observed fluctuations in the CMB imply a scale for the initial density fluctuations of the universe.

Fig. 1.3 shows the temperature power spectrum of the CMB measured by the planck mission (Planck Collaboration et al., 2015). Each peak represents a different oscillation state. Their height and position constrain the cosmological parameters appearing in the evolution equation for the scale factor in eq. 1.9.

The model described above combining dark matter, baryons and the cosmic expansion is the present-day accepted framework for structure formation and is called the ΛCDM model.
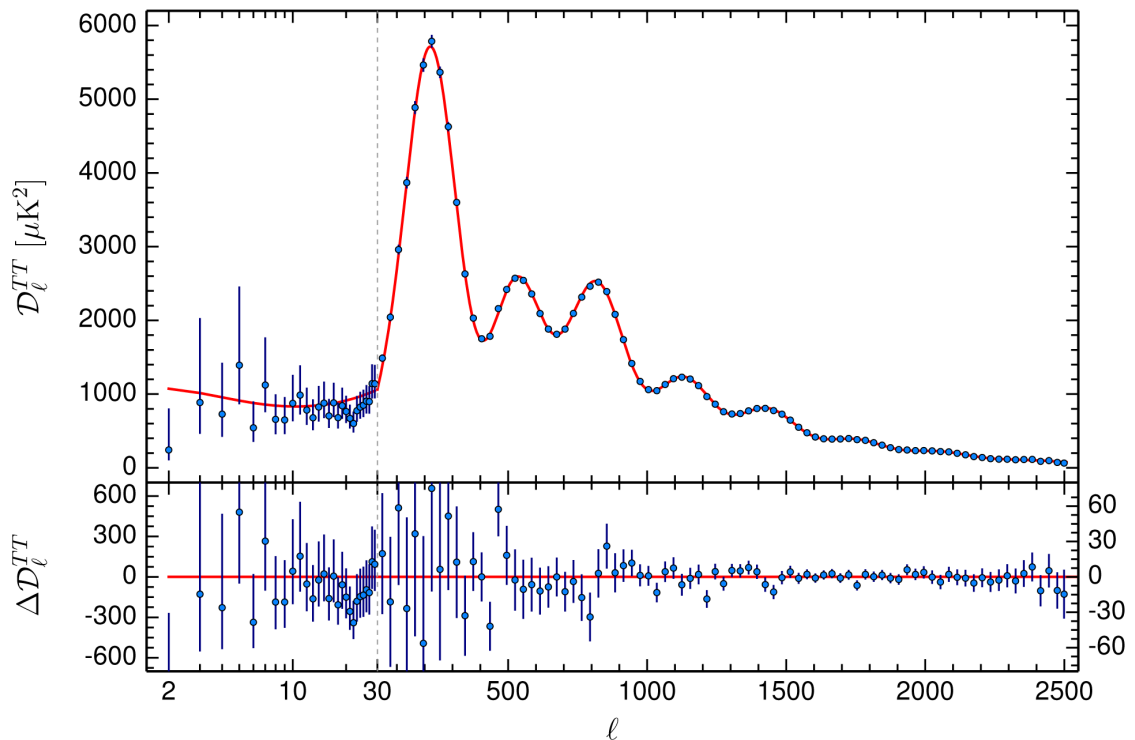

Figure 1.3.: Taken from Planck Collaboration et al. (2015): Upper Panel: Temperature power spectrum from the Planck data indicated by blue circles with the best fitting λCDM model as red line. Lower Panel: Residuals with respect to this model. The error bars show $\pm 1\sigma$ uncertainties.

1.2.2. Galaxy Formation at Lower Redshifts

Within the ΛCDM framework, after the formation of the first protogalaxies the structure formation progresses in a hierarchical manner. The dominating component of this process is the dark matter because of its commanding gravitational attraction. Through merging of smaller dark matter structures larger structures build up which continuously accrete gas thereby gaining angular momentum. Due to the ability of the gas to radiate away energy and redistribute angular momentum, it cools to the centre. Ongoing gas accretion increases the density in the centre and thus trigger star formation of Population III stars.

The merger and accretion history of galaxies at lower redshifts is effectively encoded in their star formation history. Present-day galaxies can be broadly divided into two main classes, namely star-forming (gas-rich) and quiescent (gas-poor). A model describing mass assembly of galaxies has to account for this bimodality.

The star formation inside the galaxy is fuelled by ongoing infall of smaller structures and smooth gas accretion. The evolution of the star formation density measured from different wave bands is shown in fig. 1.4 indicating an increase of star formation until it peaks at $z \approx 2$. At this stage, quiescent galaxies have already formed, however, the main part is gas-rich and actively forming stars. (van de Sande et al., 2013; Whitaker, 2011; Brammer et al., 2011). In the range of $0 < z < 2$ the star formation density decreases, building up the red quiescent class. Hence, in the
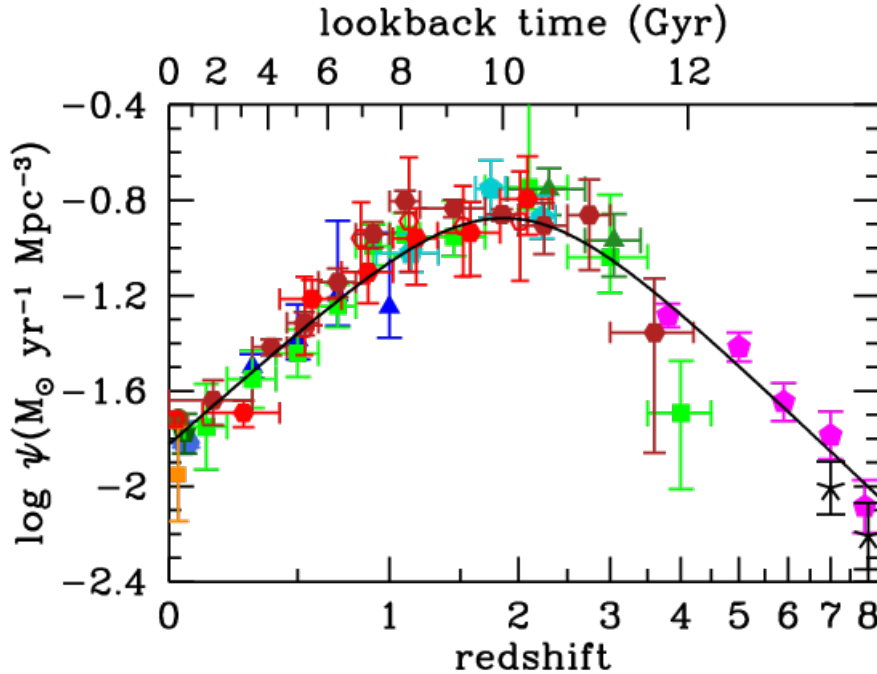

Figure 1.4.: Taken from Madau and Dickinson (2014): Evolution of cosmic star formation rate density from FUV+IR rest-frame measurements.

vicinity of the maximum star formation a physical mechanism is triggered driving galaxies towards the red sequence. In fact, it is a complex interplay of various effects which quench the star formation inside galaxies. Sudden removal of gas through outflows or stripping is one often proposed mechanism (Diamond-Stanic et al., 2012; Förster Schreiber et al., 2014; Cicone et al., 2014; Abadi et al., 1999). Another process is the so-called "strangulation", in which the gas supply halted causing the galaxy to "dry-out" (Peng et al., 2015).

Detailed cosmological simulations revealed a two-phase picture of mass accretion for $z \lesssim 3.5$ (Oser et al., 2010). In the first, rapid phase smooth cold gas gets accreted onto the galaxy centre through cold streams. Cold streams are narrow pipelines of cold gas reaching from the cosmic web directly into the galactic centre (Dekel et al., 2009).

The accretion time scales for this "cold mode" are much shorter than for the "hot mode", in which the gas initially is shock heated to the virial temperature of the surrounding hot halo. Therefore, cold streams supply cold gas for high star formation rates at early times, as found in fig. 1.4. Stars which are formed within the galaxy are called "in-situ". However, as the galaxy grows in mass, various feedback mechanisms quench the inflow of cold gas. This transition happens between $z \approx 1$ and $z \approx 2$. The redshift dependent interplay between hot and cold mode accretion is shown in fig.1.5. Below $z \approx 1.8$ cold streams exist, although the galaxy already exhibits a hot surrounding halo.

In a second, subsequent phase galaxies grow in mass and radius, primarily by accretion of stars through merger events. Stars accreted in this manner are called "ex-situ" stars, since they have formed in a different galaxy and only added to the forming central galaxy later on.

As the dominant mechanism, driving galaxy formation at low redshifts, galaxy mergers have a major influence on the morphology of an object. Especially in the context of ETG formation, various simulations showed that mergers of two LTGs can produce ellipticals (Gerhard, 1981; Hernquist, 1992; Burkert and Naab, 2003). Recent studies revealed that the outcome of a merger event is determined by fundamental properties of the progenitor galaxies: mass ratio, orbital parameter, morphologies and the gas fractions (Mo et al., 2010). However, not only the morphology is affected but also kinematical features like kinematically distinct or counter-rotating cores have formed in this manner (Bois et al., 2011; Tsatsi et al., 2015).
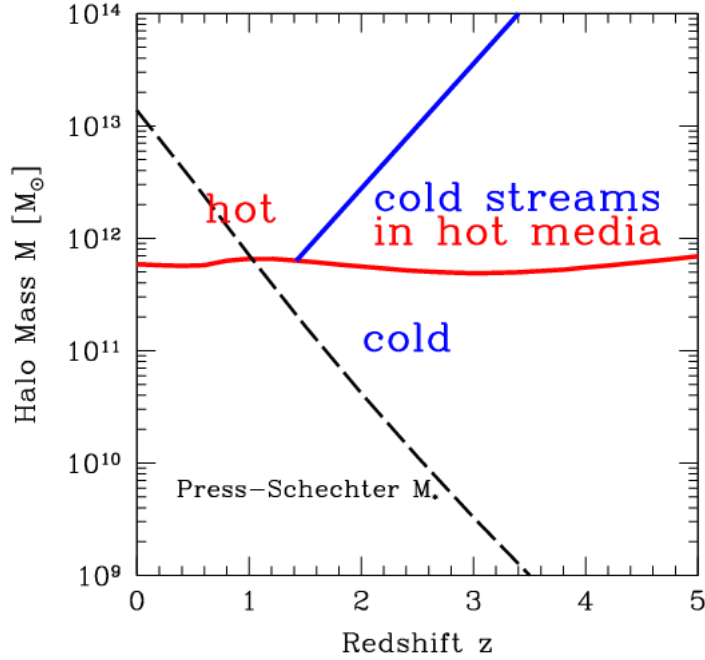
Figure 1.5.: Taken from Dekel and Birnboim (2006): Hot and cold mode accretion as function of redshift and halo mass. The nearly horizontal red curve marks the typical threshold for a hot halo. The inclined solid curve is the upper limit for the existence of cold streams in a hot halo. The dashed line shows the Press-Schechter estimates of the forming halo masses.

1.3. The Magneticum Pathfinder Simulations

The galaxies investigated in this study are extracted from the Magneticum Pathfinder simulations, which are a set of cosmological hydrodynamical simulations performed with the Tree/SPH code GADGET-3. GADGET-3 is an extended version of GADGET-2 (Springel, 2005; Springel et al., 2001b) including improvements concerning the treatment of viscosity and the used kernels (Dolag et al., 2005; Beck et al., 2015).

To investigate the kinematics of galaxies, a detailed treatment of the underlying baryonic physics is required. Therefore, our simulations include a wide variety of baryonic physics such as gas cooling and star formation (Springel and Hernquist, 2003), black hole seeding, evolution and AGN feedback (Springel et al., 2005; Hirschmann et al., 2014) as well as stellar evolution and metal enrichment (Tornatore et al., 2007).

The Magneticum Pathfinder simulations implement a standard ΛCDM cosmology with parameters adapted from the seven-year results of the Wilkinson Microwave Anisotropy Probe (WMAP7) (Komatsu et al., 2011). The density parameters are $\Omega_\mathrm{b} = 0.0451$, $\Omega_\mathrm{M} = 0.272$ and $\Omega_\Lambda = 0.728$ for baryons, matter and dark energy, respectively. The Hubble parameter is $h = 0.704$ and the normalisation of the fluctuation amplitude at 8Mpc is given by $\sigma_8 = 0.809$. The Magneticum Pathfinder

simulation set includes boxes of different sizes and resolutions. Sizes range from 2688Mpc/h box length to 18Mpc/h box length, while resolutions cover a particle mass range of $10^{10} > m_{dm} > 10^7 M_\odot/h$ for the dark matter and $10^9 > m_{gas} > 10^6 M_\odot/h$ for gas particles. The implemented star formation scheme allows a gas particle to form up to four star particles (Springel and Hernquist, 2003). A summary of all available boxes is given in tab. 1.1.

For this study we choose the medium-sized cosmological Box4, with a side length of 48Mpc/h at the ultra high resolution level from the various volumes and resolutions provided by the Magneticum Pathfinder simulations at a redshift of 0.1. The masses for the dark matter and gas particles are $m_{DM} = 3.6 \cdot 10^7 M_\odot/h$ and $m_{gas} = 7.3 \cdot 10^6 M_\odot/h$ respectively, with a gravitational softening length of 1.4kpc/h for dark matter and gas particles, and 0.7 kpc/h for star particles. This box is chosen to ensures a high enough resolution as well as a large sample size to examine the kinematics of galaxies in a statistically meaningful manner.

The haloes are detected using SUBFIND (Springel et al., 2001a) which utilises a standard Friends-of-Friends algorithm, and is adapted for the treatment of the baryonic component (Dolag et al., 2009), which allows to identify satellite galaxies in addition to the central galaxies inside the main haloes. The virial radius of the main haloes is defined according to the density contrast based on the top-hat model.

Table 1.1.: Properties of available boxes contained in the Magneticum Pathfinder set. Values taken from the Magneticum Project homepage: www.magneticum.org.

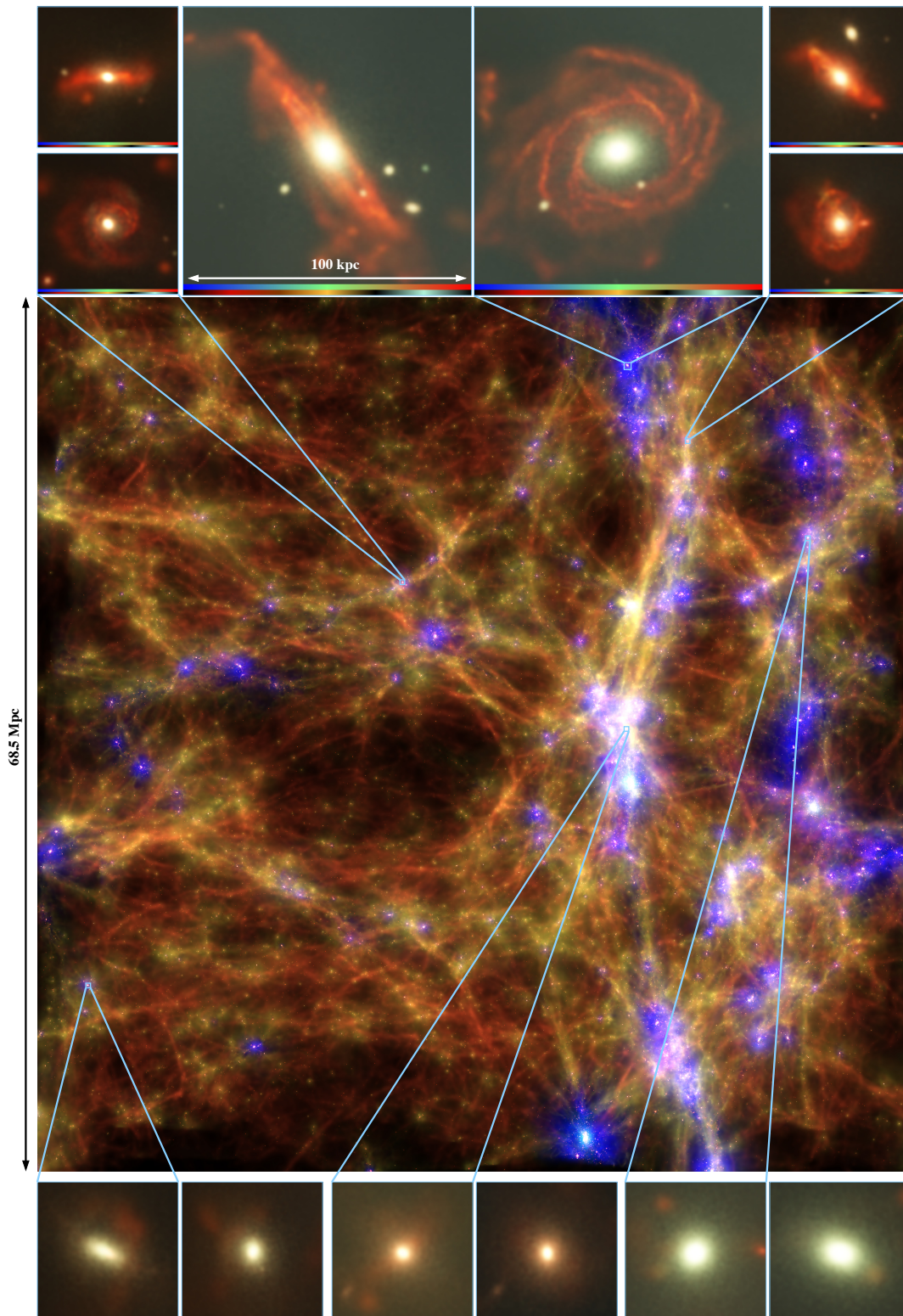|	Box0	Box1	Box2b	Box2	Box3	Box4	Box5
Size [Mpc/h]:	2688	896	640	352	128	48	18
N_{mr}:	$2 \cdot 4536^3$	$2 \cdot 1526^3$	–	$2 \cdot 594^3$	$2 \cdot 216^3$	$2 \cdot 81^3$	–
N_{hr}:	–	–	–	$2 \cdot 1584^3$	$2 \cdot 576^3$	$2 \cdot 216^3$	$2 \cdot 81^3$
N_{uhr}:	–	–	–	–	–	$2 \cdot 576^3$	$2 \cdot 216^3$

Figure 1.6.: Taken from Teklu et al. (2015): Main Panel: Complete simulated box at
redshift 0.5. The upper and lower panel show exemplary spiral and elliptical
galaxies that have formed in the box. In all panels the upper colour bar
represents the age of the stars from young to old, whereas the lower colour
bar indicates the gas temperature from cold to hot.

2. The λ_{R}-ϵ Plane

2.1. Definition of a New Kinematical Parameter

For many years the V/σ-parameter has been used to quantify the amount of observed stellar rotation in a system, where V and σ denote the projected stellar velocity and velocity dispersion, respectively. This parameter is a useful tool to investigate the dynamical state of early type galaxies. However, it fails to distinguish between small scale rotation like kinematically distinct cores and large scale rotation (Emsellem et al., 2007). Therefore, a new parameter needs to be introduced, which takes the global velocity structure into account and in addition maintains the information about the dynamical state, i.e. ordered vs. random motion.

Such a parameter was established by Emsellem et al. (2007) within the SAURON project, which aimed to investigate the intrinsic shape and structure of ETGs. For an observed velocity and dispersion map it is defined as

$$\lambda_R \equiv \frac{\langle R \ |V| \rangle}{\langle R \ \sqrt{V^2 + \sigma^2} \rangle},\tag{2.1}$$

where R is the radius, V the velocity and σ the stellar velocity dispersion. $\langle \cdot \rangle$ denotes the luminosity-weighted average over the full two-dimensional kinematic field, which is given by

$$\langle G \rangle = \frac{\sum_{i=1}^{N_p} F_i G_i}{\sum_{i=1}^{N_p} F_i}.\tag{2.2}$$

Therefore, if the brackets are written out, λ_R reads as

$$\lambda_R = \frac{\sum_{i=1}^{N_p} F_i \ R_i \ |\overline{V}_i|}{\sum_{i=1}^{N_p} F_i \ R_i \ \sqrt{\overline{V}_i^2 + \sigma_i^2}},\tag{2.3}$$

with the sum running over all pixels of the velocity and dispersion maps. F_i, R_i, $\left|\overline{V}_i\right|$ and σ_i are the flux, projected distance to the galaxy centre, mean stellar velocity and velocity dispersion of the ith photometric bin, respectively.

The normalisation by $(\overline{V}^2 + \sigma^2)^{1/2}$ implies that $\lambda_{\mathrm{R_e}}$ tends to one for purely rotational- supported systems. The lower limit of $\lambda_{\mathrm{R_e}}$ corresponds to either a purely dispersion-dominated system with no ordered rotation, or to a rotating system where the total angular momentum vector is along the line of sight. The usage of $\langle R |V| \rangle$ as a surrogate for the angular momentum ensures the distinction between large-scale

or little rotation.

It is important to mention that λ_{R_e} obviously depends on the spatial size, over which the sum in eq. 2.3 is taken. Moreover, it is sensitive to the tessellation method used for the velocity and dispersion maps. This will be discussed in more detail in sec. 2.3.1.

2.2. ATLAS^{3D}: **Sample Selection and Relevant Results**

The basis for the ATLAS^{3D} project is provided by the investigations within the SAURON project (Bacon et al., 2001). In the SAURON project the morphology and kinematics of 48 early-type galaxies were observed, providing detailed kinematical maps for the mean stellar line-of-sight-velocity $\overline{V}$ and the velocity dispersion σ, as well as for the higher Gauss-Hermite moments h_3 and h_4 (van der Marel and Franx, 1993; Gerhard, 1993). The moments h_3 and h_4 are used to parametrise the line-of-sight-velocity-distribution (LOSVD) f, measuring deviations from a single Gaussian function

$$f(y) \propto e^{-\frac{y^2}{2}}[1 + h_3 H_3(y) + h_4 H_4(y)] \tag{2.4}$$

where $y = (V - V')/\sigma$. Here, V', σ, h_3 and h_4 are independent fit parameters. $H_3(y)$ and $H_4(y)$ denote the third and fourth Hermite polynomial. Therefore h_3 and h_4 quantify the asymmetric and symmetric deviation of the LOSVD from a Gaussian.

As a result of this study, λ_{R_e} can be used to disentangle the two classes of fast and slow rotators with a threshold value of 0.1. Fast rotating ETGs show large-scale rotation and a regular pattern in their velocity maps. In contrast, slow rotators exhibit different kinematical features like counter-rotating or kinematically distinct cores with little rotation leading to lower λ_{R_e} values.

The ATLAS^{3D} project extends the SAURON sample to a total of 260 early-type galaxies supplying the same types of kinematical maps. While the ETGs in the SAURON sample were individually selected, the ATLAS^{3D} sample is only volume-limited ,that is all galaxies within a certain area of the sky below a certain luminosity ($M_B \lesssim -18.0$mag) were observed. From there the ETGs were identified and the kinematical maps of those ETGs were obtained. This method, in contrast to the SAURON survey, allows a more complete, statistical approach to understanding ETG kinematics. Tab. 2.1 summarizes the characteristics of the total ATLAS^{3D} sample, including the LTGs. A detailed description of the observational and selection process is given in Cappellari et al. (2011) and in sec. 2.4.

Having access to a statistically more meaningful sample, ATLAS^{3D} redefined the threshold between fast and slow rotators as:

$$\lambda_{R_e} > 0.31 \cdot \sqrt{\epsilon_e} \rightarrow \text{fast rotator}$$
$$\lambda_{R_e} \leq 0.31 \cdot \sqrt{\epsilon_e} \rightarrow \text{slow rotator}$$

where ϵ_{e} is the projected ellipticity which is defined as

$$\epsilon_{\mathrm{e}} \equiv 1 - \sqrt{\frac{\langle y^2 \rangle}{\langle x^2 \rangle}} = 1 - \sqrt{\frac{\sum_{i=1}^{N_p} F_i \, y_i^2}{\sum_{i=1}^{N_p} F_i \, x_i^2}} \tag{2.5}$$

(Cappellari et al., 2007), where the coordinates (x, y) are centred on the galaxy nucleus and x is measured along the photometric major axis. The subscript "e" indicates the aperture of one effective radius, which is adopted to calculate $\lambda_{\mathrm{R_e}}$.

Table 2.1.: Characteristics of the ATLAS$^{\mathrm{3D}}$ sample.

Distance:	$D < 42$ Mpc
Galaxy K-band luminosity:	$L > 8.2 \cdot 10^9 \; L_{K,M_\odot}$
Galaxy stellar mass:	$M_* \gtrsim 6 \cdot 10^9 \; M_\odot$
Galaxy B-band total mag:	$M_B \lesssim -18.0$ mag
Galaxy SDSS r-band total mag:	$M_r \lesssim -18.9$ mag
Total number of galaxies:	$N_{gal} = 871$
Spiral and irregular galaxies:	$N_{sp} = 611 \; (70\%)$
S0 galaxies:	$N_{S0} = 192 \; (22\%)$
Elliptical galaxies:	$N_E = 68 \; (8\%)$

Thus, this separation also uses the morphological parameter ϵ_{e}. This new proxy is motivated by the effect of inclination on the classification scheme. A fast rotator seen face-on shows very low rotation and round shape. If one uses the constant 0.1 criterion this leads to a misclassification of the galaxy as a slow rotator. The new criterion is significantly more robust with respect to inclination effects (Emsellem et al., 2011). Although this relation is determined empirically, the $\sqrt{\epsilon_{\mathrm{e}}}$ dependence somewhat mocks the change of λ_{R_e} and the flattening of ETGs due to inclination effects.

2.3. Calculating $\lambda_{\mathrm{R_e}}$ in Numerical Simulations

The previously established parameter $\lambda_{\mathrm{R_e}}$ is specifically customised to fit the needs and constraints of the current observational methods. It solely uses projected quantities and fluxes, which can be observed by multi-wavelength surveys. Quantities like the spatial angular momentum $\mathbf{j} = m\mathbf{r} \times \mathbf{v}$, which require three dimensional information, can not be observed directly.

Since we obtained our data from the cosmological Magneticum Pathfinder simulations, i.e. we have full three dimensional information and masses of particles but no luminosities, it is necessary to adapt both eq. 2.3 as well as the tessellation method.

The expression for λ_{R_e} is transformed into

$$\lambda_R = \frac{\sum_{i=1}^{N_p} M_i \ R_i \ |\overline{V}_i|}{\sum_{i=1}^{N_p} M_i \ R_i \ \sqrt{\overline{V}_i^2 + \sigma_i^2}}. \tag{2.6}$$

The flux F_i is replaced by the mass inside the ith bin, assuming a constant light-to-mass-ratio. Eq. 2.6 is the final formula we will use in this study to calculate λ_{R_e} from the kinematical maps.

In the same way we modify eq. 2.5 for the projected ellipticity

$$\epsilon_e = 1 - \sqrt{\frac{\sum_{i=1}^{N_p} M_i \ y_i^2}{\sum_{i=1}^{N_p} M_i \ x_i^2}}. \tag{2.7}$$

The construction of kinematical maps from simulated data is not a trivial task. To be comparable to observations we have to use calculation methods which takes the properties of numerical simulations into account.

For example, the limited mass resolution in SPH leads to low particle numbers when assigning particles onto a grid which causes statistical problems. Another issue is the limited spatial resolution making the maps sensitive to numerical small-scale fluctuations. For a detailed resolution study see Bois et al. (2010).

Since we aim to calculate λ_{R_e} given in eq. 2.6, we need to generate two types of kinematical maps. The mean projected velocity $\overline{V}_i$ within a cell given by

$$\overline{V}_i = \frac{\sum_{j=1}^{N_c} V_j}{N_c} \tag{2.8}$$

where V_j is the particle velocity and the sum runs over all N_c particles within a cell. And the projected velocity dispersion defined as

$$\sigma_i = \sqrt{\frac{\sum_{j=1}^{N_c} V_j^2}{N_c} - \left(\frac{\sum_{j=1}^{N_c} V_j}{N_c}\right)^2}. \tag{2.9}$$

2.3.1. Tessellation Methods

The first crucial step when calculating kinematical maps is to choose an appropriate tessellation scheme. When we evaluate $\overline{V}_i$ for each grid cell we have to address the issue of low number statistics. We can estimate the statistical quality of the arithmetic mean for each grid cell via the so-called standard error of the mean (SEM).

If n_s is the size and σ_s the standard deviation of the sample, which is used to

estimate the population mean, the SEM is given by

$$SEM = \frac{\sigma_{\mathrm{s}}}{\sqrt{n_s}}. \tag{2.10}$$

This quantity is the standard deviation of all possible sample means that can be drawn from the complete population. The denominator $\sqrt{n_s}$ implies that a larger sample size diminishes the SEM.

Due to the mass resolution in SPH simulations, which can cause low particle numbers per cell, this statistical error is artificially introduced. To investigate the effects of various tessellation schemes and resolutions we compare three different methods with respect to the impact on the $\lambda_{\mathrm{R_e}}$-parameter.

Simple Rectangular Grid and Triangulate Shaped Cloud

In this study we use two tessellation methods that are based on a quadratic rectangular grid. After determining the spatial geometry, we have the freedom to choose a window function. The window function determines which particles around a grid point are assigned to it, and how these particles are weighted.

The most basic window function is the nearest grid point (NGP). In one dimension it is given by

$$W_{\mathrm{NGP}}(x_i) = \begin{cases} 1, & |x_i| < 0.5, \\ 0, & \text{otherwise.} \end{cases} \tag{2.11}$$

where x_i is the distance to the considered grid point, given in units of the lattice constant A. From the shape of $W_{\mathrm{NGP}}(x_i)$ in fig. 2.1 we deduce that all particles within an interval of length A around a grid point are assigned to it. Generalising the NGP window function to two dimensions, every particle inside a quadratic cell with side length A around a grid point will be sampled to it.

Another commonly used window function is the triangular-shaped cloud (TSC):

$$W_{TSC}(x_i) = \begin{cases} 0.75 - x_i^2, & |x_i| < 0.5, \\ \dfrac{(1.5 - |x_i|)^2}{2}, & 0.5 < |x_i| < 1.5, \\ 0, & \text{otherwise.} \end{cases} \tag{2.12}$$

Hence, in one dimension the sample range is three times the lattice constant. The weight of a particle decreases quadratically with increasing distance to the grid point.

Switching from one to two dimensions the sampling area is a square with a side length of three times the lattice constant. The weights are multiplied according to

the distance from the grid point in both directions leading to:

$$
W_{TSC}(x_i, y_i) = \begin{cases} (0.75 - x_i^2) \cdot (0.75 - y_i^2), & |x_i| < 0.5 \text{ and } |y_i| < 0.5, \\[2mm] \dfrac{(1.5 - |x_i|)^2}{2} \cdot (0.75 - y_i^2), & 0.5 < |x_i| < 1.5 \text{ and } |y_i| < 0.5, \\[2mm] (0.75 - x_i^2) \cdot \dfrac{(1.5 - |y_i|)^2}{2}, & |x_i| < 0.5 \text{ and } 0.5 < |y_i| < 1.5, \\[2mm] \dfrac{(1.5 - |x_i|)^2}{2} \cdot \dfrac{(1.5 - |y_i|)^2}{2}, & 0.5 < |x_i| < 1.5 \text{ and } 0.5 < |y_i| < 1.5, \\[2mm] 0, & \text{otherwise.} \end{cases}
$$
(2.13)

We use this window function in order to smooth the mass of a particle over nine grid points, while conserving its total mass. In this manner we improve our statistics at each grid cell by a factor of nine, hence decreasing the SEM (see sec. 2.3.1).
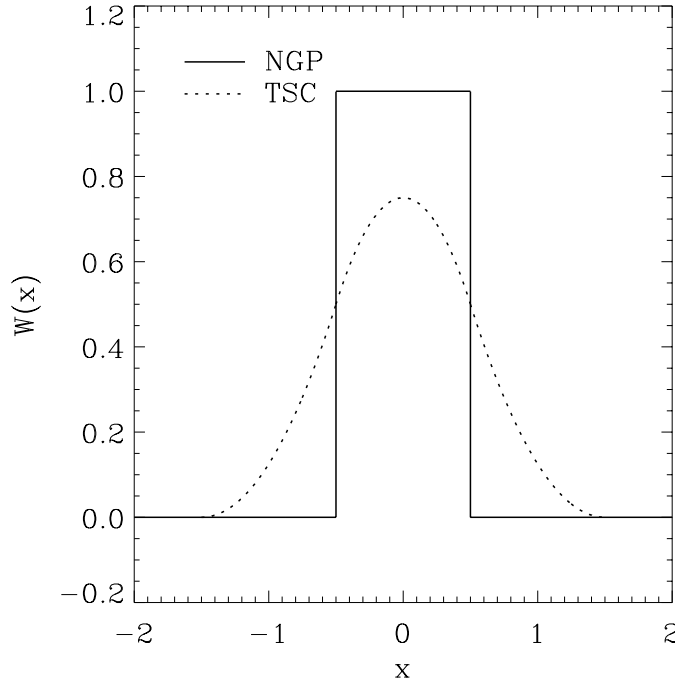

Figure 2.1.: One dimensional window function for NGP (solid line) and TSC (dashed line). The x-axis is in units of lattice constant A.

Since this method samples the mass of a particle over more than one grid cell we have to adapt the expressions for the mean velocity and the velocity dispersion at each grid point:

$$
\overline{V}_i = \frac{\sum_{j=1}^{N_c} W_{\mathrm{TSC}}(x_j, y_j) m_j V_j}{\sum_{j=1}^{N_c} W_{\mathrm{TSC}}(x_j, y_j) m_j},
$$
(2.14)

$$\sigma_i = \sqrt{\frac{\sum_{j=1}^{N_c} W_{TSC}(x_j, y_j) m_j V_j^2}{\sum_{j=1}^{N_c} W_{TSC}(x_j, y_j) m_j} - \left(\frac{\sum_{j=1}^{N_c} W_{TSC}(x_j, y_j) m_j V_j}{\sum_{j=1}^{N_c} W_{TSC}(x_j, y_j) m_j}\right)^2}, \qquad (2.15)$$

where the sum runs over all particles within the sampling area. The kinematical maps calculated with these expressions are then used to derive λ_R.

Centroidal Voronoi Tessellation Scheme

The third tessellation method we will use in this study is the so-called centroidal voronoi tessellation (CVT). It was introduced by Cappellari and Copin (2003) and primarily developed to tessellate integral-field spectroscopic images into bins with a signal-to-noise-ratio above a certain threshold while retaining a maximum spatial resolution.

Since we obtain data from a numerical simulation, we are dealing with statistical noise due to the SEM rather than with observational noise. Thus we adapt the method of CVT to generate a tessellation with nearly equal-particle-number bins in the range of a chosen target-particle-number N_T. In contrast to the pure NGP- and TSC-Method this ensures a constant statistical error per bin below a value determined by N_T.

A good tessellation scheme should fulfil some basic requirements. Let Ω be the 2D particle distribution area, already tessellated with the NGP-Method. The term "pixel" refers to the cells of the NGP binning, whereas "bin" refers to the actual voronoi cell.

- **Topological Requirement**: the tessellation should construct a partition of Ω without any cavities or overlapping.

- **Morphological Requirement**: the bin shape should be as "round" as possible, such that the pixels in one bin are as close as possible to each other. In that manner the best spatial resolution is implemented and it is possible to assign a well defined spatial position to each bin. To measure the roundness of a bin we use the parameter

$$R = \frac{r_\mathrm{max}}{r_\mathrm{eff}} - 1 \qquad (2.16)$$

  where r_max is the maximum distance to any pixel of the bin and r_eff the radius of a circle with the same area as the bin. Cappellari and Copin (2003) obtained good results for $R < 0.3$, thus we adapt the same value.

- **Uniformity Requirement**: the scatter around N_T should be as small as possible while not sacrificing the spatial resolution.

A general Voronoi tessellation (VT) of an area Ω is uniquely determined by a set of points $\{z_i\}_{i=1}^N$ called generators. A VT is a segmentation of Ω into regions $\{V_i\}_{i=1}^N$, enclosing the pixels closer to z_i than to any other generator. In the special class

of Centroidal Voronoi tessellation the generators coincide with the mass centroids according to the quantity which is desired to be constant (in our case the particle number). If one for example wants to create equal physical mass bins, the generators coincide with the physical mass centroids.

Such a partition naturally satisfies the topological requirement but none of the other requirements. Hence Cappellari and Copin (2003) developed an algorithm that also tackles the morphological and uniformity criterion. We will sketch this bin-accretion algorithm following Cappellari and Copin (2003) adapted to generate equal-particle-number bins:

i) Choose the pixel with the highest particle-number N_i.

ii) Compute geometrical centroid of the current bin and select the closest unbinned pixel as candidate for addition to the current bin.

iii) If the following criteria are satisfied add the pixel to the bin and go back to ii)

    a) The new pixel is adjacent to the current bin (topological criterion).

    b) Adding the pixel would not cause the roundness R to exceed the chosen threshold (morphological criterion).

    c) By adding the pixel the N_i will get closer to the desired N_{T} (uniformity criterion).

iv) The accretion has come to an end if the S/N is above a certain fraction of N_{T}.

v) Again calculate the geometric centroid of the pixels in the current bin and select the nearest unbinned pixel as starting point for a new bin. Go back to ii) until all pixels are binned.

vi) Evaluate the geometric centroid of each successful bin and assign the unbinned pixels to the closest centroid.

vii) Recalculate the geometrical centroids.

The centroids obtained from this process can directly be used as generators to perform a VT, giving already good results (Cappellari, 2009).

In this study we use a second procedure starting from the calculated centroids and performing a CVT. This bin-regularisation uses a modified Lloyd algorithm to generate a CVT with the generators coincide with the mass centroids, rather than the geometrical centroids (Cappellari, 2009; Cappellari and Copin, 2003).

An example for a CVT of a simulated galaxy is given in fig. 2.2 with $N_{\mathrm{T}} = 150$. The green crosses indicate the positions of the generators, while the particles positions are represented by red dots. Filling colours of the cells are according to the particle numbers as given in the colour bar. The number and size of the cells clearly scale with the density, while properly satisfying the three requirements stated before. However, there is a certain scatter in the particle numbers between 111 and 231. Hence it is important to take this scatter into account when choosing a target-particle-number.
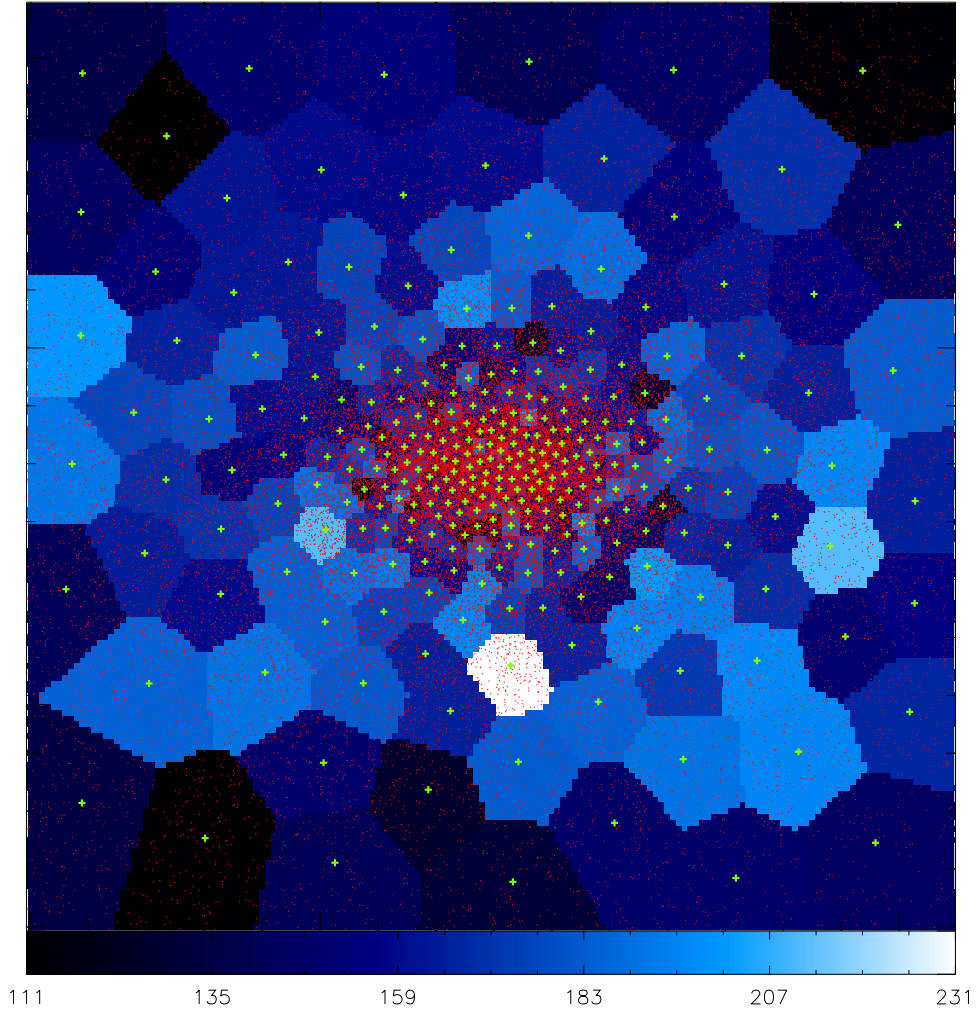
Figure 2.2.: Exemplary Centroidal Voronoi Tessellation of a random galaxy from the Magneticum sample. Filling colours correspond to the particle number per cell. The stellar particle positions are indicated by red dots, while green crosses mark the position of the generators.

2.3.2. Probing Tessellation Methods

After introducing three different tessellation schemes we now investigate their stability. For this purpose we select a random galaxy from our sample and trace its path in the λ_{R_e}-ϵ_e plane when going from the edge-on to the face-on projection. We always use a square with a side length of two effective radii centred on the centre-of-mass of the galaxy as the field of view to calculate λ_{R_e}. It is not intended to conduct any physical interpretation in this section, we only focus on the behaviour of the tessellation methods.

For the NGP and TSC method the free parameter to vary is given by the number of grid cells N_{cell}. Generally, it is possible to use a different cell number for each spatial direction, i.e. non-quadratic grid cells can be generated. However, we restrict ourself to quadratic cells. The CVT method has two free parameters, namely the cell number of the the underlying NGP and the desired target-particle number. To exclusively investigate the impact on λ_{R_e} the parameters to determine ϵ_e are held constant for all 40 projections.

Fig. 2.3 shows the paths in the λ_{R_e}-ϵ_e plane for five different N_{cell}, distinguishing the tessellation schemes by colour.
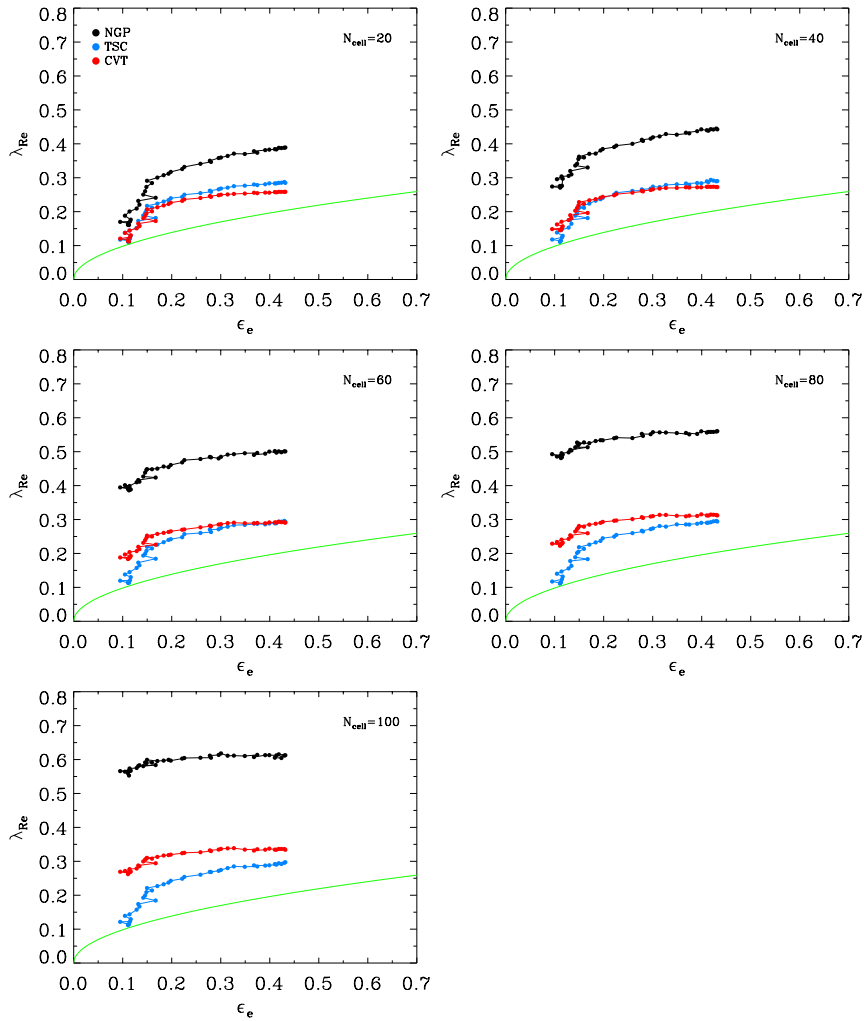

Figure 2.3.: Each panel shows tracks in the λ_{R_e}-ϵ_e plane when going from the edge-on to the face-on projection for the same galaxy. From left to right, top to bottom the cell number N_{cell} increases by 20. The colours represent the three tessellation methods as given in the legend. The green solid line marks the threshold between fast and slow rotators, i.e eq. 2.5.

For $N_\mathrm{cell} = 20$ and $N_\mathrm{cell} = 40$ the CVT and TSC are in good agreement, whereas the NGP already shows significantly larger values. When going to even higher N_cell this trend continues until the NGP is approximately a factor 2 higher than the CVT. A similar, however weaker, trend can be observed when comparing the CVT and TSC method: The TSC curve shifts away from the CVT line to larger values for increasing N_cell. The behaviour of the TSC and NGP scheme can be explained by by the decreasing number of particles per cell for larger N_cell, causing the statistical noise on $\overline{V}_i$ to increase.

As expected, only the CVT curve stays constant for all five N_cell, implying stability with respect to changing N_cell. This result emphasises one of the major advantages of a CVT: All cells contain approximately the same number of particles, ensuring a constant as well as low statistical error.

In order to examine the effect of a varying N_T on the CVT, we again calculate the paths in the $\lambda_{\mathrm{R}_\mathrm{e}}$-$\epsilon_\mathrm{e}$ plane, now for five different N_T. We adapt an underlying NGP with $N_\mathrm{cell} = 60$ for all five paths. From Fig. 2.4 we conclude that the CVT method is stable across a large range of target-particle numbers. The curve shifts only little when lowering N_T, especially for $N_\mathrm{T} > 200$ the deviations are very small. Although an increasing N_T improves the statistical noise, it is not reasonable to employ extremely large values, due to the larger extend of the cells leading to a reduced spatial resolution.

Based on the considerations in this section, we select the CVT method for this study adopting $N_\mathrm{T} = 150$. For the underlying NGP we choose $N_\mathrm{cell} = 60$, which is in agreement with the resolution within the ATLAS[3D] project. This ensures a low statistical noise as well as a proper spatial resolution.
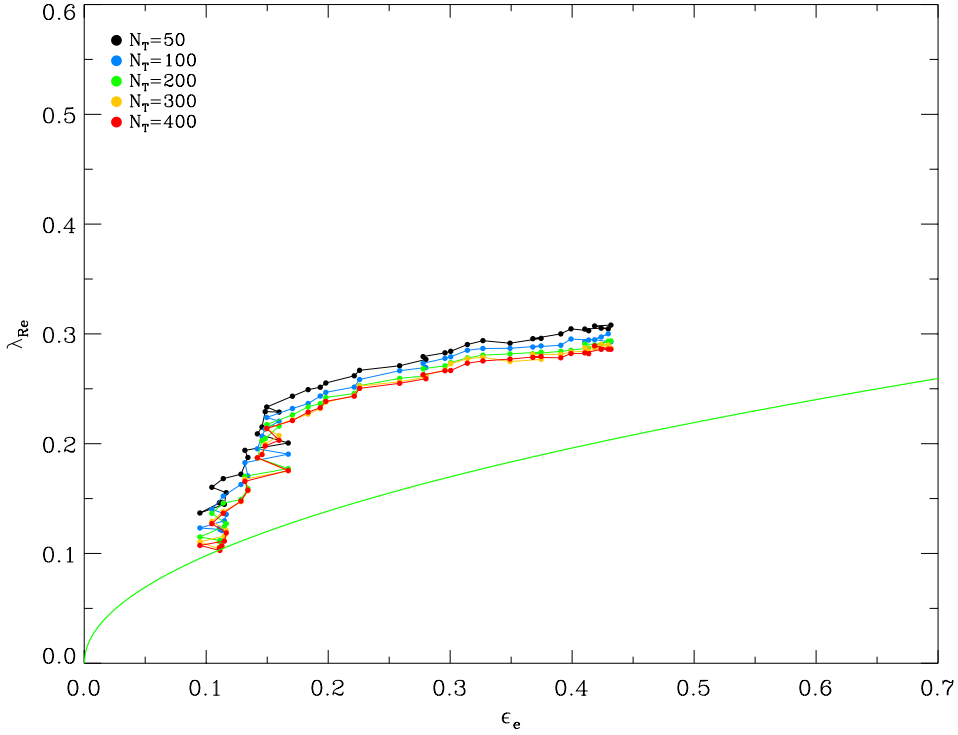
Figure 2.4.: Tracks in the λ_{R_e}-ϵ_e plane for the CVT method. Colours are according to different target-particle-numbers N_T as given in the legend. The green solid line represents eq. 2.5.

2.4. The Magneticum Galaxy Sample

Since we aim to conduct a statistical comparison to results which are based on the ATLAS^{3D} sample, the galaxy selection is a crucial step. Our galaxy selection algorithm should ensure a meaningful comparability as well as a large enough sample size.

The classification scheme used by ATLAS^{3D} is purely based on the morphological properties of a galaxy (Cappellari et al., 2011). Adopting the discrimination criterion between LTGs and ETGs outlined in Sandage (1961), they select ETGs from their complete sample by visually inspecting multi-colour images. Therefore, the galaxy selection is based entirely on the presence of spiral arms, while other galaxy characteristics, which vary with morphology, are neglected (Sandage, 1975). This is reasonable, because a further devision into the subclasses E0-E7 is not intended.

Because of the potentially large sample size and the challenging task of generating realistic multi-colour images, a visual inspection is not convenient for our study. Hence we use a simple automatic process to select our sample from the complete simulated box: We first select all main- and subhaloes identified by SUBFIND with a total stellar mass $M_* > 1 \cdot 10^{10} M_\odot$. In this manner the se-

lected galaxies are properly resolved in terms of mass resolution. Furthermore this threshold is in the range of the lower limit $M_* \gtrsim 6 \cdot 10^9 M_\odot$ chosen for the ATLAS^{3D} galaxies. In total, we find 2112 galaxies above this mass in Magneticum Box4.

The presence of spiral arms is tightly coupled to the amount of cold gas contained in a galaxy. Young et al. (2014) investigated the cold gas contend for the ATLAS^{3D} ETG sample, observing M_{HI}/M_*-fractions ranging from 10^{-1} to 10^{-4}. Therefore, we adopt the selection criteria

$$f_{\text{gas}} = \frac{M_{\text{gas,cold}}}{M_*} \leq 0.1 \qquad (2.17)$$

rather than visually identifying spiral arms. In addition, we constrain the effective radius to be larger than 1.4 kpc (i.e. twice the stellar softening length) to ensure a proper spatial resolution. Our final sample therefore includes 1334 galaxies, which we will refer to as the "Magneticum sample" in the following. Some characteristics of our sample are summarised in Tab.2.2.

Table 2.2.: Characteristics of the Magneticum sample.

Total number of ETG's:	1334
Galaxy stellar masses:	$1 \cdot 10^{10} - 9.7 \cdot 10^{11}\ M_\odot$
Galaxy cold gas fractions:	$3 \cdot 10^{-5} - 0.09$
Galaxy effective radii:	$1.58 - 30.5$ kpc
Galaxy gas masses:	$0 - 3.1 \cdot 10^{12}\ M_\odot$
Total halo masses:	$1.1 \cdot 10^{10} - 4.0 \cdot 10^{13}\ M_\odot$

To further motivate our sample selection, we follow results of Cappellari et al. (2013) and Shen et al. (2003). For a given stellar mass they observe a larger effective radius for LTGs compared to ETGs on average (see fig. 9 and fig. 14 in Cappellari et al. (2013)). Cappellari et al. (2013) used the complete (also including LTGs) sample described in sec. 2.2 in their study.

To review the Magneticum sample in the view of these results, fig. 2.5 shows the mass-size relation for each galaxy. Galaxies that are selected to resemble ETGs are shown in red, those that were discarded from our sample are shown in blue. The latter includes disc-like galaxies as well as peculiar galaxies and ongoing merger. In the mass stellar range $10^{10} - 10^{11} M_\odot$ we clearly see the separation stated above between the selected spheroidal galaxies and rejected galaxies with an significant overlap as found in the observations. At the high mass end the split up becomes less evident. Small deviations from the observations in Cappellari et al. (2013) might be due to the low number of galaxies observed in this range. However, overall the mass-size relation found for the Magneticum sample is consistent with the observations in Cappellari et al. (2013) as well as the results from the GAMA survey (Baldry et al., 2012).
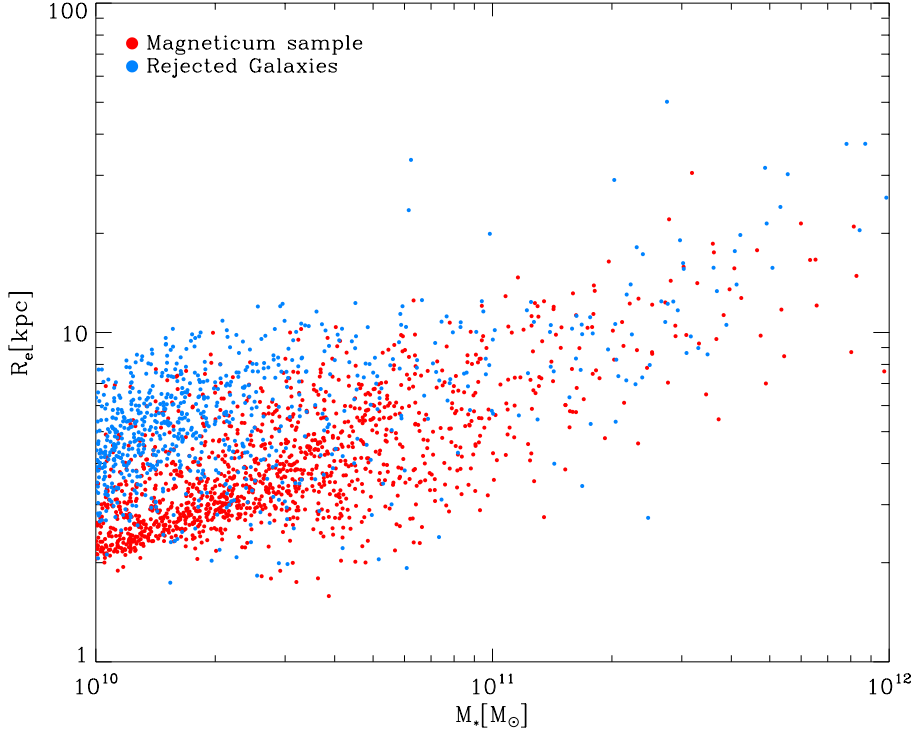
Figure 2.5.: The mass-size distribution for all galaxies with $M_* > 1 \cdot 10^{10} M_\odot$ and $R_e >$ 1.4 kpc. Colours separate selected and rejected galaxies as given in the legend.

2.5. The λ_{R_e}-ϵ_e Plane in the Magneticum Simulation

In this section we investigate the λ_{R_e}-ϵ_e plane for the sample described in Sec. 2.4 and compare it directly to ATLAS[3D].

Since the galaxies in the observational sample are observed in a random projection, an arbitrary projection is selected to calculate λ_{R_e} and ϵ_e to avoid a possible bias. As mentioned in sec. 2.1, λ_{R_e} depends on the spatial area which is considered for the calculation. In practice, we start by calculating the ellipticity according to eq. 2.5. Knowing ϵ_e and the effective radius R_e, the calculation area is determined to be an ellipse with ϵ_e and a surface of $A_{\mathrm{ellipse}} = \pi R_e^2$. This procedure ensures maximal comparability to observational results (Emsellem et al., 2007).

2.5.1. Magneticum Galaxies in the λ_{R_e}-ϵ_e Plane

To get a sense for the concept of λ_{R_e}, fig. 2.6 illustrates the λ_{R_e}-ϵ_e plane for all galaxies in the simulated box satisfying $M_* > 1 \cdot 10^{10} M_\odot$ decomposed into the Magneticum sample and rejected galaxies.
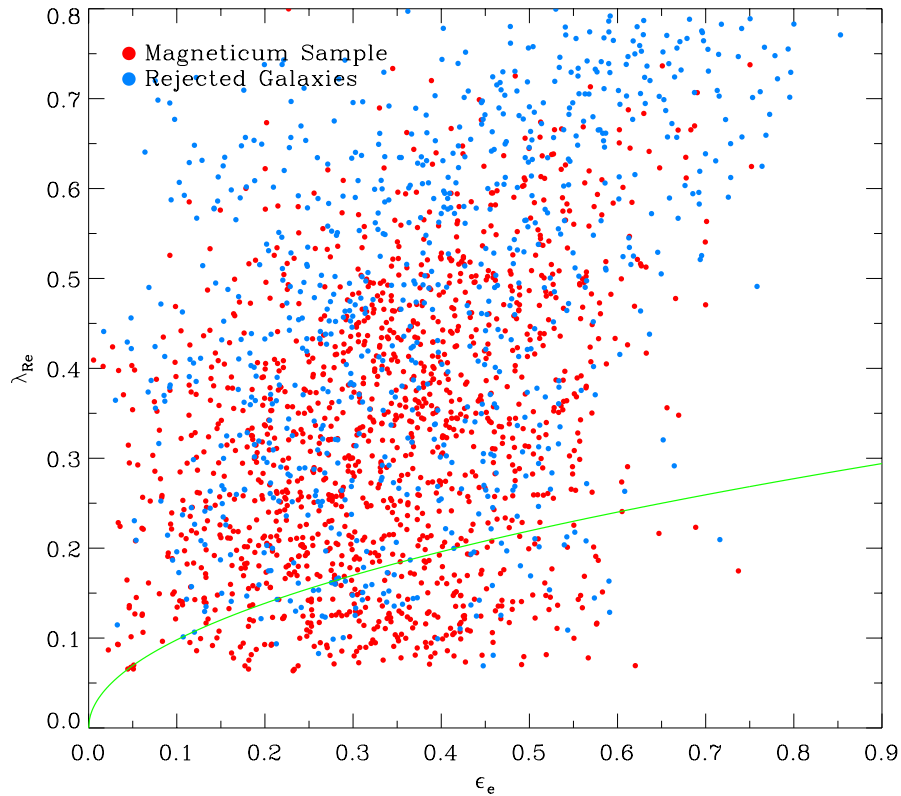
Figure 2.6.: λ_{R_e}-ϵ_e plane for Magneticum galaxies with $M_* > 1 \cdot 10^{10} M_\odot$. Colours sepa-
rate the Magneticum sample (red) and the rejected galaxies (blue) according
to sec. 2.4. The green line defines the threshold between fast and slow ro-
tators given in eq. 2.5.

Overall, the rejected galaxies clearly show higher λ_{R_e} values, as expected for poten-
tial LTGs. Hence, fig. 2.6 further verifies our sample selection. Of course inclination
effects can cause low λ_{R_e} for LTGs, furthermore external interaction can diminish
λ_{R_e} for gas-rich objects.

The most extreme case of inclination effects can be seen in fig. 2.7, where we show
the λ_{R_e}-ϵ_e plane for the edge- and face-on projection of the Magneticum sample.

As expected, the distribution shifts significantly from the lower left to the upper
right corner. A large amount of galaxies, which are classified as slow rotators in the
face-on projection, cross the green line, whereas only few fast rotators go the reverse
way. This behaviour follows the basic idea of λ_{R_e}, however clearly showing its limits
in terms of inclination, especially with respect to the slow rotator family.

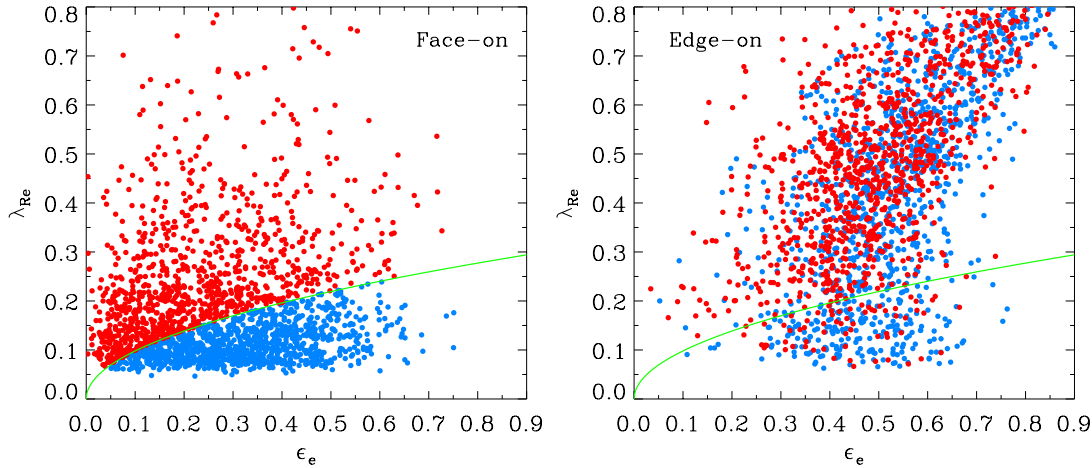**Figure 2.7.:** λ_{R_e}-ϵ_e plane for the Magneticum sample. The left panel shows the face-on projection, whereas the right panel illustrates the edge-on projection. Colours separate fast (red) and slow (blue) rotators, according to the face-on projection. The green line represents eq. 2.5.

2.5.2. Comparison to ATLAS[3D] and CALIFA Observations

The comparison sample contains the ATLAS[3D] sample (see sec.2.2) and observations from the CALIFA survey (Sánchez et al., 2012) extracted form Querejeta et al. (2015).

Fig. 2.8 shows the λ_{R_e}-ϵ_e plane for our sample as well as for the observational sample. The Magneticum simulation forms fast as well as slow rotating early-type galaxies with λ_{R_e} and ϵ_e in the range $0.06 < \lambda_R < 0.84$ and $0.005 < \epsilon_e < 0.75$, respectively. With 83% (1103/1334) the vast majority is classified as fast rotators, accordingly only 17% (231/1334) are slowly rotating. The appearance of both types is in almost perfect agreement with the ATLAS[3D] observations, where 86% (224/260) are fast rotators and 14% (36/260) are slow rotators (Emsellem et al., 2011).

The overall distribution covers almost the complete observational range except for the lowest λ_{R_e} values. However, this is not a physical issue, since it is due to the nature of calculating λ_{R_e} from simulated data. As λ_{R_e} is a cumulative parameter of absolute values, the statistical noise of voronoi cells with nearly zero velocity adds up creating a lower limit for λ_{R_e} (Naab et al., 2014). We verified this notion by calculating λ_{R_e} for all galaxies assuming zero velocity, only considering the statistical noise. It revealed a mean value of 0.07, which corresponds to the lower values found for the simulation in fig. 2.8.

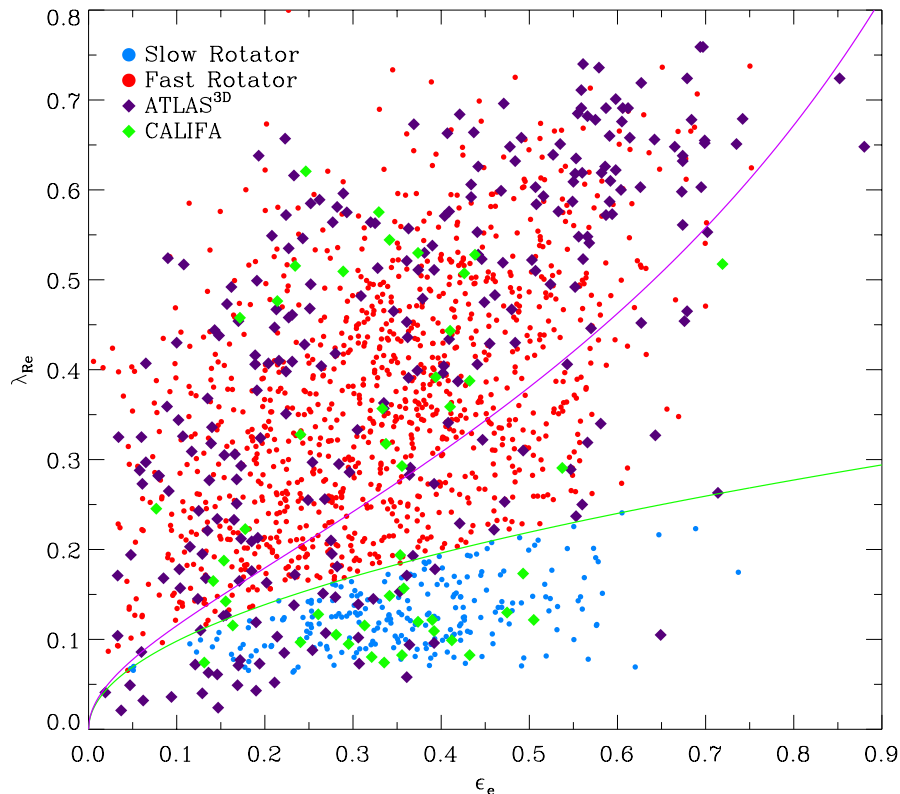Similar to the observations, we see a fairly well defined upper envelope: as ϵ_e

Figure 2.8.: Comparison of the Magneticum sample with ATLAS[3D] and CALIFA observations in the λ_{R_e}-ϵ_e plane. Filled circles indicate the Magneticum sample, whereas the filled diamonds mark the observations. The green line defines the threshold between fast and slow rotators given in eq. 2.5. The lilac line shows the theoretical position of an edge-on viewed ellipsoidal galaxy with an anisotropy parameter $\beta = 0.70 \times \epsilon$ (for further details see Cappellari et al. (2007)).

increases, the maximum λ_{R_e} increases accordingly. In the slow rotating regime we tend to have larger ellipticities than the observations. While ATLAS[3D] includes only one slow rotator with $\epsilon_e > 0.4$, we find several slow rotators in the Magneticum sample with flatter ellipticities. The CALIFA survey, however, finds already five slow rotators with ellipticities flatter than 0.4. Nevertheless, although there are observed galaxies in this range, a larger number is found in the Magneticum sample. If this slight disagreement is caused by insufficient physics implemented in the simulation needs to be checked by comparing to a more complete observational sample.

The fast rotating domain is in substantial agreement with the observations, showing only minor deviations in the range of extremely large ϵ_e near 0.9, where we do not find any galaxy. Several former studies investigated the formation of fast and slow rotating ellipticals in simulations through isolated merging events (Jesseit et al., 2009; Naab et al., 2014; Moody et al., 2014; Bois et al., 2010, 2011). Although

they were able to produce both kinematical types, they did not reach the regime of $\lambda_{R_e} > 0.65$. Since we obtain our data from a fully cosmological simulation, this is a hint for a different formation process forming high λ_{R_e} ETGs that is only present in a cosmological framework. Effects like strangulation and ram-pressure-stripping of LTGs are candidates for these processes (Peng et al., 2015; Abadi et al., 1999).

Overall, the galaxies in the Magneticum sample resemble the λ_{R_e}-ϵ_e plane observed by the ATLAS[3D] and CLAIFA projects in a remarkable manner implying a proper treatment of physical processes influencing the formation of fast and slow rotating ETGs. Only in the extreme low λ_{R_e} range we are not able to make a meaningful statement due to the limitations by statistical noise aforementioned.

To further investigate the consistency with observations, we plot the mass distribution within the λ_{R_e}-ϵ_e plane for our sample (upper panel) in direct comparison to results found by Emsellem et al. (2011) (lower panel) in fig. 2.9. The size and colour of the symbols is chosen accordingly to the mass as given in the legend. The observations revealed that the roundest slow rotating ETGs are among the most massive ones, while the high λ_{R_e} range is preferentially populated by less massive galaxies. Still today the formation of this objects is not completely clarified. A recent study by Moody et al. (2014) showed a possible formation channel through multiple minor mergers.

Comparing the panels in fig. 2.9 we find a similar trend for the high λ_{R_e} range to be preferentially populated by object with stellar masses below $10^{11.5} M_\odot$. The most massive galaxy in our sample represents an outlier in this regime. With decreasing λ_{R_e} the number density of ETGs with stellar masses above $10^{11} M_\odot$ increases, comparable to the observations. In the extremely round slow rotating sector we do not find the most massive galaxies, however we resemble the tendency for slow rotators to be more massive then fast rotators.

A possible reason for the lack of massive slow rotators in the simulated galaxy sample the still relatively small box size of our simulation, which simply does not allow the formation of extremely massive structures in a statistically relevant amount. This is also visible in the fact that the ATLAS[3D] sample includes five galaxies with stellar masses larger than $10^{12} M_\odot$, we only have one galaxy above this mass. Thus to understand the properties of those massive slow rotating galaxies, a larger box volume with at least the same resolution would be needed, however, this is beyond the scope of this work, but needs to be addressed in the future.
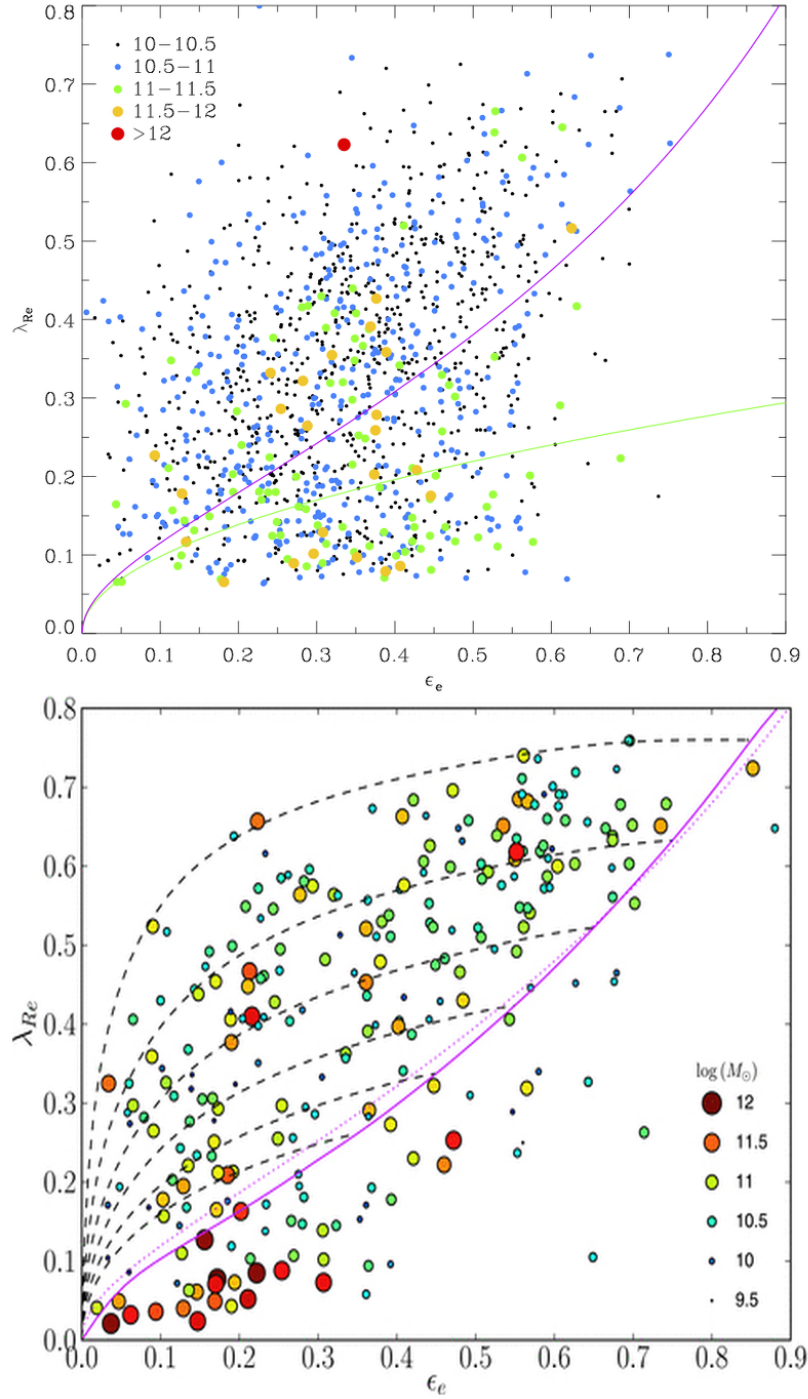
Figure 2.9.: Upper panel: λ_{R_e}-ϵ_e plane for the Magneticum sample. Colour and size of the symbols are according to the logarithm of the stellar galaxy mass as given in the legend. The green line represents eq. 2.5. Lower panel: Taken from Emsellem et al. (2011): Same as upper panel now for the ATLAS^{3D} sample. Lilac solid and dashed lines represent two different anisotropy parameters as in fig. 2.8.

2.5.3. Connecting the λ_{R_e}-ϵ_e and the M_*-J_* Plane

In this section we want to connect the separation of ETGs into slow and fast rotators to the fundamental classification introduced by Fall (1983) and reviewed in (Romanowsky and Fall, 2012). When investigating a plane spanned by the stellar specific angular momentum $\log_{10}(J_*)$ and the total stellar mass $\log_{10}(M_*)$, they found a continuous sequence of morphological types when going from the lower right to the upper left corner. Furthermore, they found that LTGs and ETGs follow a parallel sequence with a slope of approximately 2/3, implying a power law relation in the non-log plane. This result was confirmed for the Magneticum simulation, using the same box as this study, by Teklu et al. (2015). The authors adapt the so-called "b-value" defined as

$$b = \log_{10}\left(\frac{j_*}{\text{kpc km/s}}\right) - \frac{2}{3}\log_{10}\left(\frac{M_*}{M_\odot}\right) \tag{2.18}$$

to effectively distinguish between morphological galaxy types. It is per definition the y-intercept of a linear function with slope 2/3 in the $\log_{10}(M_*)$-$\log_{10}(J_*)$ plane. According to Romanowsky and Fall (2012) and Teklu et al. (2015), objects with $b \approx -4$ are disc-like galaxies followed by a smooth transition to lenticular and elliptical galaxies with decreasing b.

In fig. 2.10 we show the λ_{R_e}-ϵ_e plane coloured according to b-value bins of size $\Delta b = 0.25$. For the calculation of M_* and J_* we used all stellar particles within a sphere of radius $5R_e$ centred on the galaxy centre of mass.

There is a clear trend for the b-value to increase with increasing λ_{R_e}. Except for a few outliers, all objects with $b > -4.5$ are classified as fast rotators. The mean values for this branch is $(\overline{\lambda}_{R_e}, \overline{\epsilon}_e) = (0.46, 0.36)$, hence lying in the fast rotating regime. From a physical point of view one would expect objects with large b-values to be located in the extremely high λ_{R_e}, however inclination effects can lead to near zero values. This explains the scatter in λ_{R_e} for galaxies with $b > -4.5$. For the high λ_{R_e} galaxies in our sample we see properties similar to LTGs in terms of b-value. Such a connection was already found by Bois et al. (2011) and Jesseit et al. (2009) when they compared the location of their spiral merger progenitors in the λ_{R_e}-ϵ_e plane to ATLAS[3D] or SAURON observations. The formation process of these objects is probably driven by smooth processes like strangulation or ram-pressure-stripping of an gas rich disc virtually conserving its b-value. Conserving the b-value requires a coevolution of M_* and J_* during the galaxy transformation. In the view of the Hubble-sequence they are most probably classified as SO, which typically possess a large amount of angular momentum. Although Querejeta et al. (2015) showed that the formation of S0 through the violent process of major merger is possible, they did not reach the high λ_{R_e} regime above 0.65. This is a hint for a transition of smooth formation processes, only present in cosmological simulations, to more violent ones when going from extreme high to intermediate λ_{R_e}. This supports our findings in sec. 2.5.2.

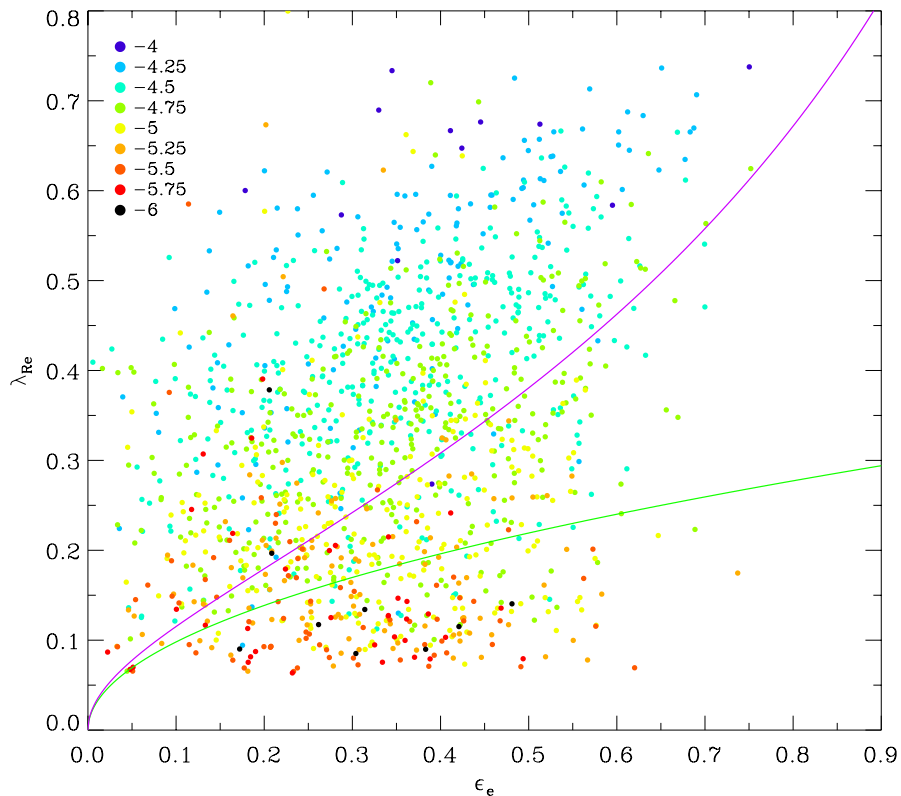Objects with $b < -5.25$ are primarily classified as slow rotators, reflecting their

Figure 2.10.: $\lambda_{\mathrm{R_e}}$-ϵ_e plane for the Magneticum sample with colours according to nine
b-value bins of size 0.25 symmetric around the value given in the legend.

small total angular momentum. Accordingly, the mean values for this branch are
$(\overline{\lambda}_\mathrm{R}, \overline{\epsilon}_\mathrm{e}) = (0.14, 0.27)$, thus lying in the slow rotating region. The intermediate
b-values populate the complete intermediate $\lambda_{\mathrm{R_e}}$ range with a mean of $(\overline{\lambda}_\mathrm{R}, \overline{\epsilon}_\mathrm{e}) =$
$(0.31, 0.34)$.

Although we find a smooth transition for the b-values, we want to emphasise that
there are outliers in all $\lambda_{\mathrm{R_e}}$ regions, e.g. one of the galaxy with the lowest b-value
possesses a $\lambda_{\mathrm{R_e}}$ of 0.38. An ongoing merger might be an explanation for such an
unlikely object.

To further investigate the connection between $\lambda_{\mathrm{R_e}}$ and b, fig. 2.11 shows their
direct relation. The vertical dashed lines mark the borders of the b-bins, while
colours are according to fig. 2.10. Although fig. 2.11 nicely verifies the trend
described above, the b-value range for a constant $\lambda_{\mathrm{R_e}}$ is too broad to conclude a
distinct correlation. We can only define a banana shaped envelope enclosing the
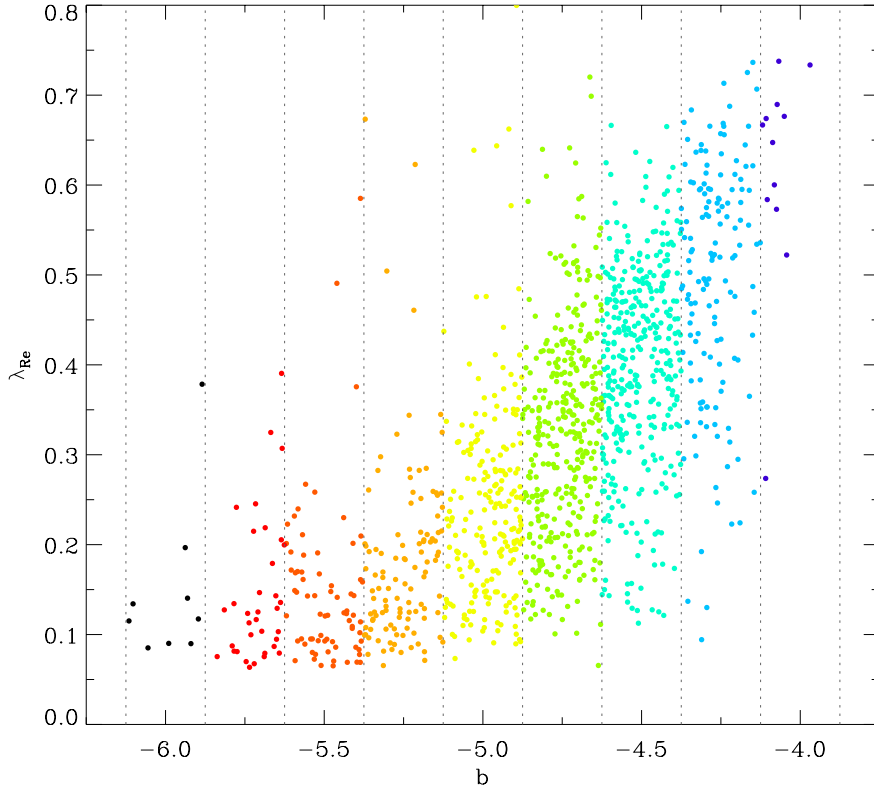vast majority of galaxies.

Figure 2.11.: Relation between $\lambda_{\mathrm{R_e}}$ and b-value. Colours correspond to the same nine bins as in fig. 2.10 with vertical lines marking the bin borders.

2.5.4. Connecting Morphological and Kinematical Classification

In eq. 1.1 we introduced the Sérsic index as a parameter to distinguish between ETGs and LTGs, more generally between spheroidal and disc-like objects. Although it was already established in 1963, it is still widely used in observational studies (Sérsic, 1963). Since it describes the curvature of the Sérsic-profile fitted to the radial light distribution, it is a purely morphological parameter. Thus, in this section we explore how this morphological classification is connects to the kinematical split-up of slow and fast rotators. Furthermore, the relationship between the Sérsic index and the b-value is investigated.

Sérsic fits

The Sérsic fits are performed on the same projection of the stellar component used to calculate $\lambda_{\mathrm{R_e}}$, but out to $5R_{\mathrm{e}}$. Since the isophotes in general have an elliptical shape, we initially transform them into circles, conserving the enclosed area, by

applying the coordinate transformation:

$$x' = x \cdot \sqrt{1 - \epsilon_{\mathrm{e}}}$$
$$y' = \frac{y}{\sqrt{1 - \epsilon_{\mathrm{e}}}} \quad (2.19)$$

where x is measured along the major axis of the ellipse. We neglect the effects of isophotal twists or variation of ϵ_{e} with radius. Excluding the inner 1.4 kpc, the density is derived in annuli out to $5R_{\mathrm{e}}$. The border of the annuli are determined by demanding a constant particle number of 200, ensuring a proper weighting of all data points.

The surface density is then defined as:

$$\rho(R) = \frac{M(R_{\mathrm{in}} < R < R_{\mathrm{out}})}{\pi R^2} \quad (2.20)$$

where R_{in} and R_{out} are the boundaries of the annuli. We now fit a Sérsic-profile in log-space to the obtained surface density $\rho(r)$:

$$\log_{10}(\rho(R)) = \log_{10}(I_{\mathrm{e}}) - b_n \left[\left(\frac{R}{R_{\mathrm{e}}} \right)^{\frac{1}{n}} - 1 \right] \log_{10}(e) \quad (2.21)$$

where I_{e} is the density at the effective radius R_{e}. The dimensionless parameter b_n is defined according to the definition of the effective radius. There is no analytic solution to the defining equation for b_{n}. Hence, we use a numeric approximation given by Ciotti and Bertin (1999):

$$b_n = 2n - \frac{1}{3} + \frac{4}{405n} + \frac{46}{25515n^2} \quad (2.22)$$

Fig. 2.12 shows fit examples for four galaxies. As expected, n is lower for more flat profiles. A LTG with $n = 1$ would be represented by a straight line in this log-linear plot.
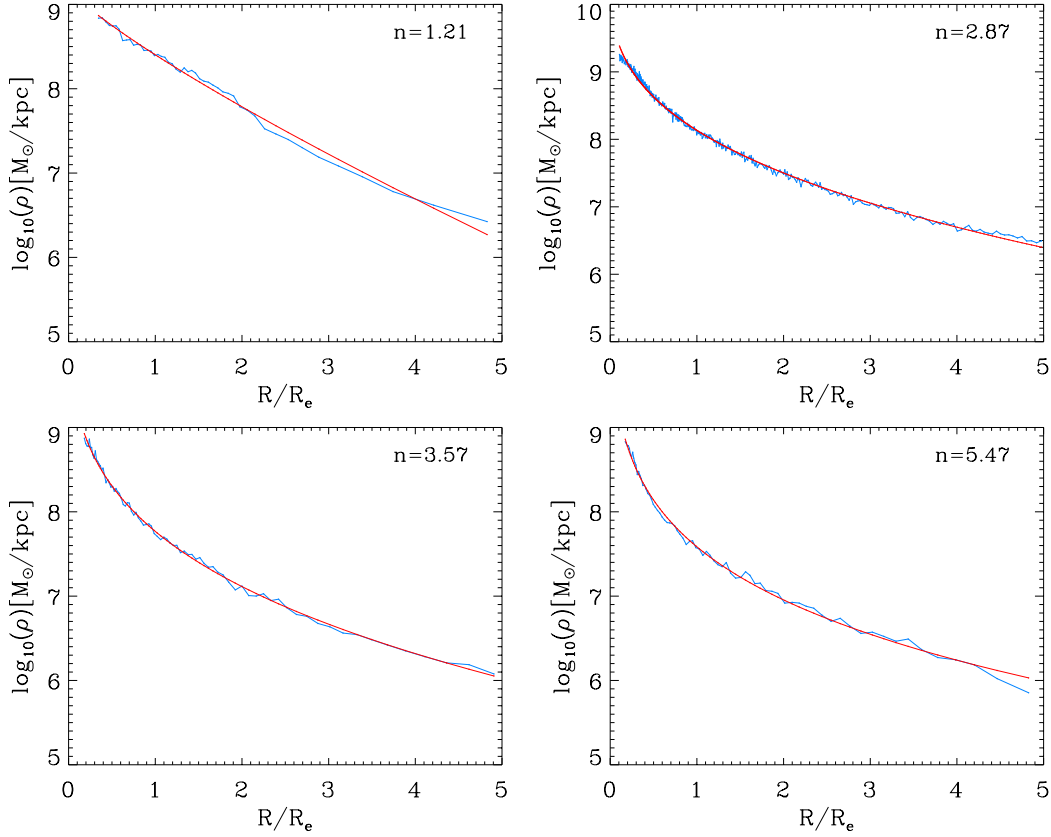
Figure 2.12.: Projected surface density profiles for four example galaxies with different Sérsic indices indicated by blue lines in a log-linear plot. Red curves represent the best fitting Sérsic profile.

Sérsic Index in the λ_{R_e}-ϵ_e Plane

Fig. 2.13 illustrates the Sérsic index distribution in the λ_{R_e}-ϵ_e plane for the Magneticum (upper panel) and the ATLAS[3D] (lower panel) sample (Krajnović et al., 2013). We sample the galaxies into seven bins as defined in the legend of fig. 2.13, where big symbols represent the mean $(\overline{\lambda}_R, \overline{\epsilon}_e)$ of the corresponding bin.

The statistical abundance for the Sérsic index bins are summarised in tab. 2.3. The Magneticum sample covers the complete range found for the ATLAS[3D] sample. In the six lowermost bins the deviations are small, namely between 0.4 and 3.4 per cent. For both samples the majority of galaxies populate the bin with $2 < n < 3$. We find the largest deviation in the uppermost bin. However, overall the statistical distributions are in good agreement, allowing for a meaningful comparison.
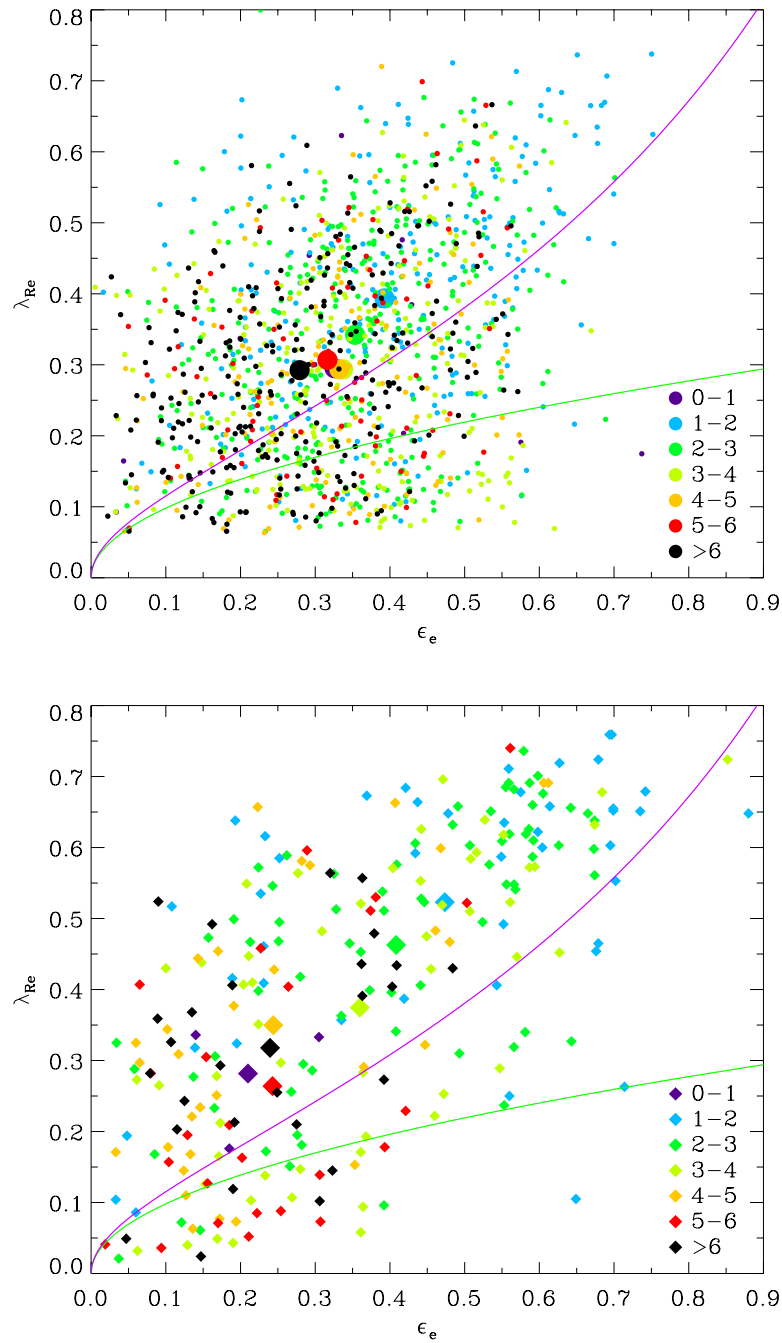
Figure 2.13.: Upper panel: λ_{R_e}-ϵ_e plane for the Magneticum sample with colours according to the Sérsic index bins defined in the legend. Major symbols indicate the mean values for each particular bin. Lower Panel: Same as upper panel for the ATLAS^{3D} sample.

Looking at the overall distribution of n in fig. 2.13 there is no clear separation in both samples. However, the high λ_{R_e} regime is preferentially occupied by galaxies

with $1 < n < 3$ in both panels.

For the Magneticum sample four bins show almost the same $(\overline{\lambda}_{R_e}, \overline{\epsilon}_e)$, while only the $1 < n < 2$ and $3 < n < 4$ bins shift to higher mean values as physically expected. Such a trend is also present in the observational sample, but more distinct: except for the first and last bin, larger n tend to exhibit larger $(\overline{\lambda}_{R_e}, \overline{\epsilon}_e)$. Although we observe weak trends for both samples, the mean values of all bins are in the intermediate range.

Table 2.3.: Statistical frequency of different Sérsic index bins.

Sérsic index	Magneticum [%]	ATLAS^{3D} [%]
$0 - 1$	0.8	1.2
$1 - 2$	19.3	17.3
$2 - 3$	25.9	29.2
$3 - 4$	17.6	20.4
$4 - 5$	10.0	11.9
$5 - 6$	6.1	9.6
> 6	19.7	10.3

The direct relationship between n, λ_{R_e} and ϵ_e is shown in fig. 2.14. Colours are according to the various bins as indicated in the legend of 2.13.

It confirms the trend stated above, furthermore showing a rather well-defined upper envelope in all panels. Especially, the maximum ϵ_e in each bin for the Magneticum sample follows a parabolic shape. A similar trend is present in the ATLAS^{3D} sample, however showing a more linear declining shape when going to larger n. In the two left panels we see a similar linearly declining behaviour, but less evident. For the observational sample this was already found in Krajnović et al. (2013).

In general, we do not find any strong correlation between ϵ_e and n or λ_{R_e} and n for the Magneticum sample. Hence, using the Sérsic index alone is not sufficient to disentangle fast and slow rotators. A similar result was concluded by Emsellem et al. (2011) from the correlation between a_4 and λ_{R_e}, where a_4 is a purely morphological parameter measuring the "boxiness" and "disciness" of galactic isohotes (Kormendy and Bender, 1996; Bender, 1987).
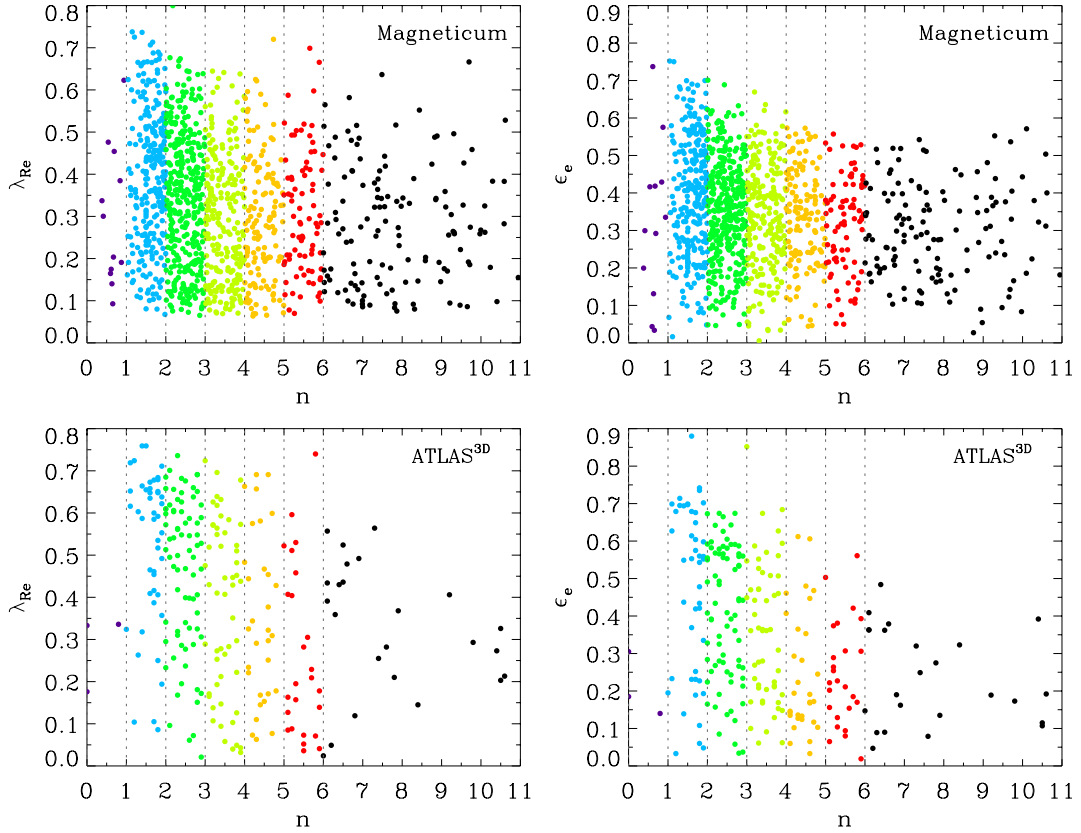
Figure 2.14.: Upper Row: Correlation between Sérsic index and λ_{R_e} (left) and ellipticity
(right) for the Magneticum sample. Lower Row: Same as upper row but
for the ATLAS[3D] galaxies. In all panels the colours correspond to the
Sérsic index bins as in fig. 2.13 with vertical dashes lines indicating the
borders.

Correlation Between Sérsic Index and b-value

After investigating the classifications according to the λ_{R_e}-ϵ_e plane in the view of
the Sérsic index, we now inspect the connection between n and the b-value (see
sec. 2.5.3). To this end fig. 2.15 shows the direct relationship between n and the
b-value. Since b-values are not available for ATLAS[3D] galaxies we are restricted to
the simulated sample. The colours are again chosen like in fig. 2.13.

The distribution is almost featureless, showing a fairly weak tendency for larger n
to have lower b-values, however much to weak for a meaningful correlation. Again,
the kinematical classification according to b is inconsistent with the morphological
classification. In the view of the results of sec. 2.5.4 this comes up to our expecta-
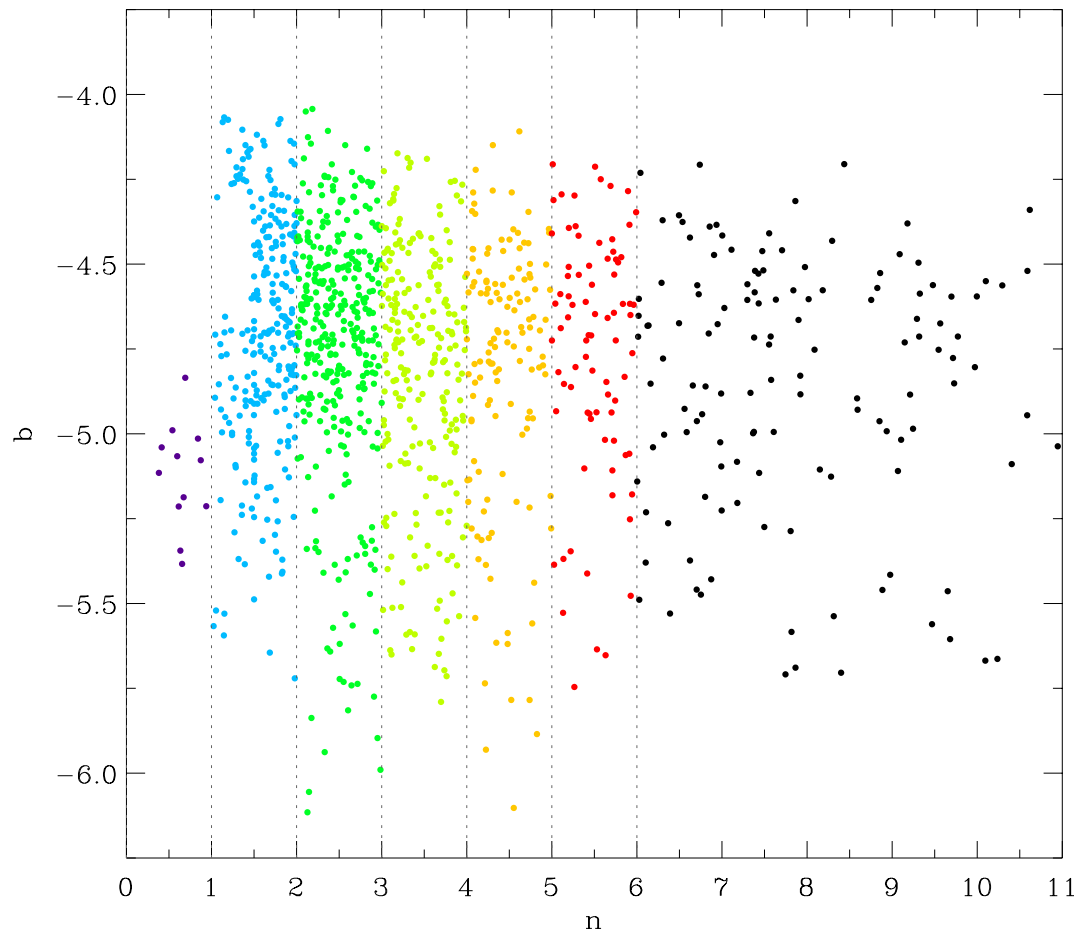tions, since both λ_{R_e} and b are proxies for the angular momentum.

Figure 2.15.: Sérsic index vs. *b*-value with colours and dashed lines according to Sérsic bins as in the figures before.

3. Kinematical Misalignment and Implications on Shape

3.1. Quantifying Morphological and Kinematical Orientation

After investigating the central kinematics of our sample in the previous sections we now analyse an important large scale property. The misalignment between morphology and kinematics gives meaningful insight into the intrinsic structure of a galaxy. For this purpose it is required to introduce quantities to measure the morphological and kinematical orientation of a galaxy.

Since the dynamics of a galaxy is dominated by its angular momentum we use the total angular momentum vector

$$\mathbf{J} = \sum_{j=1}^{N_\mathrm{s}} m_j \mathbf{r_j} \times \mathbf{v_j} = \sum_{j=1}^{N_\mathrm{s}} m_j \begin{pmatrix} y_j v_{z,j} - z_j v_{y,j} \\ z_j v_{x,j} - x_j v_{z,j} \\ x_j v_{y,j} - y_j v_{x,j} \end{pmatrix} \tag{3.1}$$

to measure the kinematical orientation of an object, where the sum runs over all stellar particles within the considered region.

The definition of the morphological orientation is based on fundamental properties of the moments of inertia tensor for ellipsoids: For an elliptical mass distribution the principal axes of inertia are along the semi-minor, semi-median and semi-major axis of the object. They can be obtained by diagonalising the moments of inertia tensor for the stellar particle distribution:

$$\hat{\mathbf{I}} = \sum_{j=1}^{N_\mathrm{s}} m_i \begin{pmatrix} y_j^2 + z_j^2 & -x_j y_j & -x_j z_j \\ -y_j x_j & x_j^2 + z_j^2 & -y_j z_j \\ -z_j x_j & -z_j y_j & x_j^2 + y_j^2 \end{pmatrix} \tag{3.2}$$

This procedure provides the principle axis of the maximum and minimum principle moments of inertia and a perpendicular axis, which in the case of an elliptical object corresponds to the semi-principal axes.

Interpreting these vectors depends on the particular shape of the ellipsoid. Let us consider an ellipsoid with semi-principal axes of length a,b and c measured along the x,y and z axis, respectively. Furthermore, the ellipsoid is centred on the origin of the coordinate system. Such an object can have four distinct shapes, each fulfilling

the defining relation for an ellipsoid:

$$\frac{x_{\text{ell}}^2}{a^2} + \frac{y_{\text{ell}}^2}{b^2} + \frac{z_{\text{ell}}^2}{c^2} \leq 1 \tag{3.3}$$

- $a > b > c$ – **triaxial** shape

- $a = b > c$ – **oblate** shape

- $a = b < c$ – **prolate** shape

- $a = b = c$ – degenerate case of a **sphere**

For an oblate object the principal axes of inertia of the largest moment is along the z-axis, with the other two moments being equal. In the case of a prolate body there are two equal moments along the x and y axis, and one smaller along the z-axis. In contrast, a triaxial object has three different moments of inertia, with the largest along the z-, the medium along the y- and the smallest along the x-axis.

Certainly the appearance of a real elliptical galaxy is not completely ellipsoidal. In addition massive substructures can influence the considerations above. However for most elliptical galaxies our consideration represents a reasonable approximation. To support this assumption, fig. 3.1 shows the stellar particle distribution before (left panel) and after (right panel) rotating the coordinate system such that the principle axis with the largest moment of inertia is along the z-axis. One can see that after the rotation the z-axis corresponds to the minor axis of the galaxy, hence implying an oblate galaxy shape in agreement with the notion described above. Based on our considerations we quantify the morphological orientation of a galaxy by the three principal axes of inertia.
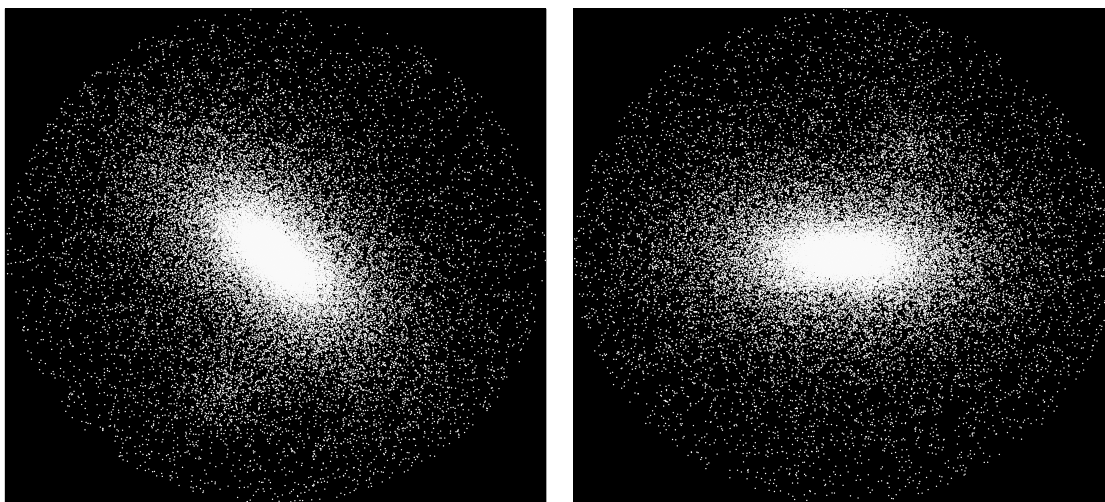

Figure 3.1.: Stellar particle distribution before (left panel) and after (right panel) rotating to the principle axes of inertia system.

3.2. Misalignment Angle Distribution in the Magneticum Sample

To measure the misalignment of the morphology and kinematics of a galaxy we follow the definition of Franx et al. (1991) and calculate three misalignment angles Ψ_i given by the equation

$$\sin(\Psi_i) = |\sin(\Phi_i)| \tag{3.4}$$

where Φ_i is the angle between the i'th principal axes of inertia and the total angular momentum as defined in the previous section. In the above parametrisation Ψ_i lies between $0°$ and $90°$ and is not sensitive to changes of $180°$ in Φ_i.

3.2.1. Fast and Slow Rotator

The result for the misalignment angle is shown in fig. 3.2 as histograms, showing the complete sample (upper panel), fast (central panel) and slow rotators (lower panel). We consider all stellar particles within a sphere of radius $5R_e$. We find that 44 per cent of the Magneticum sample galaxies show a misalignment angle lower than $5°$ with the major moment of inertia, Ψ_3. Another 21 per cent of the galaxies are in the range $5° < \Psi_3 < 10°$, while in total 74 per cent populate the region with $\Psi_3 \leq 15°$. These objects are most probable axis-symmetric and oblate shaped with minor axis rotation. Theoretically, a prolate galaxy rotating around one of the minor axes would show the same behaviour, however, such objects are very unlikely.

The peaks at $90°$ in the other two panels are a direct consequence of the small misalignment in the third panel, because per definition the principle axis of inertia are perpendicular. It is however meaningful to also investigate these angles, since a prolate objects with major axis rotation would be aligned with the minor moment and hence generate a peak in the first or second panel at $0°$. As can be seen, there are only very few galaxies which show a peak at $\approx 0°$ in the first or second panel, that is these objects are rare.

While the total mean value for Ψ_3 is 13.9, only 25 per cent of the galaxies show a misalignment angle larger than $15°$ with only a few percentages having angles above $40°$. As a result for the majority of galaxies in our sample the total angular momentum is aligned with the principal axes of inertia of the largest moment. Croft et al. (2009) calculated the same angle in a fully cosmological simulation at a redshift of 1. They found a significantly larger value of $39°$ for their average sample. This disagreement implies a significant evolution of the misalignment angle from $z = 1$ to $z = 0$. A possible explanation might be the higher merger rate at $z = 1$ compared to $z = 0$, which leads to a larger amount of galaxies with external interactions, disturbing the alignment. Recent studies indeed showed a decreasing merger rate over cosmic time, however strongly dependent on the progenitor mass ratios (Rodriguez-Gomez et al., 2015; Lotz et al., 2011). Hence we can not clarify if the evolution in the merger rate can account for the approximately factor 3 larger misalignment angle at $z = 1$, without checking the detailed merger trees in the simulation.
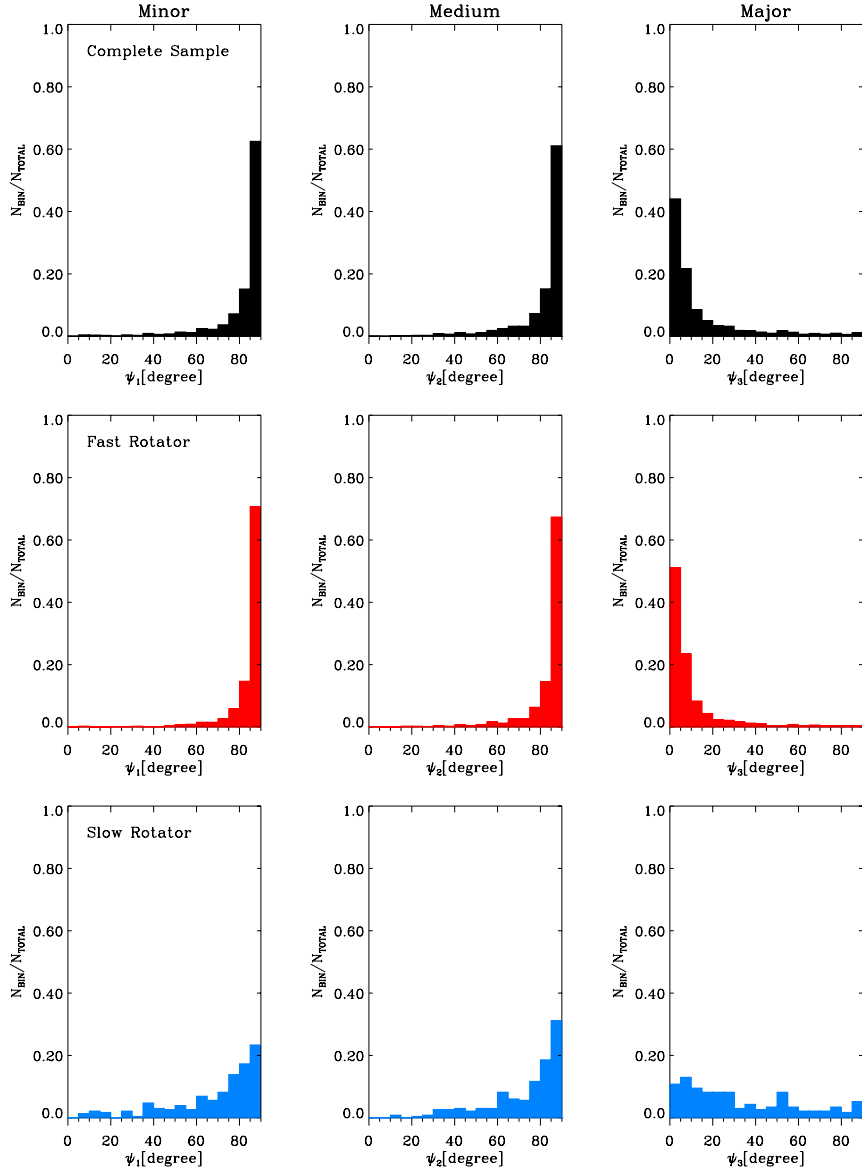
Figure 3.2.: Misalignment angle for minor, medium and major moment of inertia (from left to right). Different rows correspond to the complete Magneticum sample (black), fast rotators (red) and slow rotators (blue). We only take particles within $5R_{\rm e}$ into account.

If we compare the lower two panels, a clear trend is visible: Fast rotators are much better aligned with the major moment of inertia than slow rotators. The mean value of Ψ_3 is 10.0° for the fast rotating regime. This implies, as expected, an oblate disc-like shape with minor axis rotation for fast rotators. In contrast, the distribution for slow rotators is much broader, showing only a weak trend of alignment between the morphological major axis and the angular momentum axis,

with an average misalignment of $\overline{\Psi}_3 = 32.6°$. This is not a surprise result since slow rotators are per definition dominated by random motion, it however indicates an agreement between the kinematics on the scale of $1R_e$ and the complete galaxy out to $5R_e$ for both fast and slow rotators.

To further investigate the misalignment angle, fig. 3.3 illustrates the same plot as fig. 3.2 only considering stellar particles within $2.5R_e$.
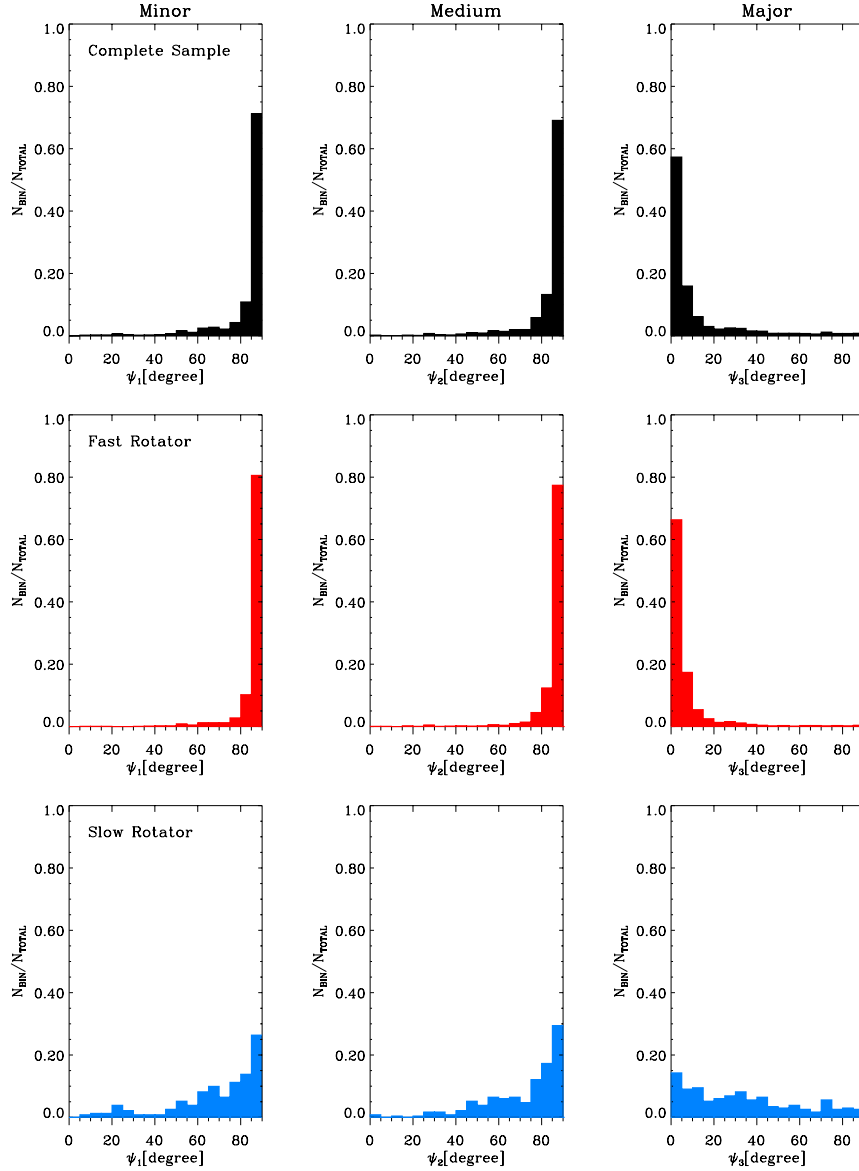

Figure 3.3.: Same as fig. 3.2, but considering only stellar particles within $2.5R_e$

Visually we observe an improved alignment for the complete sample and the fast rotators. Also, the slow rotators appear to be better aligned, however, the mean Ψ_3 stays almost identical with $\overline{\Psi}_3 = 33.1°$.

Table 3.1.: Statistical properties of the misalignment angle distribution.

$5R_e$	Complete sample	Fast Rotators	Slow Rotators
$\Psi_3 < 5°$:	44%	52%	11%
$5° < \Psi_3 < 10°$:	22%	24%	13%
$\Psi_3 < 15°$:	74%	83%	33%
$\Psi_3 > 15°$:	26%	17%	66%
$\overline{\Psi}_3$:	13.9°	10.0°	32.6°
$2.5R_e$			
$\Psi_3 < 5°$:	57%	66%	14%
$5° < \Psi_3 < 10°$:	16%	17%	9%
$\Psi_3 < 15°$:	80%	89%	33%
$\Psi_3 > 15°$:	20%	11%	67%
$\overline{\Psi}_3$:	11.8°	7.3°	33.1°
$1R_e$			
$\Psi_3 < 5°$:	60%	70%	15%
$5° < \Psi_3 < 10°$:	15%	16%	11%
$\Psi_3 < 15°$:	80%	90%	34%
$\Psi_3 > 15°$:	20%	10%	66%
$\overline{\Psi}_3$:	11.7°	7.0°	35.5°

The mean value for the complete sample decreases slightly to $\overline{\Psi}_3 = 11.8°$ with a total of 80 per cent having misalignment angles lower than $15°$. For the fast rotators this trend is somewhat more evident with a decline of $\overline{\Psi}_3$ to $7.3°$. On the even smaller scale of $1R_e$ this behaviour continues, though not as clear. Going from $2.5R_e$ to $1R_e$ the mean values and percentages only chance little as can be seen in tab. 3.1, where we summarise the results for all scales. This might be due to structures like bulges, rings and bars which potentially disturb the alignment, which become more influential in this region.

We can directly compare the complete sample in fig. 3.3 to the observed angles found in Krajnović et al. (2011) for the ATLAS[3D] sample. They approximated the misalignment angle via the two dimensional velocity and intensity maps in the range between 2.5 and $3R_e$, depending on the accessible data for the galaxy.

They find a mean misalignment angle of only $3°$ with 90 per cent showing angles lower than $15°$. This is a significant difference of $8.8°$ and 10 per cent respectively. We however want to emphasis the fact that the differences in the methods determining Ψ influences the comparison and therefore it is reasonable to compare the overall

picture rather than the numbers: In agreement with the observations we find the majority of ETGs to show strong evidence of axial symmetry with the total angular momentum being aligned with the minor axis (major moment of inertia).

3.2.2. Correlating the Misalignment Angle with the M_*-J_* Plane

In sec. 2.5.3 we introduced the b-value as a parameter to discriminate spheroidal and disclike galaxies according to their position in the M_*-J_* plane. We now want to explore how the b-value connects to the misalignment angle to see if it fits the physical expectation for larger b-values to be better aligned. Since the b-value is a globally measured quantity, the misalignment angles on the scale of $5R_\mathrm{e}$ are employed in this section.

Fig. 3.4 shows again the misalignment angle distribution as an histogram plot, each row now representing one of five b-value bins. Corresponding mean values and percentage are displayed in 3.2, revealing a distinct tendency for larger b-values to be better aligned.

The percentage in the range $0° < \Psi_3 < 5°$ declines continuously from 84 per cent in the first bin to 0 per cent in the last bin. Accordingly, the mean misalignment angle increases rapidly with decreasing b. Only between $5°$ and $10°$ the amount of galaxies rises between the first and second bin.

Table 3.2.: Statistical properties of the misalignment angle distribution for various b-value bins. The bins are as given in fig. 3.4.

	1.Bin	2.Bin	3.Bin	4.Bin	5.Bin
$\Psi_3 < 5°$:	84%	56%	14%	1%	0%
$5° < \Psi_3 < 10°$:	11%	27%	21%	4%	0%
$\Psi_3 < 15°$:	99%	90%	50%	12%	0%
$\Psi_3 > 15°$:	1%	10%	50%	88%	100%
$\overline{\Psi}_3$:	3.7°	7.3°	22.4°	45.7°	54.0°

This result follows our expectations since larger b-values correspond to disclike objects. In the view of sec. 2.5.4, were we found only a weak correlation between the Sérsic index and b, this is a surprising result. It suggest that also galaxies with large Sérsic indices can be well aligned implying again a non-trivial connection between kinematics and the Sérsic index.
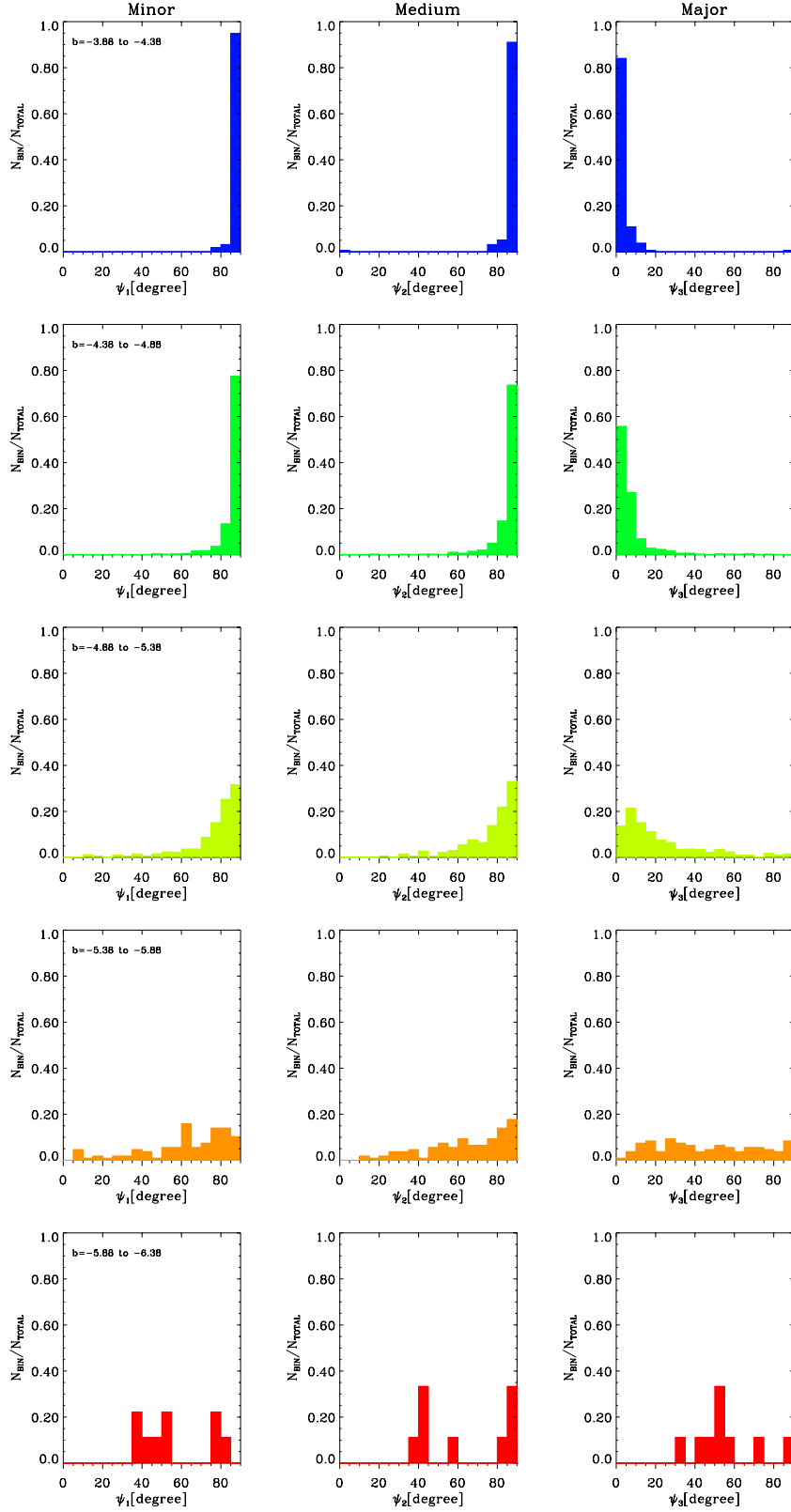
Figure 3.4.: Misalignment angle for minor, medium and major moment of inertia (from left to right). Each row represents a b-value bin as given in the first panel. We consider only stellar particles within $5R_\mathrm{e}$.

3.3. Discriminate Between Oblate and Prolate Shape

As shown in the previous sections, if one assumes an ellipsoidal morphology the moments of inertia deliver insight into the actual shape of the galaxy, i.e. prolate,oblate or triaxial. In this section we introduce a parameter to effectively distinguish between prolate and oblate objects. Moreover, its correlation to the b-value is investigated.

As mentioned in sec. 3.1, an oblate ellipsoid has two equal moments of inertia and a larger one. In contrast, a prolate body possesses two equal and one smaller moment. In the special case of a sphere all moments are equal. Bases on this consideration we define the so-called "oblatness" parameter n_{ob} as:

$$n_{\mathrm{ob}} = \frac{(J_1/J_2)}{(J_2/J_3)} \tag{3.5}$$

where J_1, J_2 and J_3 are the minor, medium and major moment of inertia, respectively. Following this definition it is possible to distinguish the three shapes:

$$n_{\mathrm{ob}} \begin{cases} > 1 & \text{oblate,} \\ \approx 1 & \text{nearly spherical,} \\ < 1 & \text{prolate.} \end{cases} \tag{3.6}$$

Since triaxial shaped ellipsoids show three different moments, with their quotient dependent on the length of the principle axes, n_{ob} does not separate them from oblate and prolate galaxies. It is important to note that $n_{\mathrm{ob}} > 1$ does only imply a more oblate shape, rather than a completely oblate morphology. The same applies in the prolate case.

Fig. 3.5 illustrates the relation between n_{ob} and the b-value. It clearly indicates a trend for larger b-values to be oblate shaped, whereas lower b-values tend to be more prolate. When looking at the mean values the transition between oblate and prolate occurs at $b \approx -5.1$. We find that 73 per cent of the galaxies are in the oblate range with $n_{\mathrm{ob}} > 1$. Accordingly, 27 per cent populate the prolate range with $n_{\mathrm{ob}} < 1$. These values are almost identical to the percentages we found in sec. 3.2.1 on the $5R_{\mathrm{e}}$ scale for galaxies with a misalignment angle below and above $15°$.

In fig. 3.6 we again show the b-value against n_{ob}, now discriminating the two branches of misalignment angles by colour. Although the separation is not as distinct as the percentages suggest, a clear trend is visible: Galaxies with $\Psi_3 < 15°$ preferentially populate the oblate regime with a mean n_{ob} of 1.16. This supports the conclusion that galaxies with little misalignment show an oblate shape with minor axis rotation.

In contrast, the red symbols are present in both branches, however not reaching the range $n_{\mathrm{ob}} > 1.4$. They reach farther into the prolate region, accordingly the mean value is 0.92, hence in the spherical/prolate regime. Of course effects which disturb the ellipsoidal morphology, like tidal forces or ongoing mergers, are more
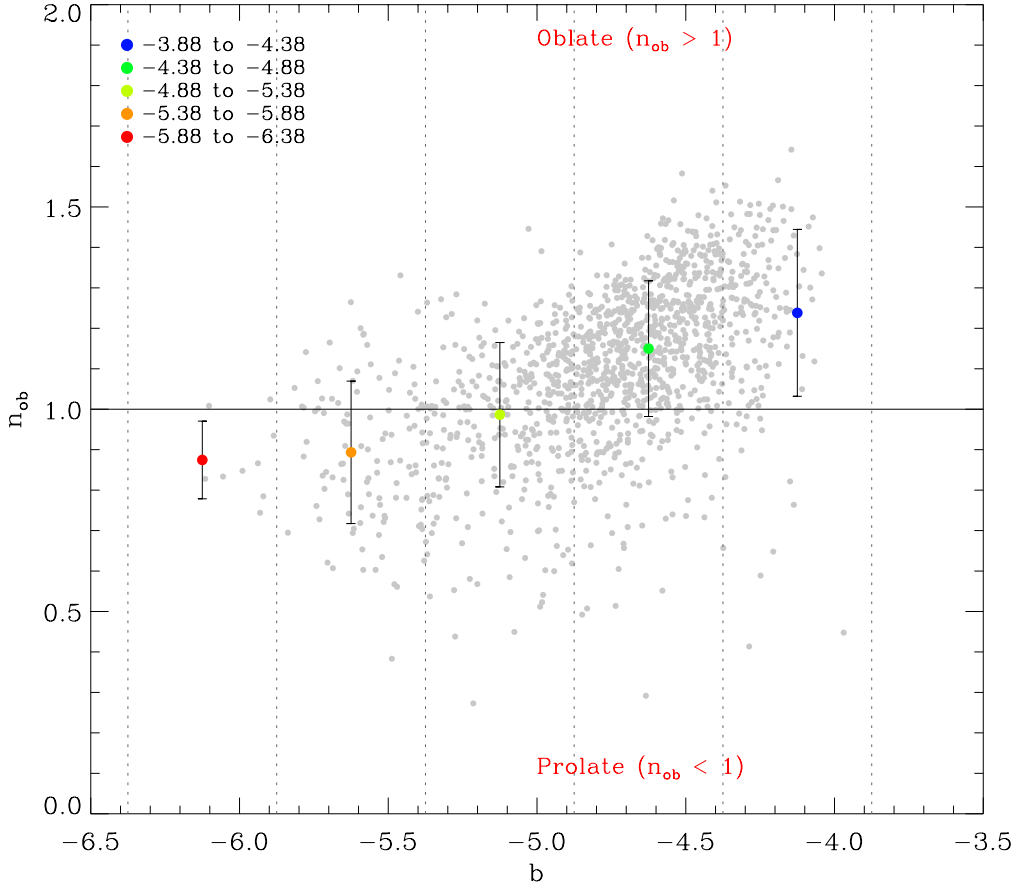
present for misaligned galaxies.

Figure 3.5.: b-value against the oblateness parameter n_{ob}. We adapt the same bins as in fig. 3.4. Grey circles represent the complete distribution, whereas coloured circles indicate the mean value per bin. Black dashed lines mark the borders of each bin. The length of the error bars is according to the standard deviation within each bin. The horizontal solid line separates the prolate (< 1) and the oblate (> 1) regime.

Furthermore, triaxial galaxies have a larger potential to exhibit features like kinematical and morphological twists increasing the misalignment (van den Bosch and van de Ven, 2009). Therefore both effects influence the the $\Psi_3 > 15°$ regime and increase the scatter into the oblate and prolate region.
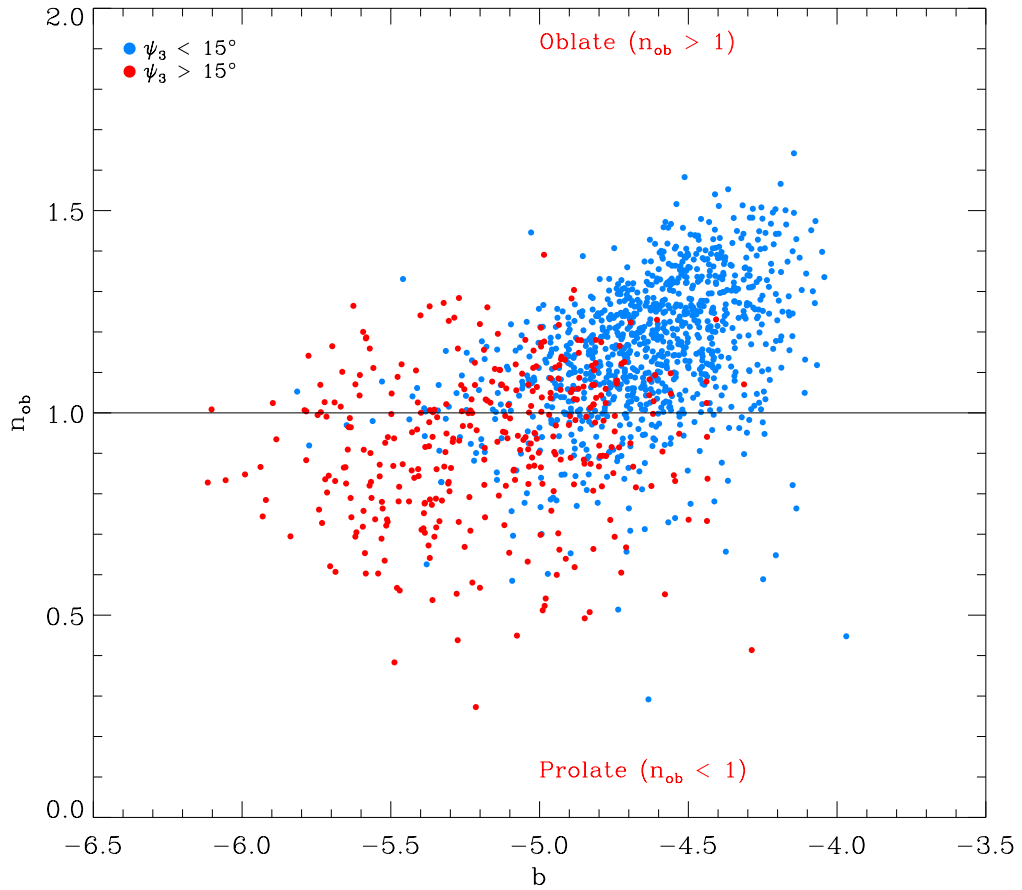
Figure 3.6.: b-value against the oblateness parameter n_{ob}. Red filled circles indicate galaxies with $\Psi_3 > 15°$, whereas blue symbols correspond to objects with $\Psi_3 < 15°$.

4. Kinematical Features

4.1. Kinematical Features in the $\mathrm{ATLAS^{3D}}$ Sample

As mentioned in sec. 2.2, the $\mathrm{ATLAS^{3D}}$ project provides detailed kinematical maps of the stellar velocity and velocity dispersion. Until now, we only used these maps to calculate λ_{R_e} without viewing them in detail.

Within the $\mathrm{ATLAS^{3D}}$ project, such a study was done by Krajnović et al. (2011) and will serve as the comparison observation in this section. They find that the majority of galaxies are dominated by ordered rotation, but several maps exhibit distinct features. The variety of kinematical features indicate a variety of formation histories. Based on this result they define five kinematic subclasses:

- **Group a:** galaxies with no apparent rotation.

- **Group b:** galaxies with non-regular velocity pattern (non-regular rotators), but without any specific kinematic feature.

- **Group c:** galaxies with kinematically distinct or counter-rotating cores.

- **Group d:** galaxies with two symmetrical off-centred stellar velocity dispersion peaks.

- **Group e:** galaxies with regular apparent rotation (regular rotators) and with or without small minor-axis kinematic twists.

Members of group a to d are mainly slow rotators, whereas group e contains mostly fast rotators. While the groups a,b,c and e are defined by their velocity maps, group d is determined by the appearance of the dispersion maps.

Examples for observed velocity maps for all groups are given in fig. 4.1. The panels showing galaxies of group e suggest a further distinction, however the large scale behaviour is similar in all three maps.

Especially kinematical decoupled cores are believed to be imprints of the complex assembly history of early type galaxies. Several studies investigated the connection of these five kinematical groups to the formation processes affecting the galaxy evolution. Tsatsi et al. (2015) showed that kinematical maps of type c and d can result from an initially prograde major merger of two disk galaxies. The kinematically distinct core is most prominent in the old stellar population. Further studies demonstrate the formation of the other three groups by major or multiple minor mergers (Moody et al., 2014; Bois et al., 2010, 2011; Naab et al., 2014; Jesseit et al., 2009; Khochfar et al., 2011).
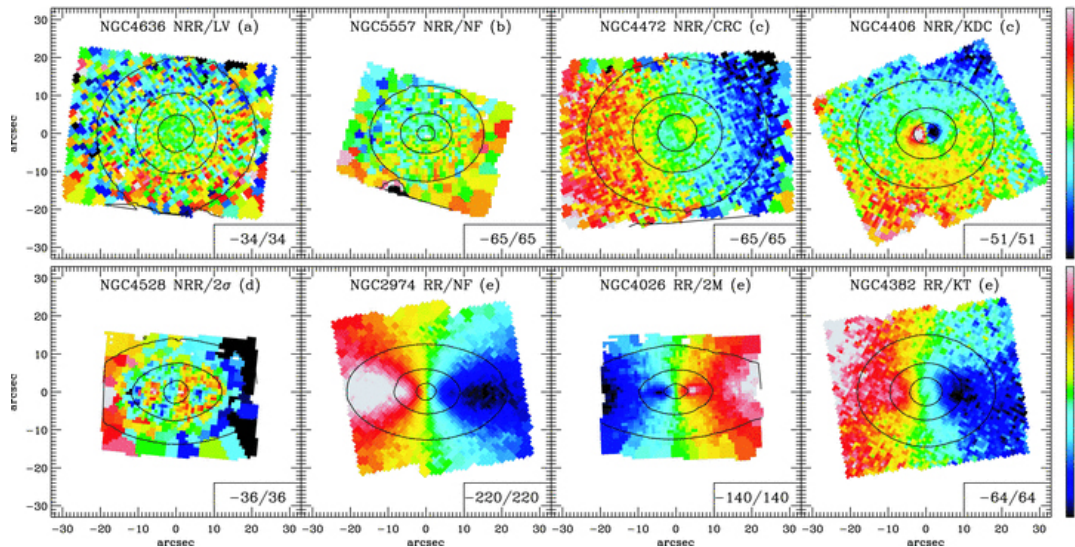
Figure 4.1.: Taken from Krajnović et al. (2011): Example of various features found in the velocity maps of ATLAS^{3D} galaxies. The different kinematical groups are indicated by the letter in the right upper corner.

4.2. Kinematical Features in the Magneticum Sample

In this section we investigate whether we find galaxies showing the same kinematical features as the five groups stated above. Therefore, we construct images of the voronoi tessellated velocity and dispersion fields out to one and two effective radii. After choosing a random projection of the galaxy and rotate it such that the projected major axis is aligned with the x-axis the CVT is performed. We lower the target-particle-number to $N_T = 100$ to obtain an improved spatial resolution. The characteristic kinematical features are identified by eye viewing the velocity maps on both scales.

Group a

Group a combines all galaxies possessing featureless non-rotating velocity maps with typical low-level velocities. Results from binary mergers simulations suggest a complex formation history since they could not be formed in a such process (Bois et al., 2011). The velocity maps found in the magneticum sample in fig. 4.2 show no evidence of a characteristic kinematical feature in agreement with the observations.

Furthermore, the maximum velocities are around 30 to 50km/s, which indicate the low-level velocities. So we can clearly account for this types of velocity structures.
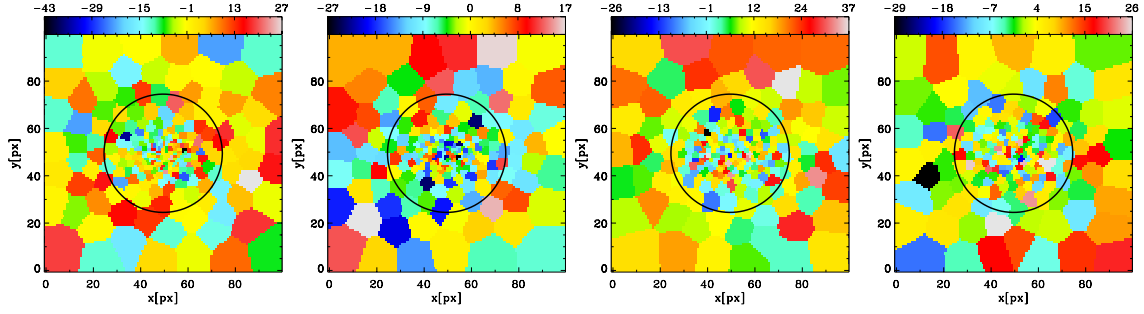
Figure 4.2.: Voronoi binned velocity maps of four members of group a for the simulated galaxies. The colours are rescaled for every individual plot as given in the colour bar in km/s. Black solid circles indicate one effective radius.

Group b

Although denoted as non-regular rotators, galaxies assigned to this group show complex velocity patterns without any specific feature. Hence a large variety of velocity maps are collected in this group. For example, galaxies with multiple rotating sub-components or significant kinematical twists are contained. Therefore, it is kind of a residual class of objects which could not be assigned to group c or e. We also plot four examples identified in the Magneticum sample in fig. 4.3.
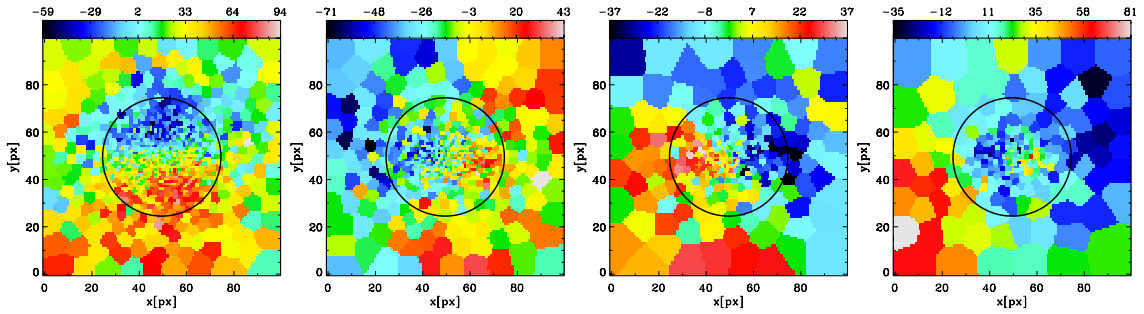

Figure 4.3.: Voronoi binned velocity maps of four members of group b for the simulated galaxies. The colours are rescaled for every individual plot as given in the colour bar in km/s. Black solid circles indicate one effective radius.

Although there is rotation in all maps, they do not show a kinematically distinct core or regular rotation. Since galaxies of this type exhibit various completely distinct features, rather than one characteristic like the other groups, it is likely that there are multiple different formation pathways that lead to galaxies included in this group.

Group c

This group is defined by very distinct kinematical structures: The central region shows a kinematically decoupled rotating component either, completely independent of its environment (KDC) or even counter-rotating (CRC).

Fig. 4.4 illustrates four examples for members of this group identifies in the Magneticum sample. In the first panel, the centre roughly extending to $1R_{\rm e}$, rotates opposite than its surrounding with a small kinematical twist. Hence it clearly represents a CRC.
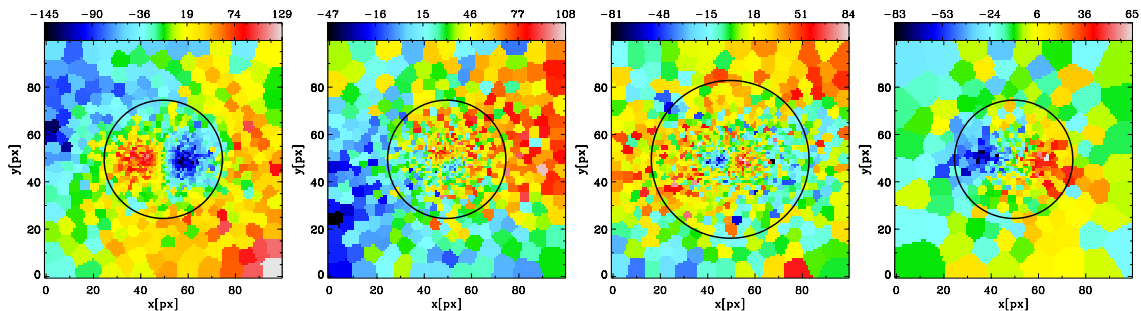

Figure 4.4.: Voronoi binned velocity maps of four members of group c for the simulated galaxies. The colours are rescaled for every individual plot as given in the colour bar in km/s. Black solid circles indicate one effective radius.

A similar pattern is visible in the third panel showing a less extended CRC. Furthermore, there seems to be a larger rotating structure inclined by 45° with respect to the core. The second panel two shows a special case of KDC, featuring a rotating core inclined 90° to the large scale rotation. The core extends roughly out to half the effective radius.

Another characteristic feature for this group is a rotating core surrounded by a non rotating environment. Such a pattern is present in the fourth panel. There is a rotating core within $1R_{\rm e}$ encircled by a region showing comparatively low (near zero) velocities.

Group d

Group d is the only class determined by a feature in the velocity dispersion maps. Galaxies which feature two off-centred peaks separated by at least half the effective radius are assigned to this group. The two peaks are interpreted as two counter-rotating flattened components which can have various relative luminosity contributions (Emsellem et al., 2011). Such systems can be formed through merging of two spiral galaxies with opposes intrinsic spin (Crocker et al., 2009). Although there are several formation channels Emsellem et al. (2011) concludes that most probably a gas-rich merger or accretion event is required.

Galaxies of this type are very rare in the simulated sample. We only find three objects of this type. Moreover, the maps shown in fig. 4.5 do not feature peaks as clear as in the observations (Krajnović et al., 2011).
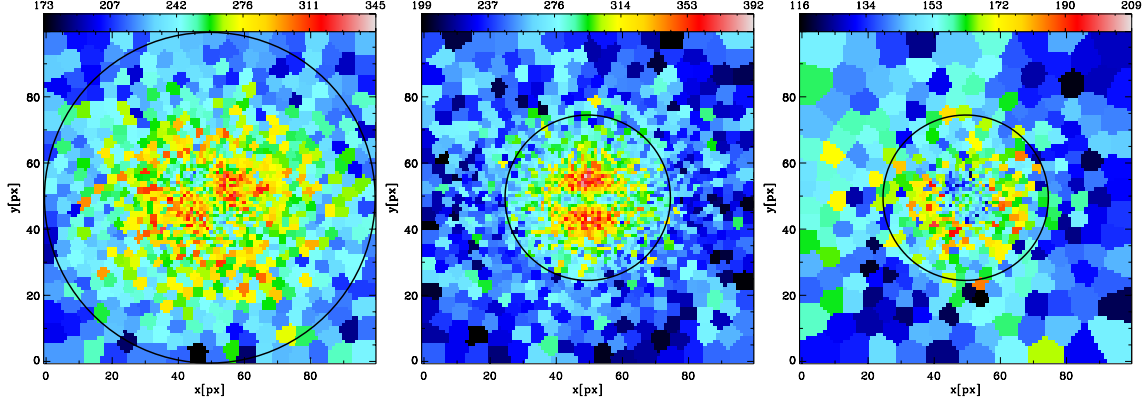

Figure 4.5.: Voronoi binned velocity dispersion maps of four members of group d. The colours are rescaled for every individual plot as given in the colour bar in km/s. Black solid circles indicate one effective radius.

In all three panels the peaks are well aligned with respect to each other. In the first and second pictures the requirement for a separation of at least half the effective radius is not fulfilled. Although the third panel satisfies this demand, the σ-peaks are very weak. So we are not able to fully account for group d galaxies in the Magneticum sample. We want to note that for many galaxies the low spatial resolution of the voronoi binned maps makes it difficult to identify galaxies of this type.

When comparing the absolute values of the maps to the observations, we find significantly higher values. Only one out of eleven observed 2σ galaxies reaches similar values. There might be a connection between the lack of 2σ galaxies and the larger velocity dispersions in the simulation.

Group e

Members of this group exhibit a regular rotating velocity pattern with a receding and an approaching side almost axis symmetric with respect to the y axis. They are also denoted as regular rotators.

Such galaxies are mainly classified as fast rotators in the λ_{R_e}-ϵ_e plane due to their ordered rotation (see sec. 4.3 and Emsellem et al. (2011)). There are several formation pathways like ram-pressure stripping, strangulation, multiple minor and major mergers leading to such a kinematical. However, as mentioned in sec. 2.5.2, cosmological processes apart from mergers have not been investigated yet.

In fig. 4.6 we again plot four examples extracted from the Magneticum sample. All galaxies exhibit the characteristic velocity pattern stated above and are well

aligned with the minor axis, with only minor differences among them. Especially the first panel shows a core with maximum rotation velocities restricted to roughly half the effective radius. The maximum velocity regions of the residual galaxies are located near or outside the black circle. Comparing the absolute velocities the maps are in total agreement with the observations.
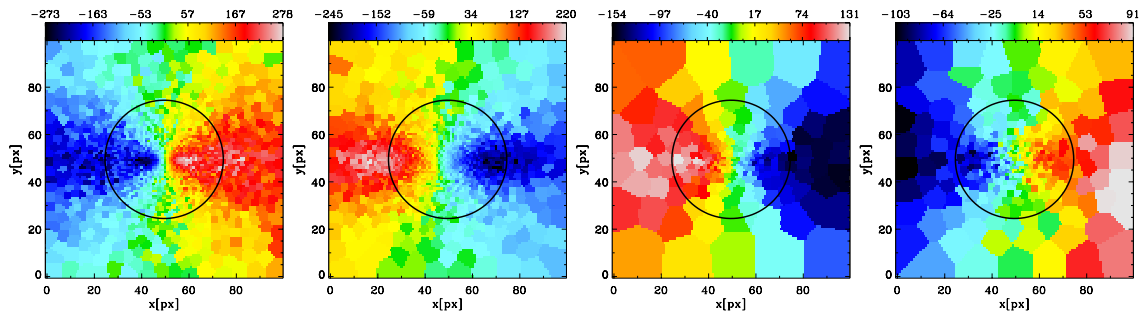

Figure 4.6.: Voronoi binned velocity maps of four members of group e for the simulated galaxies. The colours are rescaled for every individual plot as given in the colour bar in km/s. Black solid circles indicate one effective radius.

Anomaly

We briefly want to mention an anomaly found when surveying the velocity maps to assign them to the kinematical groups. We find a noticeable number of objects appearing to rotate around their projected major axis. Fig. 4.7 presents four exemplary velocity maps of these type of kinematics.
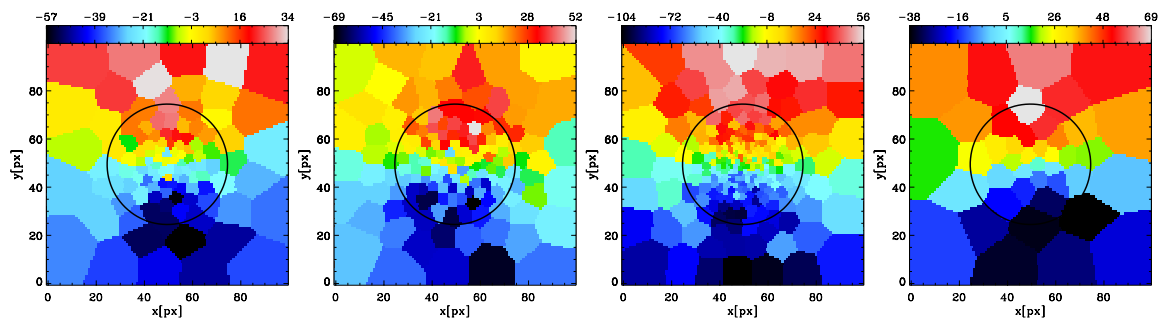

Figure 4.7.: Voronoi binned velocity maps of four simulated galaxies showing a difference of 0° between the projected major axis and the rotation axis.

In the ATLAS[3D] sample only one similar object is observed and assigned to group b. Theoretically, a prolate object rotating around its semi-major axis would exhibit such a velocity map, however, from the random projection displayed in fig. 4.7 it is not possible to confirm this speculation.

4.3. Classification of Kinematical Groups into Fast and Slow Rotators

After showing the existence of all kinematical groups in the magneticum sample in the previous section, we further investigate their nature by examining their position in the λ_{R_e}-ϵ_e plane. For this purpose we classify a subsample of galaxies from the Magneticum sample according to the kinematical groups. Because classifying the complete Magneticum sample is a cumbersome task, we only classify a subset of 188 objects. This subsample only includes galaxies which can confidently be assigned to one of the five groups, randomly picked from the complete sample. Thus it is not reasonable to compare the abundance of a certain group to observations, since we are biased by the selection process. However, we can very well compare the position in the λ_{R_e}-ϵ_e diagram to observations conducted by Krajnović et al. (2011) for the ATLAS[3D] sample. Therefore, fig. 4.8 displays the λ_{R_e}-ϵ_e diagram for the subsample, separating the kinematical groups by colour, as given in the legend.

From the definitions of group a and e we expect them to be clearly separated by the green line. Indeed, all group e galaxies in our subsample are classified as fast rotators, whereas group a galaxies are, except for three objects, classified as slow rotators. The three fast rotators in group a show low λ_{R_e} values near the fast-slow rotator threshold, lying slightly above the maximum λ_{R_e} for group a galaxies found in the observations. We have to keep in mind that the slow rotating regime is biased towards higher values due to statistical noise as outlined in sec. 2.5.2.

The λ_{R_e} distribution of group a and e nicely resemble the trend found in the observations. Looking at the ellipticities in the slow rotating regime, we find the same trend as in sec. 2.5.2 for the slow rotators to be more elongated as in the observations.

Members of group b and c are clustered below or in the vicinity of the green line, showing slightly larger λ_{R_e} values than the observations. For group b it is difficult to visually identify members, since a large variety of kinematical patterns are collected in this group. The slightly larger values for group c might also be induced by identification process: A galaxy which shows a clear KDC on the scale of $2R_e$ might be classified as a group e galaxy on the scale of $1R_e$.

The low number of group d galaxies does not allow for a meaningful comparison. We only mention that non of the three members lies far of the observations.

Taking the differences in the classification schemes into account we conclude a similar trend as found in the observations for group e galaxies to be classified as fast rotators, whereas members of group a,b and c cluster below or near the fast-slow rotator threshold.

The velocity maps for the galaxies in the subsample are shown in app. A. The dispersion maps for group d galaxies are shown in fig. 4.5
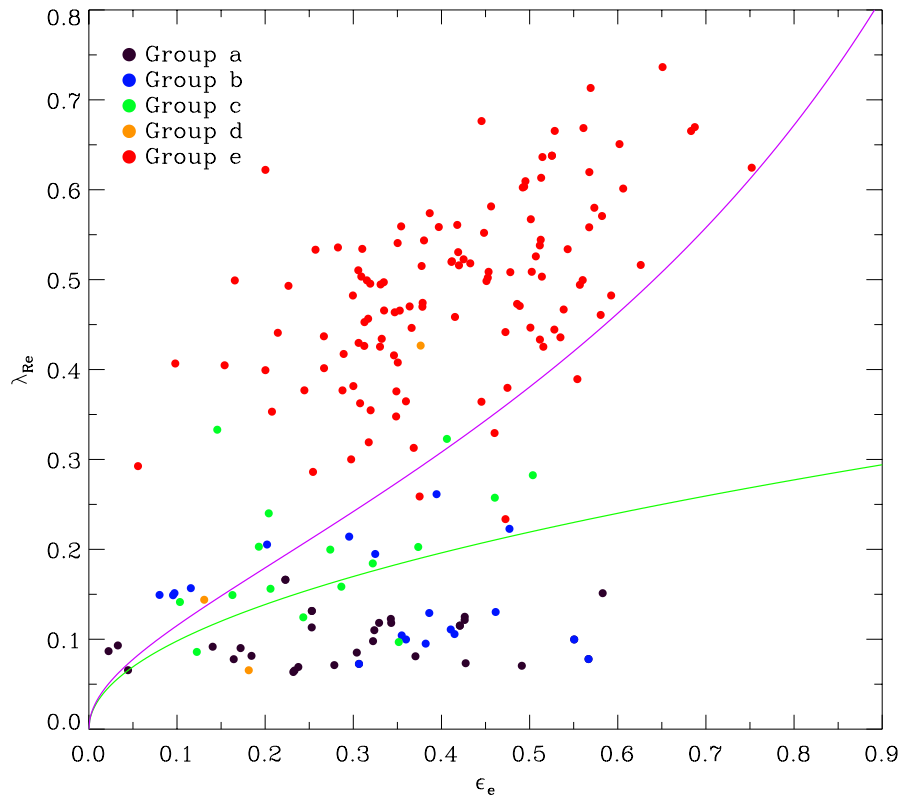
Figure 4.8.: λ_{R_e}-ϵ_e plane for a subsample of galaxies. Colours distinguish the five kine-
matical groups as given in the legend. The green solid line indicates the
threshold between fast and slow rotators and the lilac line represents the
edge-on view for a certain anisotropy parameter as in the λ_{R_e}-ϵ_e diagram
before.

5. Summary and Conclusion

Recent observations revealed a shift in the existing paradigm for early-type galaxies away from the classical morphological separation into elliptical galaxies and S0 mostly driven by the observed ellipticities, towards a classification based on fundamental kinematical properties. The picture of early-type galaxies to be kinematically unimpressive has been revolutionised by observing a richness of complex kinematical structures, suggesting a variety of different formation histories.

In this study we investigated the kinematical properties of a sample of 1334 galaxies extracted from the Magneticum Pathfinder simulation, which are a set of hydrodynamical simulations performed with the Tree/SPH code GADGET-3. We selected all galaxies with $M_* > 1 \cdot 10^{10} M_\odot$ and a cold gas fraction below 0.1, to ensure maximal comparability to the galaxy selection process adopted for the ATLAS^{3D} observations.

One of the most important quantities to describe the different kinematical behaviours of galaxies is the λ_{R_e}-parameter, which encodes information about the projected angular momentum as well as the amount of random motion. It was introduced by Emsellem et al. (2007) to distinguish between early-type galaxies without or only low rotation, so-called slow rotators, and early-type galaxies showing a rotational supported kinematical structure, called fast rotators.

In a first technical part we introduced three tessellation schemes to handle the issue of statistical noise in the calculation of λ_{R_e}, caused by the nature of SPH simulations. Based on its stability and the possibility to determine a target-particle number we choose the centroidal voronoi tessellation method for this study.

The comparison of the λ_{R_e}-ϵ_e plane found for the Magneticum sample to ATLAS^{3D} and CALIFA observations revealed a remarkable agreement:

- We classify 83%(1103/1334) of the galaxies as fast rotators, accordingly 17% (231/1334) of the sample is slow rotating. Thus we are in perfect agreement with the 86%(224/260) and 14%(36/260) found in the observations for fast and slow rotators, respectively.

- The fast rotating regime is in substantial agreement with the observations showing only minor deviations in the extreme elongated region. In contrast to former studies which build fast rotators through isolated mergers we reach the extreme fast rotating regime with $\lambda_{R_e} > 0.65$. We interpret this as a hint for formation processes like strangulation or ram-pressure striping of disc galaxies, only present in a fully cosmological context.

- In the slow rotating branch we are biased by statistical noise that causes a lower limit for λ_{R_e} of 0.07. When comparing the ellipticities in this regime, the Magneticum sample shows slightly larger values than the observations.

- When comparing the mass distribution in the λ_{R_e}-ϵ_e diagram we find a similar trend for slow rotators to be more massive than fast rotators, however, we do not find our most massive galaxies in the extreme round, slow-rotating regime.

From the results summarised above we conclude a proper treatment of the physical processes within the Magneticum simulation which are responsible for the kinematical bimodality of fast and slow rotors observed in the ATLAS[3D] sample. Thus, we investigated the connection between a galaxy classification based on the position of the galaxy in the M_*-J_* plane parametrised by the b-value, with the kinematical bimodality of fast and slow rotators. We found a smooth transition of b-values towards larger values with increasing λ_{R_e}. From the fact that the extremely fast rotating regime is populated by galaxies with disc-like b-values we constrain a coevolution of M_* and J_* during the formation process of these objects. This again suggests non-violent processes like strangulation or ram-pressure stripping of a disc galaxy, as mentioned before.

Furthermore, we confirm that the Sérsic index alone is not sufficient to disentangle fast and slow rotators, showing only a weak trend to decrease with decreasing λ_{R_e}. The weak correlation between Sérsic index and b-value substantiates the inconsistency of kinematical and morphological classifications.

We calculated the misalignment angles between kinematics and morphology for the complete Magneticum sample, defined as the angles between the total angular momentum and the principle axis of inertia. It revealed a remarkable alignment, implying that the majority of the galaxies in our sample are oblate and axial symmetric with minor axis rotation. By separating fast and slow rotators, we confirmed that fast rotators are significantly aligned, while slow rotators only show a weak trend of alignment corresponding to a broad range of misalignment angles. This behaviour is in very good agreement with the observational results for the ATLAS[3D] sample. Furthermore we explore the relationship between the misalignment angle and the b-value, showing a distinct trend for ETGs with larger b-value to be significantly better aligned compared to low b-value objects. Combining this results with the poor correlation between the Sérsic index and b we conclude that even ETGs with large Sérsic index can be well aligned, again showing the inconsistency of the Sérsic index with kinematics.

In order to further verify the oblate and axial symmetric shape of aligned galaxies, we introduce the "oblateness" parameter n_{ob}, which is based on the quotients of the principle moments of inertia. It beautifully confirms that objects with a misalignment angle lower than 15° exhibit a oblate shape. The distribution for ETGs with an angle larger than 15° features a scatter in the prolate and oblate region, most probable due to external interaction and triaxiality. Moreover, the correlation between the b-value and n_{ob} is investigated in this study. According to the notion

that larger b-values correspond to disc-like objects it reveals an oblate shape in this range, followed by a smooth transition to a more prolate shapes for low b-values.

Observation suggest a further separation of fast and slow rotators into five kinematical groups based on the presence of certain kinematical features in the velocity and dispersion maps. We find evidence for the existence of all groups within the Magneticum sample. Although there are examples for the group of 2σ galaxies, the appearance of the dispersion peaks is not in perfect agreement with the observations. In addition, only three out of 1334 galaxies are assigned to this group which is significantly less than what would be expected from the observations. The distribution of the five groups in the λ_{R_e}-ϵ_e diagram is in general consistent with observations. It nicely resembles the separation ob non- and regular rotators by the fast-slow rotator threshold. Only the group of kinematically distinct cores shows slightly higher λ_{R_e} values than it is observed in the ATLAS^{3D} sample.

The results of this study serve as the basis to study the formation of fast and slow rotators, and even their kinematical subgroups, in a fully cosmological context. Especially potential environmental effects and the role of formation processes apart from merger can be explored in great detail. However, further investigation has to be conducted to clarify minor disagreements, like the large ellipticities of slow rotators, or the lack of 2σ galaxies. An improvement of resolution in the future will allow for a more meaningful comparison of the extreme slow rotating regime, and a larger box size with the same resolution to enhance the number of massive spheroidals in the simulation will enable a more detailed study of the most massive spheroidal galaxies in the universe.

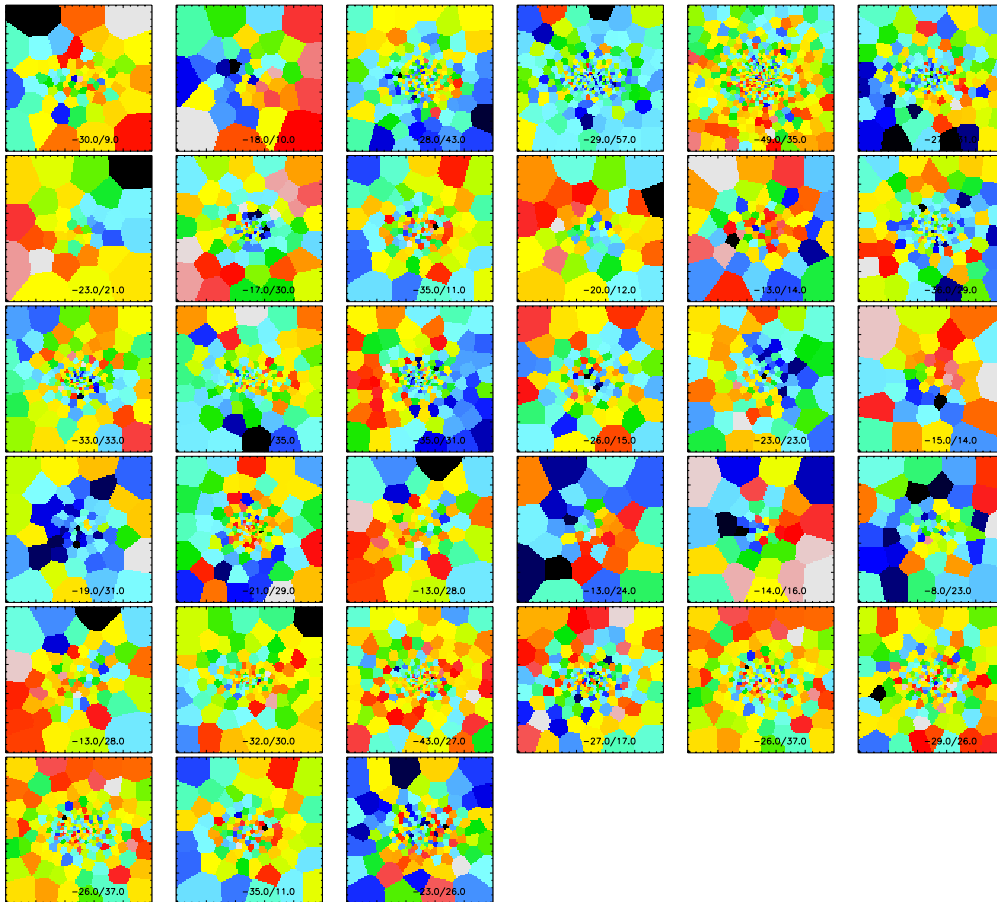# A. Appendix: Kinematical Maps of Galaxies Classified in sec. 4.3

Figure A.1.: Velocity maps of the galaxies of the kinematic group a. Maps are voronoi binned. The side length of each panel is $4R_e$. Orientation is such that the morphological major axis is horizontal and that the receding side is on the left. The numbers in lower right corners show the range of the plotted velocities in km/s.
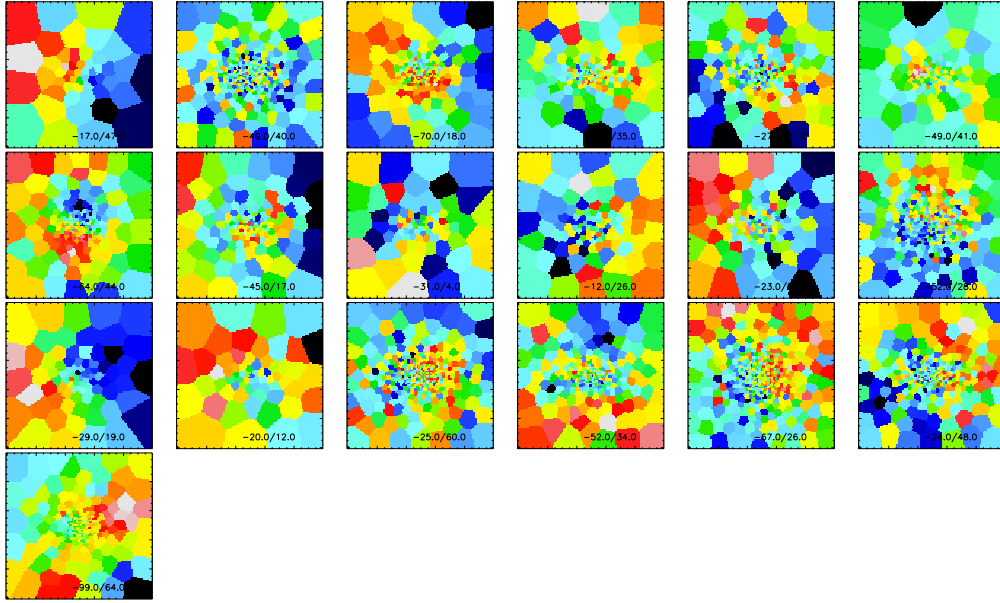
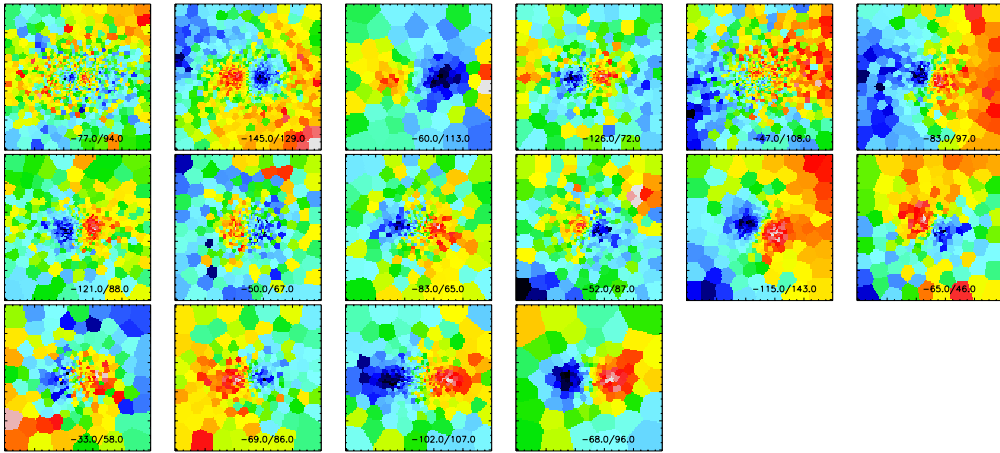**Figure A.2.:** Same as fig. A.1, but for galaxies of kinematical group b.

Figure A.3.: Same as fig. A.1, but for galaxies of kinematical group c. The third panel has a side length of only $1.2R_\mathrm{e}$ to improve the visibility of the KDC.
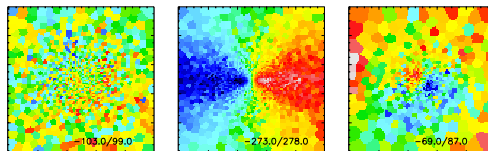

Figure A.4.: Same as fig. A.1, but for galaxies of kinematical group d.
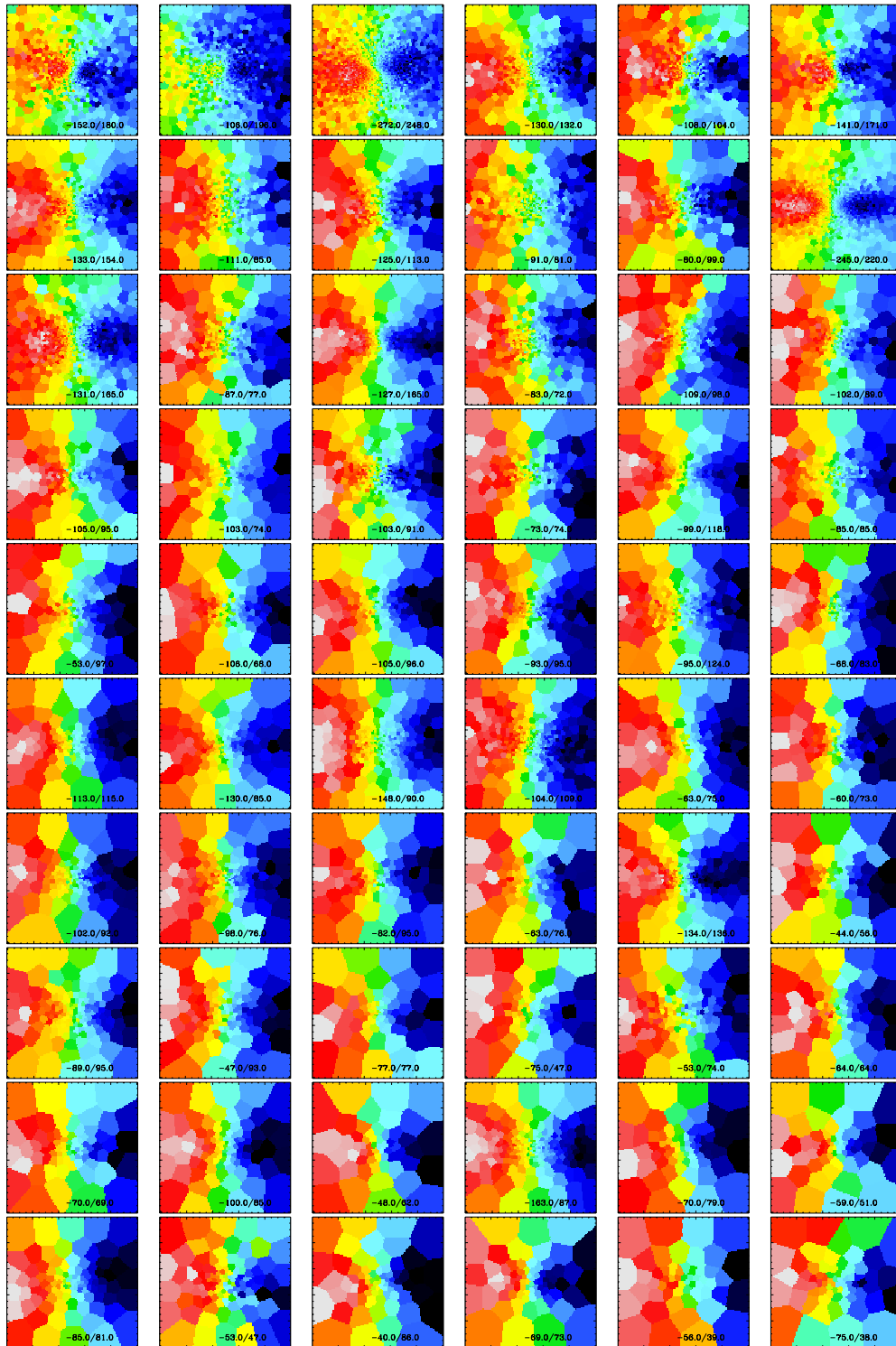
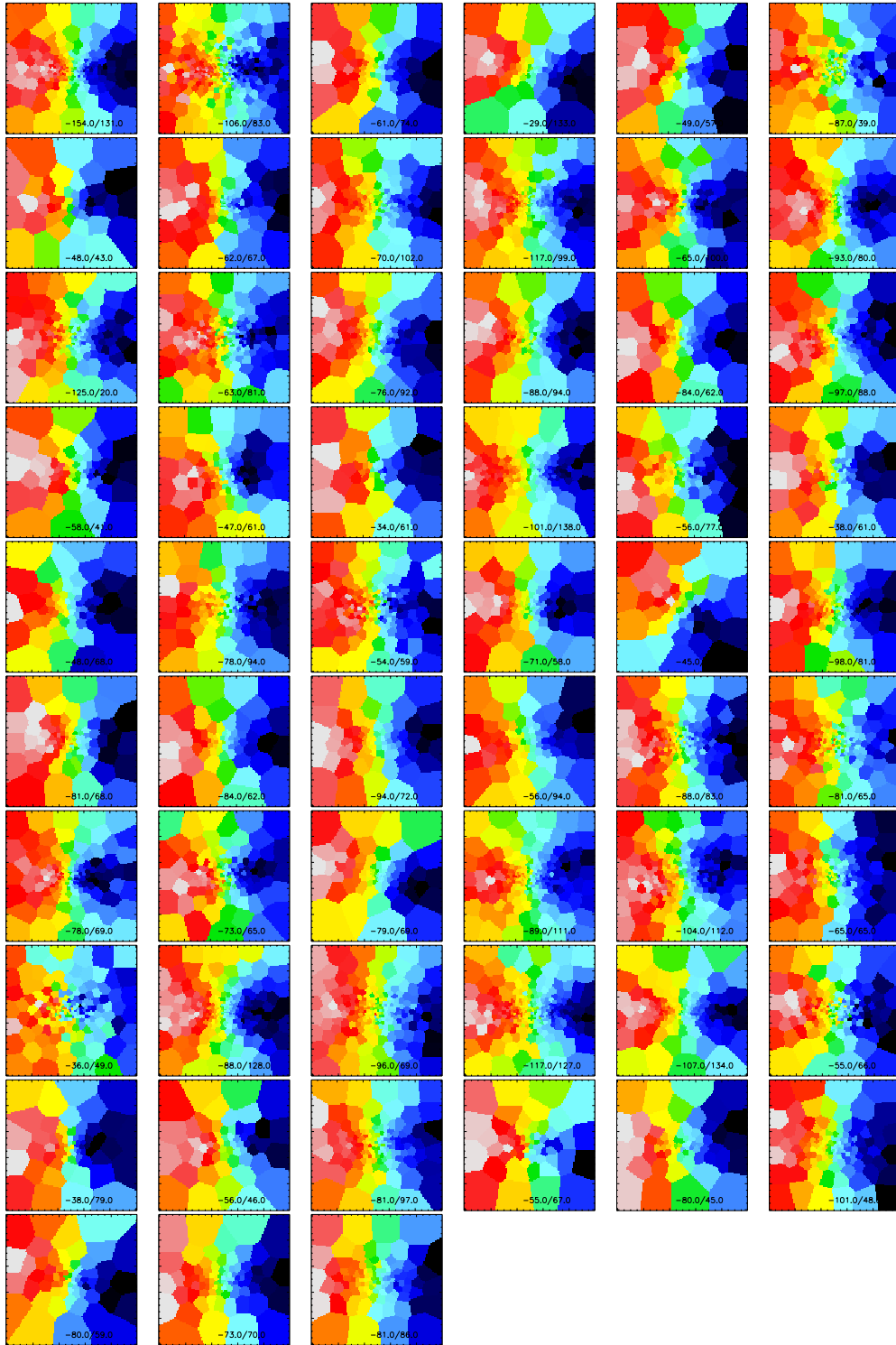**Figure A.5.:** Same as fig. A.1, but for galaxies of kinematical group e.

Figure A.6.: Same as fig. A.1, but for galaxies of kinematical group e.

Acknowledgements

I want to thank all people who supported me during the writing of this thesis and my entire course of studies.

First of all I want to thank PD Dr. Klaus Dolag for many fruitful discussions and unconditional helpfulness. Thank you for many useful comments and giving me the opportunity to work with the Magneticum Pathfinder simulations.

Furthermore, I want to thank Prof. Andreas Burkert for giving me the opportunity to work in the CAST group. It was a pleasure to work in such an interesting and supportive group.

I would like to thank Dr. Rhea-Silvia Remus for answering many questions and showing so much excitement for my work. I also want to thank my officemate Adelheid Teklu for the fun and helpful discussions. Thanks are due to Tadziu Hoffmann for all matters concerning failing computers.

Finally, I want to thank my family and girlfriend for sometimes knowing me better than I know myself. Thanks for your support during my whole studies, especially in difficult times.

Bibliography

Abadi, M. G., Moore, B., and Bower, R. G. (1999). Ram pressure stripping of spiral galaxies in clusters. *Monthly Notices of the Royal Astronomical Society*, 308:947–954.

Bacon, R., Copin, Y., Monnet, G., Miller, B. W., Allington-Smith, J. R., Bureau, M., Carollo, C. M., Davies, R. L., Emsellem, E., Kuntschner, H., Peletier, R. F., Verolme, E. K., and de Zeeuw, P. T. (2001). The SAURON project - I. The panoramic integral-field spectrograph. *Monthly Notices of the Royal Astronomical Society*, 326:23–35.

Baldry, I. K., Driver, S. P., Loveday, J., Taylor, E. N., Kelvin, L. S., Liske, J., Norberg, P., Robotham, A. S. G., Brough, S., Hopkins, A. M., Bamford, S. P., Peacock, J. A., Bland-Hawthorn, J., Conselice, C. J., Croom, S. M., Jones, D. H., Parkinson, H. R., Popescu, C. C., Prescott, M., Sharp, R. G., and Tuffs, R. J. (2012). Galaxy And Mass Assembly (GAMA): the galaxy stellar mass function at z ¡ 0.06. *Monthly Notices of the Royal Astronomical Society*, 421:621–634.

Beck, A. M., Murante, G., Arth, A., Remus, R.-S., Teklu, A. F., Donnert, J. M. F., Planelles, S., Beck, M. C., Foerster, P., Imgrund, M., Dolag, K., and Borgani, S. (2015). An improved SPH scheme for cosmological simulations. *ArXiv e-prints*.

Bender, R. (1987). Kinematics and Morphology of Elliptical Galaxies. *Mitteilungen der Astronomischen Gesellschaft Hamburg*, 70:226.

Bender, R., Surma, P., Doebereiner, S., Moellenhoff, C., and Madejsky, R. (1989). Isophote shapes of elliptical galaxies. II - Correlations with global optical, radio and X-ray properties. *A&A*, 217:35–43.

Bois, M., Bournaud, F., Emsellem, E., Alatalo, K., Blitz, L., Bureau, M., Cappellari, M., Davies, R. L., Davis, T. A., de Zeeuw, P. T., Duc, P.-A., Khochfar, S., Krajnović, D., Kuntschner, H., Lablanche, P.-Y., McDermid, R. M., Morganti, R., Naab, T., Oosterloo, T., Sarzi, M., Scott, N., Serra, P., Weijmans, A., and Young, L. M. (2010). Formation of slowly rotating early-type galaxies via major mergers: a resolution study. *Monthly Notices of the Royal Astronomical Society*, 406:2405–2420.

Bois, M., Emsellem, E., Bournaud, F., Alatalo, K., Blitz, L., Bureau, M., Cappellari, M., Davies, R. L., Davis, T. A., de Zeeuw, P. T., Duc, P.-A., Khochfar, S., Krajnović, D., Kuntschner, H., Lablanche, P.-Y., McDermid, R. M., Morganti,

R., Naab, T., Oosterloo, T., Sarzi, M., Scott, N., Serra, P., Weijmans, A.-M., and Young, L. M. (2011). The ATLAS^{3D} project - VI. Simulations of binary galaxy mergers and the link with fast rotators, slow rotators and kinematically distinct cores. *Monthly Notices of the Royal Astronomical Society*, 416:1654–1679.

Brammer, G. B., Whitaker, K. E., van Dokkum, P. G., Marchesini, D., Franx, M., Kriek, M., Labbé, I., Lee, K.-S., Muzzin, A., Quadri, R. F., Rudnick, G., and Williams, R. (2011). The Number Density and Mass Density of Star-forming and Quiescent Galaxies at 0.4 ¡= z ¡= 2.2. *The Astrophysical Journal*, 739:24.

Burkert, A. and Naab, T. (2003). Major Mergers and the Origin of Elliptical Galaxies. In Contopoulos, G. and Voglis, N., editors, *Galaxies and Chaos*, volume 626 of *Lecture Notes in Physics, Berlin Springer Verlag*, pages 327–339.

Cappellari, M. (2009). Voronoi binning: Optimal adaptive tessellations of multidimensional data. *ArXiv e-prints*.

Cappellari, M. and Copin, Y. (2003). Adaptive spatial binning of integral-field spectroscopic data using Voronoi tessellations. *Monthly Notices of the Royal Astronomical Society*, 342:345–354.

Cappellari, M., Emsellem, E., Bacon, R., Bureau, M., Davies, R. L., de Zeeuw, P. T., Falcón-Barroso, J., Krajnović, D., Kuntschner, H., McDermid, R. M., Peletier, R. F., Sarzi, M., van den Bosch, R. C. E., and van de Ven, G. (2007). The SAURON project - X. The orbital anisotropy of elliptical and lenticular galaxies: revisiting the (V/σ, ϵ) diagram with integral-field stellar kinematics. *Monthly Notices of the Royal Astronomical Society*, 379:418–444.

Cappellari, M., Emsellem, E., Krajnović, D., McDermid, R. M., Scott, N., Verdoes Kleijn, G. A., Young, L. M., Alatalo, K., Bacon, R., Blitz, L., Bois, M., Bournaud, F., Bureau, M., Davies, R. L., Davis, T. A., de Zeeuw, P. T., Duc, P.-A., Khochfar, S., Kuntschner, H., Lablanche, P.-Y., Morganti, R., Naab, T., Oosterloo, T., Sarzi, M., Serra, P., and Weijmans, A.-M. (2011). The ATLAS^{3D} project - I. A volume-limited sample of 260 nearby early-type galaxies: science goals and selection criteria. *Monthly Notices of the Royal Astronomical Society*, 413:813–836.

Cappellari, M., McDermid, R. M., Alatalo, K., Blitz, L., Bois, M., Bournaud, F., Bureau, M., Crocker, A. F., Davies, R. L., Davis, T. A., de Zeeuw, P. T., Duc, P.-A., Emsellem, E., Khochfar, S., Krajnović, D., Kuntschner, H., Morganti, R., Naab, T., Oosterloo, T., Sarzi, M., Scott, N., Serra, P., Weijmans, A.-M., and Young, L. M. (2013). The ATLAS^{3D} project - XX. Mass-size and mass-σ distributions of early-type galaxies: bulge fraction drives kinematics, mass-to-light ratio, molecular gas fraction and stellar initial mass function. *Monthly Notices of the Royal Astronomical Society*, 432:1862–1893.

Cicone, C., Maiolino, R., Sturm, E., Graciá-Carpio, J., Feruglio, C., Neri, R., Aalto, S., Davies, R., Fiore, F., Fischer, J., García-Burillo, S., González-Alfonso, E., Hailey-Dunsheath, S., Piconcelli, E., and Veilleux, S. (2014). Massive molecular outflows and evidence for AGN feedback from CO observations. *A&A*, 562:A21.

Ciotti, L. and Bertin, G. (1999). Analytical properties of the $R^{1/m}$ law. *A&A*, 352:447–451.

Crocker, A. F., Jeong, H., Komugi, S., Combes, F., Bureau, M., Young, L. M., and Yi, S. (2009). Molecular gas and star formation in the red-sequence counter-rotating disc galaxy NGC 4550. *Monthly Notices of the Royal Astronomical Society*, 393:1255–1264.

Croft, R. A. C., Di Matteo, T., Springel, V., and Hernquist, L. (2009). Galaxy morphology, kinematics and clustering in a hydrodynamic simulation of a Λ cold dark matter universe. *Monthly Notices of the Royal Astronomical Society*, 400:43–67.

de Sitter, W. (1916a). Einstein's theory of gravitation and its astronomical consequences. *Monthly Notices of the Royal Astronomical Society*, 76:699–728.

de Sitter, W. (1916b). On Einstein's theory of gravitation and its astronomical consequences. Second paper. *Monthly Notices of the Royal Astronomical Society*, 77:155–184.

de Sitter, W. (1917). Einstein's theory of gravitation and its astronomical consequences. Third paper. *Monthly Notices of the Royal Astronomical Society*, 78:3–28.

de Vaucouleurs, G. (1948). Recherches sur les nébuleuses extragalactiques. *Journal des Observateurs*, 31:113.

Dekel, A. and Birnboim, Y. (2006). Galaxy bimodality due to cold flows and shock heating. *Monthly Notices of the Royal Astronomical Society*, 368:2–20.

Dekel, A., Birnboim, Y., Engel, G., Freundlich, J., Goerdt, T., Mumcuoglu, M., Neistein, E., Pichon, C., Teyssier, R., and Zinger, E. (2009). Cold streams in early massive hot haloes as the main mode of galaxy formation. *Nature*, 457:451–454.

Diamond-Stanic, A. M., Moustakas, J., Tremonti, C. A., Coil, A. L., Hickox, R. C., Robaina, A. R., Rudnick, G. H., and Sell, P. H. (2012). High-velocity Outflows without AGN Feedback: Eddington-limited Star Formation in Compact Massive Galaxies. *The Astrophysical Journal*, 755:L26.

Dolag, K., Borgani, S., Murante, G., and Springel, V. (2009). Substructures in hydrodynamical cluster simulations. *Monthly Notices of the Royal Astronomical Society*, 399:497–514.

Dolag, K., Vazza, F., Brunetti, G., and Tormen, G. (2005). Turbulent gas motions in galaxy cluster simulations: the role of smoothed particle hydrodynamics viscosity. *Monthly Notices of the Royal Astronomical Society*, 364:753–772.

Einstein, A. (1915). Zur allgemeinen Relativitätstheorie. *Sitzungsberichte der Königlich Preußischen Akademie der Wissenschaften (Berlin), Seite 778-786.*, pages 778–786.

Emsellem, E., Cappellari, M., Krajnović, D., Alatalo, K., Blitz, L., Bois, M., Bournaud, F., Bureau, M., Davies, R. L., Davis, T. A., de Zeeuw, P. T., Khochfar, S., Kuntschner, H., Lablanche, P.-Y., McDermid, R. M., Morganti, R., Naab, T., Oosterloo, T., Sarzi, M., Scott, N., Serra, P., van de Ven, G., Weijmans, A.-M., and Young, L. M. (2011). The ATLAS^{3D} project - III. A census of the stellar angular momentum within the effective radius of early-type galaxies: unveiling the distribution of fast and slow rotators. *Monthly Notices of the Royal Astronomical Society*, 414:888–912.

Emsellem, E., Cappellari, M., Krajnović, D., van de Ven, G., Bacon, R., Bureau, M., Davies, R. L., de Zeeuw, P. T., Falcón-Barroso, J., Kuntschner, H., McDermid, R., Peletier, R. F., and Sarzi, M. (2007). The SAURON project - IX. A kinematic classification for early-type galaxies. *Monthly Notices of the Royal Astronomical Society*, 379:401–417.

Faber, S. M. and Jackson, R. E. (1976). Velocity dispersions and mass-to-light ratios for elliptical galaxies. *The Astrophysical Journal*, 204:668–683.

Fall, S. M. (1983). Galaxy formation - Some comparisons between theory and observation. In Athanassoula, E., editor, *Internal Kinematics and Dynamics of Galaxies*, volume 100 of *IAU Symposium*, pages 391–398.

Ferrarese, L., Côté, P., Jordán, A., Peng, E. W., Blakeslee, J. P., Piatek, S., Mei, S., Merritt, D., Milosavljević, M., Tonry, J. L., and West, M. J. (2006). The ACS Virgo Cluster Survey. VI. Isophotal Analysis and the Structure of Early-Type Galaxies. *Astrophysical Journal Supplement Series*, 164:334–434.

Förster Schreiber, N. M., Genzel, R., Newman, S. F., Kurk, J. D., Lutz, D., Tacconi, L. J., Wuyts, S., Bandara, K., Burkert, A., Buschkamp, P., Carollo, C. M., Cresci, G., Daddi, E., Davies, R., Eisenhauer, F., Hicks, E. K. S., Lang, P., Lilly, S. J., Mainieri, V., Mancini, C., Naab, T., Peng, Y., Renzini, A., Rosario, D., Shapiro Griffin, K., Shapley, A. E., Sternberg, A., Tacchella, S., Vergani, D., Wisnioski, E., Wuyts, E., and Zamorani, G. (2014). The Sins/zC-Sinf Survey of z ~ 2 Galaxy Kinematics: Evidence for Powerful Active Galactic Nucleus-Driven Nuclear Outflows in Massive Star-Forming Galaxies. *The Astrophysical Journal*, 787:38.

Franx, M., Illingworth, G., and de Zeeuw, T. (1991). The ordered nature of elliptical galaxies - Implications for their intrinsic angular momenta and shapes. *The Astrophysical Journal*, 383:112–134.

Friedmann, A. (1922). Über die Krümmung des Raumes. *Zeitschrift fur Physik*, 10:377–386.

Gerhard, O. E. (1981). N-body simulations of disc-halo galaxies - Isolated systems, tidal interactions and merging. *Monthly Notices of the Royal Astronomical Society*, 197:179–208.

Gerhard, O. E. (1993). Line-of-sight velocity profiles in spherical galaxies: breaking the degeneracy between anisotropy and mass. *Monthly Notices of the Royal Astronomical Society*, 265:213.

Hernquist, L. (1992). Structure of merger remnants. I - Bulgeless progenitors. *The Astrophysical Journal*, 400:460–475.

Hirschmann, M., Dolag, K., Saro, A., Bachmann, L., Borgani, S., and Burkert, A. (2014). Cosmological simulations of black hole growth: AGN luminosities and downsizing. *Monthly Notices of the Royal Astronomical Society*, 442:2304–2324.

Hubble, E. P. (1926). Extragalactic nebulae. *The Astrophysical Journal*, 64:321–369.

Jesseit, R., Cappellari, M., Naab, T., Emsellem, E., and Burkert, A. (2009). Specific angular momentum of disc merger remnants and the λ_R-parameter. *Monthly Notices of the Royal Astronomical Society*, 397:1202–1214.

Khochfar, S., Emsellem, E., Serra, P., Bois, M., Alatalo, K., Bacon, R., Blitz, L., Bournaud, F., Bureau, M., Cappellari, M., Davies, R. L., Davis, T. A., de Zeeuw, P. T., Duc, P.-A., Krajnović, D., Kuntschner, H., Lablanche, P.-Y., McDermid, R. M., Morganti, R., Naab, T., Oosterloo, T., Sarzi, M., Scott, N., Weijmans, A.-M., and Young, L. M. (2011). The ATLAS^{3D} project - VIII. Modelling the formation and evolution of fast and slow rotator early-type galaxies within ΛCDM. *Monthly Notices of the Royal Astronomical Society*, 417:845–862.

Komatsu, E., Smith, K. M., Dunkley, J., Bennett, C. L., Gold, B., Hinshaw, G., Jarosik, N., Larson, D., Nolta, M. R., Page, L., Spergel, D. N., Halpern, M., Hill, R. S., Kogut, A., Limon, M., Meyer, S. S., Odegard, N., Tucker, G. S., Weiland, J. L., Wollack, E., and Wright, E. L. (2011). Seven-year Wilkinson Microwave Anisotropy Probe (WMAP) Observations: Cosmological Interpretation. *Astrophysical Journal Supplement Series*, 192:18.

Kormendy, J. and Bender, R. (1996). A Proposed Revision of the Hubble Sequence for Elliptical Galaxies. *The Astrophysical Journal*, 464:L119.

Krajnović, D., Alatalo, K., Blitz, L., Bois, M., Bournaud, F., Bureau, M., Cappellari, M., Davies, R. L., Davis, T. A., de Zeeuw, P. T., Duc, P.-A., Emsellem, E., Khochfar, S., Kuntschner, H., McDermid, R. M., Morganti, R., Naab, T., Oosterloo, T., Sarzi, M., Scott, N., Serra, P., Weijmans, A.-M., and Young, L. M. (2013). The ATLAS^{3D} project - XVII. Linking photometric and kinematic signatures of stellar discs in early-type galaxies. *Monthly Notices of the Royal Astronomical Society*, 432:1768–1795.

Krajnović, D., Emsellem, E., Cappellari, M., Alatalo, K., Blitz, L., Bois, M., Bournaud, F., Bureau, M., Davies, R. L., Davis, T. A., de Zeeuw, P. T., Khochfar, S., Kuntschner, H., Lablanche, P.-Y., McDermid, R. M., Morganti, R., Naab, T., Oosterloo, T., Sarzi, M., Scott, N., Serra, P., Weijmans, A.-M., and Young, L. M. (2011). The ATLAS^{3D} project - II. Morphologies, kinemetric features and alignment between photometric and kinematic axes of early-type galaxies. *Monthly Notices of the Royal Astronomical Society*, 414:2923–2949.

Lin, C. C. and Shu, F. H. (1964). On the Spiral Structure of Disk Galaxies. *The Astrophysical Journal*, 140:646.

Lotz, J. M., Jonsson, P., Cox, T. J., Croton, D., Primack, J. R., Somerville, R. S., and Stewart, K. (2011). The Major and Minor Galaxy Merger Rates at z ¡ 1.5. *The Astrophysical Journal*, 742:103.

Madau, P. and Dickinson, M. (2014). Cosmic Star-Formation History. *Annual review of astronomy and astrophysics*, 52:415–486.

Mo, H., van den Bosch, F. C., and White, S. (2010). *Galaxy Formation and Evolution*.

Moody, C. E., Romanowsky, A. J., Cox, T. J., Novak, G. S., and Primack, J. R. (2014). Simulating multiple merger pathways to the central kinematics of early-type galaxies. *Monthly Notices of the Royal Astronomical Society*, 444:1475–1485.

Mukhanov, V. F. and Chibisov, G. V. (1981). Quantum fluctuations and the "non-singular" universe. *Pisma v Zhurnal Eksperimentalnoi i Teoreticheskoi Fiziki*, 33:549–553.

Naab, T., Oser, L., Emsellem, E., Cappellari, M., Krajnović, D., McDermid, R. M., Alatalo, K., Bayet, E., Blitz, L., Bois, M., Bournaud, F., Bureau, M., Crocker, A., Davies, R. L., Davis, T. A., de Zeeuw, P. T., Duc, P.-A., Hirschmann, M., Johansson, P. H., Khochfar, S., Kuntschner, H., Morganti, R., Oosterloo, T., Sarzi, M., Scott, N., Serra, P., Ven, G. v. d., Weijmans, A., and Young, L. M. (2014). The ATLAS^{3D} project - XXV. Two-dimensional kinematic analysis of simulated galaxies and the cosmological origin of fast and slow rotators. *Monthly Notices of the Royal Astronomical Society*, 444:3357–3387.

Navarro, J. F., Frenk, C. S., and White, S. D. M. (1996). The Structure of Cold Dark Matter Halos. *The Astrophysical Journal*, 462:563.

Oser, L., Ostriker, J. P., Naab, T., Johansson, P. H., and Burkert, A. (2010). The Two Phases of Galaxy Formation. *The Astrophysical Journal*, 725:2312–2323.

Pasquali, A., van den Bosch, F. C., and Rix, H.-W. (2007). The Isophotal Structure of Early-Type Galaxies in the SDSS: Dependence on Active Galactic Nucleus Activity and Environment. *The Astrophysical Journal*, 664:738–749.

Peng, Y., Maiolino, R., and Cochrane, R. (2015). Strangulation as the primary mechanism for shutting down star formation in galaxies. *Nature*, 521:192–195.

Penzias, A. A. and Wilson, R. W. (1965). A Measurement of Excess Antenna Temperature at 4080 Mc/s. *The Astrophysical Journal*, 142:419–421.

Planck Collaboration, Ade, P. A. R., Aghanim, N., Arnaud, M., Ashdown, M., Aumont, J., Baccigalupi, C., Banday, A. J., Barreiro, R. B., Bartlett, J. G., and et al. (2015). Planck 2015 results. XIII. Cosmological parameters. *ArXiv e-prints*.

Querejeta, M., Eliche-Moral, M. C., Tapia, T., Borlaff, A., van de Ven, G., Lyubenova, M., Martig, M., Falcón-Barroso, J., and Méndez-Abreu, J. (2015). Formation of S0 galaxies through mergers. Explaining angular momentum and concentration change from spirals to S0s. *A&A*, 579:L2.

Rodriguez-Gomez, V., Genel, S., Vogelsberger, M., Sijacki, D., Pillepich, A., Sales, L. V., Torrey, P., Snyder, G., Nelson, D., Springel, V., Ma, C.-P., and Hernquist, L. (2015). The merger rate of galaxies in the Illustris simulation: a comparison with observations and semi-empirical models. *Monthly Notices of the Royal Astronomical Society*, 449:49–64.

Romanowsky, A. J. and Fall, S. M. (2012). Angular Momentum and Galaxy Formation Revisited. *Astrophysical Journal Supplement Series*, 203:17.

Rubin, V. C., Thonnard, N., and Ford, Jr., W. K. (1978). Extended rotation curves of high-luminosity spiral galaxies. IV - Systematic dynamical properties, SA through SC. *The Astrophysical Journal*, 225:L107–L111.

Sánchez, S. F., Kennicutt, R. C., Gil de Paz, A., van de Ven, G., Vílchez, J. M., Wisotzki, L., Walcher, C. J., Mast, D., Aguerri, J. A. L., Albiol-Pérez, S., Alonso-Herrero, A., Alves, J., Bakos, J., Bartáková, T., Bland-Hawthorn, J., Boselli, A., Bomans, D. J., Castillo-Morales, A., Cortijo-Ferrero, C., de Lorenzo-Cáceres, A., Del Olmo, A., Dettmar, R.-J., Díaz, A., Ellis, S., Falcón-Barroso, J., Flores, H., Gallazzi, A., García-Lorenzo, B., González Delgado, R., Gruel, N., Haines, T., Hao, C., Husemann, B., Iglésias-Páramo, J., Jahnke, K., Johnson, B., Jungwiert, B., Kalinova, V., Kehrig, C., Kupko, D., López-Sánchez, Á. R., Lyubenova, M., Marino, R. A., Mármol-Queraltó, E., Márquez, I., Masegosa, J.,

Meidt, S., Mendez-Abreu, J., Monreal-Ibero, A., Montijo, C., Mourão, A. M., Palacios-Navarro, G., Papaderos, P., Pasquali, A., Peletier, R., Pérez, E., Pérez, I., Quirrenbach, A., Relaño, M., Rosales-Ortega, F. F., Roth, M. M., Ruiz-Lara, T., Sánchez-Blázquez, P., Sengupta, C., Singh, R., Stanishev, V., Trager, S. C., Vazdekis, A., Viironen, K., Wild, V., Zibetti, S., and Ziegler, B. (2012). CALIFA, the Calar Alto Legacy Integral Field Area survey. I. Survey presentation. *A&A*, 538:A8.

Sandage, A. (1961). *The Hubble atlas of galaxies.*

Sandage, A. (1975). *Classification and Stellar Content of Galaxies Obtained from Direct Photography*, page 1. the University of Chicago Press.

Sérsic, J. L. (1963). Influence of the atmospheric and instrumental dispersion on the brightness distribution in a galaxy. *Boletin de la Asociacion Argentina de Astronomia La Plata Argentina*, 6:41.

Shapiro, K. L., Falcón-Barroso, J., van de Ven, G., de Zeeuw, P. T., Sarzi, M., Bacon, R., Bolatto, A., Cappellari, M., Croton, D., Davies, R. L., Emsellem, E., Fakhouri, O., Krajnović, D., Kuntschner, H., McDermid, R. M., Peletier, R. F., van den Bosch, R. C. E., and van der Wolk, G. (2010). The SAURON project - XV. Modes of star formation in early-type galaxies and the evolution of the red sequence. *Monthly Notices of the Royal Astronomical Society*, 402:2140–2186.

Shen, S., Mo, H. J., White, S. D. M., Blanton, M. R., Kauffmann, G., Voges, W., Brinkmann, J., and Csabai, I. (2003). The size distribution of galaxies in the Sloan Digital Sky Survey. *Monthly Notices of the Royal Astronomical Society*, 343:978–994.

Springel, V. (2005). The cosmological simulation code GADGET-2. *Monthly Notices of the Royal Astronomical Society*, 364:1105–1134.

Springel, V., Di Matteo, T., and Hernquist, L. (2005). Modelling feedback from stars and black holes in galaxy mergers. *Monthly Notices of the Royal Astronomical Society*, 361:776–794.

Springel, V. and Hernquist, L. (2003). Cosmological smoothed particle hydrodynamics simulations: a hybrid multiphase model for star formation. *Monthly Notices of the Royal Astronomical Society*, 339:289–311.

Springel, V., White, S. D. M., Tormen, G., and Kauffmann, G. (2001a). Populating a cluster of galaxies - I. Results at [formmu2]z=0. *Monthly Notices of the Royal Astronomical Society*, 328:726–750.

Springel, V., Yoshida, N., and White, S. D. M. (2001b). GADGET: a code for collisionless and gasdynamical cosmological simulations. *n&a*, 6:79–117.

Teklu, A. F., Remus, R.-S., Dolag, K., Beck, A. M., Burkert, A., Schmidt, A. S., Schulze, F., and Steinborn, L. K. (2015). Connecting Angular Momentum and Galactic Dynamics: The Complex Interplay between Spin, Mass, and Morphology. *The Astrophysical Journal*, 812:29.

Toomre, A. (1977). Theories of spiral structure. *Annual review of astronomy and astrophysics*, 15:437–478.

Tornatore, L., Borgani, S., Dolag, K., and Matteucci, F. (2007). Chemical enrichment of galaxy clusters from hydrodynamical simulations. *Monthly Notices of the Royal Astronomical Society*, 382:1050–1072.

Tsatsi, A., Macciò, A. V., van de Ven, G., and Moster, B. P. (2015). A New Channel for the Formation of Kinematically Decoupled Cores in Early-type Galaxies. *The Astrophysical Journal*, 802:L3.

Tully, R. B. and Fisher, J. R. (1977). A new method of determining distances to galaxies. *A&A*, 54:661–673.

van de Sande, J., Kriek, M., Franx, M., van Dokkum, P. G., Bezanson, R., Bouwens, R. J., Quadri, R. F., Rix, H.-W., and Skelton, R. E. (2013). Stellar Kinematics of z ~ 2 Galaxies and the Inside-out Growth of Quiescent Galaxies. *The Astrophysical Journal*, 771:85.

van den Bosch, R. C. E. and van de Ven, G. (2009). Recovering the intrinsic shape of early-type galaxies. *Monthly Notices of the Royal Astronomical Society*, 398:1117–1128.

van der Marel, R. P. and Franx, M. (1993). A new method for the identification of non-Gaussian line profiles in elliptical galaxies. *The Astrophysical Journal*, 407:525–539.

Weinzirl, T., Jogee, S., Khochfar, S., Burkert, A., and Kormendy, J. (2009). Bulge n and B/T in High-Mass Galaxies: Constraints on the Origin of Bulges in Hierarchical Models. *The Astrophysical Journal*, 696:411–447.

Whitaker, K. (2011). Quiescent galaxies through cosmic time from (ultra-) low resolution NIR spectroscopy. In *Galaxy Formation*, page 41P.

Young, L. M., Scott, N., Serra, P., Alatalo, K., Bayet, E., Blitz, L., Bois, M., Bournaud, F., Bureau, M., Crocker, A. F., Cappellari, M., Davies, R. L., Davis, T. A., de Zeeuw, P. T., Duc, P.-A., Emsellem, E., Khochfar, S., Krajnović, D., Kuntschner, H., McDermid, R. M., Morganti, R., Naab, T., Oosterloo, T., Sarzi, M., and Weijmans, A.-M. (2014). The ATLAS^{3D} project - XXVII. Cold gas and the colours and ages of early-type galaxies. *Monthly Notices of the Royal Astronomical Society*, 444:3408–3426.

Erklärung

Hiermit erkläre ich, die vorliegende Arbeit selbständig verfasst zu haben und keine anderen als die in der Arbeit angegebenen Quellen und Hilfsmittel benutzt zu haben.

München,